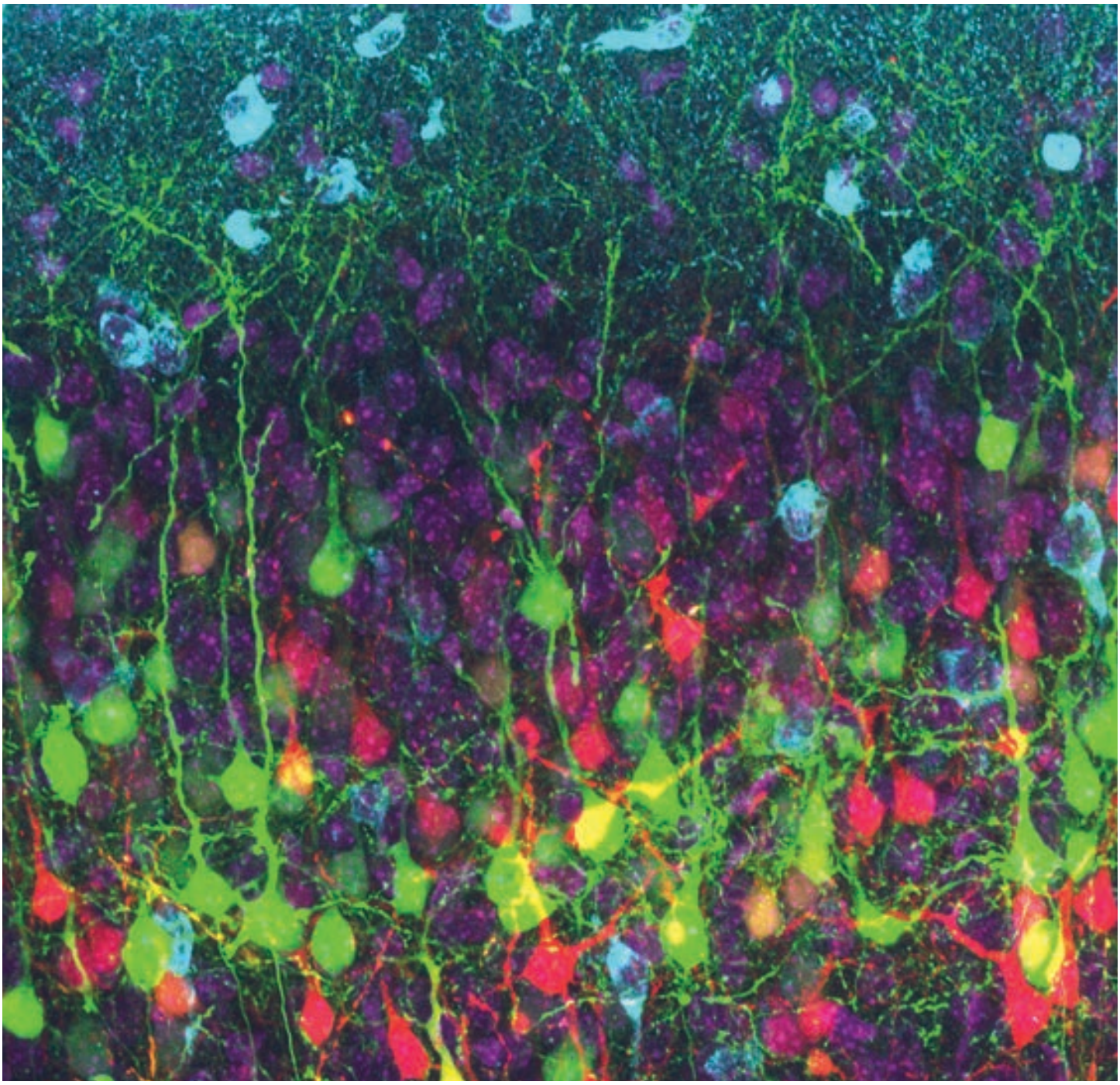

NEUROSCIENCE 2014

SHORT COURSE II

Advances in Brain-Scale, Automated Anatomical Techniques: Neuronal Reconstruction, Tract Tracing, and Atlasing

Organized by Sebastian Seung, PhD

SfN Society for Neuroscience

Short Course II

Advances in Brain-Scale, Automated Anatomical Techniques: Neuronal Reconstruction, Tract Tracing, and Atlasing

Sebastian Seung, PhD

Society for Neuroscience

Please cite articles using the model:
[AUTHOR'S LAST NAME, AUTHOR'S FIRST & MIDDLE INITIALS] (2014)
[CHAPTER TITLE] In: Advances in Brain-Scale, Automated Anatomical Techniques:
Neuronal Reconstruction, Tract Tracing, and Atlasing (Seung S, ed)
pp. [xx-xx]. Washington, DC: Society for Neuroscience.

SHORT COURSE II

Advances in Brain-Scale, Automated Anatomical Techniques: Neuronal Reconstruction, Tract Tracing, and Atlasing

Organized by Sebastian Seung, PhD

Friday, November 14

8:30 a.m.–6:00 p.m.

Location: Walter E. Washington Convention Center | Ballroom B | Washington, DC

TIME	AGENDA TOPICS	SPEAKER
8:00–8:30 a.m.	CHECK-IN	
8:30–8:40 a.m.	Opening Remarks	Sebastian Seung, PhD *Princeton Neuroscience Institute, Princeton University*
8:40–9:30 a.m.	Mapping the Brain with Serial Section Tomography	Tim Ragan, PhD *CEO, TissueVision, Inc.*
9:30–10:20 a.m.	CLARITY and Beyond: Tools for Integrated Brain Mapping	Kwanghun Chung, PhD *Massachusetts Institute of Technology*
10:20–10:50 a.m.	MORNING BREAK	
10:50–11:40 a.m.	Rapid High-Resolution Mapping of Intact Brains with CLARITY—Optimized Light-Sheet Microscopy (COLM)	Raju Tomer, PhD *Howard Hughes Medical Institute, Stanford University*
11:40 a.m.–12:30 p.m.	Mapping Local and Global Connectivity onto Functionally-Characterized Cortical Cells and Circuits	Troy Margrie, PhD *The MRC National Institute for Medical Research*
12:30–1:30 p.m.	LUNCH: Room 145 AB	
1:30–2:20 p.m.	Computational Techniques for Constructing Brain Atlases	Lydia Ng, PhD *Allen Institute for Brain Science*
2:20–3:20 p.m.	Panel Discussions	Drs. Osten, Chung, Tomer, Margrie, and Ng
3:20–3:30 p.m.	TUTORIAL INTRODUCTIONS	
3:30–3:45 p.m.	AFTERNOON BREAK	

AFTERNOON BREAKOUT SESSIONS * Participants select one discussion group at 3:45 p.m. and one at 5:00 p.m.

TIME	THEME		ROOM
3:45–4:45 p.m.	Group 1	Isotropic Fractionator Suzana Herculano-Houzel, PhD | *Institute of Biomedical Sciences, Federal University of Rio de Janeiro*	144A
	Group 2	FilamentTracer Marcel Oberlaender, PhD | *Max Planck Institute for Biological Cybernetics*	144B
	Group 3	Fiji/ImageJ Ignacio Arganda-Carreras, PhD | *The French National Institute for Agricultural Research (INRA)*	144C
4:45–5:00 p.m.	AFTERNOON BREAK		
5:00–6:00 p.m.	BREAKOUT SESSIONS REPEAT		

Table of Contents

Introduction

It is becoming feasible to rapidly generate high-resolution brainwide images using light microscopy, and computational methods are being developed to extract knowledge from these data. The field of cytoarchitectonics is being modernized by the ability to acquire and analyze the locations of all cell bodies. It is also becoming feasible to reconstruct entire axonal and dendritic arbors; in turn, information about molecular identity can be overlaid on such reconstructions. Methods of transsynaptic tracing are becoming useful and practical for tackling important scientific questions. Computational techniques of brain atlasing are enabling the alignment of all data within a common coordinate system.

All these advances are driving a renaissance of anatomy at the light-microscopic level. This short course will survey emerging automated anatomical methods and their scientific applications as well as providing "how-to" tutorials.

Mapping Brain Circuitry with a Light Microscope

Pavel Osten MD, PhD,[1] and Troy W. Margrie, PhD[2,3]

[1]Cold Spring Harbor Laboratory
Cold Spring Harbor, New York

[2]Department of Neuroscience, Physiology and Pharmacology
University College London
London, United Kingdom

[3]Division of Neurophysiology
The MRC National Institute for Medical Research
Mill Hill, London, United Kingdom

Introduction

The beginning of the 21st century has seen a renaissance in light microscopy and anatomical tract tracing that is rapidly advancing our understanding of the form and function of neuronal circuits. The introduction of instruments for automated imaging of whole mouse brains, new cell-type-specific and transsynaptic tracers, and computational methods for handling the whole-brain datasets has opened the door to neuroanatomical studies at an unprecedented scale. In this chapter, we present an overview of the state of play and future opportunities in charting long-range and local connectivity in the entire mouse brain and in linking brain circuits to function.

Since the pioneering work of Camillo Golgi in the latter 19th century and Santiago Ramón Y Cajal at the turn of the last century (Golgi, 1873; Ramón Y Cajal, 1904), advances in light microscopy (LM) and neurotracing methods have been central to the progress in our understanding of anatomical organization in the mammalian brain. The discovery of the Golgi silver-impregnation method allowed the visualization of neuron morphology, providing the first evidence for cell-type-based and connectivity-based organization in the brain. The introduction of efficient neuroanatomical tracers in the second half of the 20th century greatly increased the throughput and versatility of neuronal projection mapping, which led to the identification of many anatomical pathways and circuits, and revealed the basic principles of hierarchical and laminar connectivity in sensory, motor, and other brain systems (Rockland and Pandya, 1979; Felleman and Van Essen, 1991).

The beginning of this century has seen a new period of method-driven renaissance in neuroanatomy, one that is distinguished by the focus on large-scale projects generating unprecedented amounts of anatomical data. Instead of the traditional "cottage industry" approach of studying one anatomical pathway at a time, the new projects aim to generate complete datasets—so-called projectomes and connectomes—that can be used by the scientific community as resources for answering specific experimental questions. These efforts range in scale and resolution from the macroscopic—studies of the human brain by magnetic resonance imaging (MRI), to the microscopic—dense neural circuit reconstructions of small volumes of brain tissue by electron microscopy (EM) (Craddock et al., 2013; Helmstaedter, 2013).

Advancements in LM methods, the focus of our review, are being applied to the mapping of point-to-point connectivity between all anatomical regions in the mouse brain by means of sparse reconstructions of anterograde and retrograde tracers (Bohland et al., 2009). Taking advantage of the automation of LM instruments, powerful data processing pipelines, and combinations of traditional and modern viral-vector-based tracers, teams of scientists at Cold Spring Harbor Laboratory (CSHL), the Allen Institute for Brain Science (AIBS), and University of California, Los Angeles (UCLA), are racing to complete a connectivity map of the mouse brain—dubbed the "mesoscopic connectome"—which will provide the scientific community with online atlases for viewing entire anatomical datasets (Bohland et al., 2009). This chapter describes the rationale for mapping connectivity in the whole mouse brain at the mesoscale level by LM. These efforts demonstrate the transformative nature of today's LM-based neuroanatomy and the astonishing speed with which large amounts of data can be disseminated online and have an immediate impact on research in neuroscience laboratories around the world.

As the mouse mesoscopic connectomes are being completed, it is clear that LM methods will continue to impact the evolution of biological research and specifically neuroscience: New transsynaptic viral tracers are being engineered to circumvent the need to resolve synapses, which has constrained the interpretation of cell-to-cell connectivity in LM studies. Also, new assays combining anatomical and functional measurements are being applied to bridge the traditional structure–function divide in the study of the mammalian brain. This chapter aims to provide an overview of today's state of the art in LM instrumentation and to highlight the opportunities for progress, as well as the challenges that need to be overcome, in order to transform neuronal tracing studies into a truly quantitative science yielding comprehensive descriptions of long-range and local projections and connectivity at the level of whole mouse brains. We also discuss current strategies for the integration of anatomy and function in the study of mouse brain circuits.

Automated Light Microscopes for Whole-Brain Imaging

The field of neuroanatomy has traditionally been associated with labor-intensive procedures that greatly limited the throughput of data collection. Recent efforts to automate LM instrumentation have standardized and dramatically increased the throughput of anatomical studies. The main challenge for these methods is to maintain the rigorous quality of traditional neuroanatomical studies, resulting

NOTES

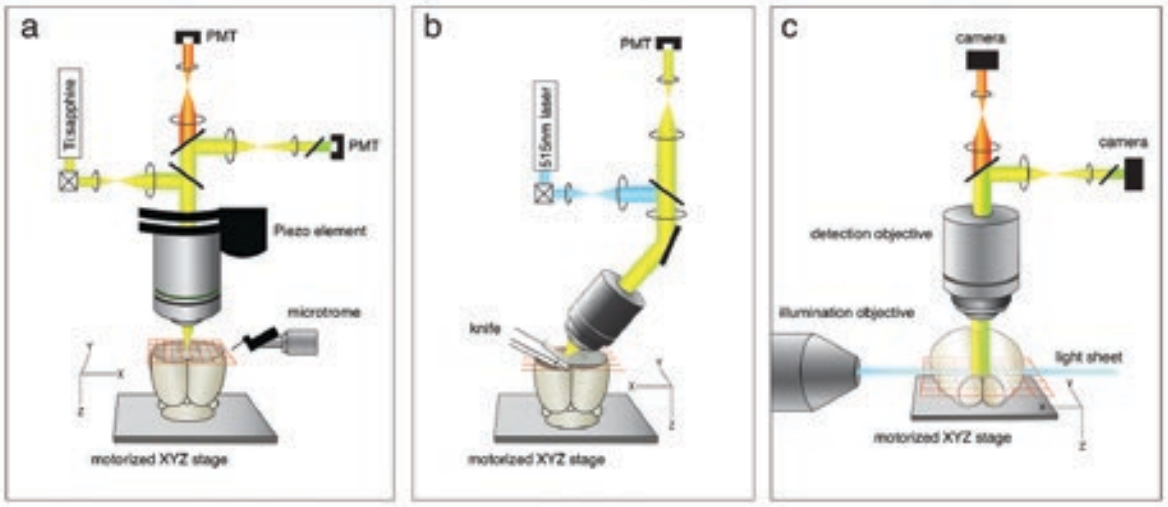

Figure 1. Whole-brain LM methods. ***a,*** STP tomography. Two-photon microscope is used to image the mouse brain in a coronal plane in a mosaic grid pattern and microtome sections off the imaged tissue. Piezo objective scanner can be used for *z*-stack imaging. Image adapted from Ragan et al. (2012), their Fig. 1*a*. ***b***, fMOST. Confocal line-scan is used to image the brain as a 1 µm thin section cut by diamond knife. Image adapted from Gong et al. (2013), their Fig. 1*a*. ***c***, LSFM. The cleared brain is illuminated from the side with the light sheet (blue) through an illumination objective (or cylinder lens [Dodt et al., 2007]) and imaged in a mosaic grid pattern from top. Image adapted from Niedworok et al. (2012), their Fig. 4*g*. In all instruments, the brain is moved under the objective on a motorized *XYZ* stage. PMT, photomultiplier tube.

from detailed visual analysis, careful data collection, and expert data interpretation.

There are currently two alternative approaches to automation of LM for imaging three-dimensional (3D) whole-brain datasets: one based on the integration of block-face microscopy and tissue sectioning, and the other based on light-sheet fluorescence microscopy (LSFM) of chemically cleared tissue. The first approach has been developed for wide-field imaging, line-scan imaging, and confocal and two-photon microscopy (Odgaard et al., 1990; Ewald et al., 2002; Tsai et al., 2003; Sands et al., 2005; Ragan et al., 2007; Mayerich et al., 2008; Li et al., 2011; Ragan et al., 2012; Gong et al., 2013). Common to all these instruments is the motorized movement of the sample under the microscope objective for top-view mosaic imaging, followed by mechanical removal of the imaged tissue before the next cycle of interleaved imaging and sectioning steps (Figs. 1*a*, *b*). Because the objective is always near the tissue surface, it is possible to use high numerical aperture (NA) lenses to achieve submicron resolution close to the diffraction limits of LM.[1]

Three instruments have been designed that combine two-photon microscopy (Denk et al., 1990) followed by tissue sectioning by either ultra-short laser pulses in all-optical histology (Tsai et al., 2003), milling machine in two-photon tissue cytometry (Ragan et al., 2007), or vibrating blade microtome in serial two-photon (STP) tomography (Ragan et al., 2012) (Fig. 1*a*). Whereas in both all-optical histology and two-photon tissue cytometry the sectioning obliterates the imaged tissue, the integration of vibratome-based sectioning in STP tomography allows the collection of the cut tissue for further analysis by, for example, immunohistochemistry (see Current Challenges and Opportunities for Whole-Brain LM Methods, below). In addition, the tissue preparation by simple formaldehyde fixation and agar embedding in STP tomography has minimal detrimental effects on fluorescence and brain morphology. This makes STP tomography applicable to a broad range of neuroanatomical projects utilizing genetically encoded fluorescent protein–based tracers, which are sensitive to fixation, dehydration, and tissue clearing conditions. This method is also versatile in terms of the mode and resolution of data collection. For example, imaging the mouse brain as a dataset of 280 serial coronal sections, evenly spaced at 50 µm and at *xy* resolution 1 µm, takes ~21 h and generates a brain atlas–like dataset

[1]Tsai et al. pioneered the approach of serial imaging by two-photon microscopy and tissue sectioning for *ex vivo* collection of neuronanatomical data. Ragan et al. (2012) introduced the method of STP tomography and demonstrated its use for anterograde and retrograde tracing in the mouse brain. Gong et al. (2013) demonstrated the first long-range tracing of individual axons in the mouse brain by the fluorescence-MOST (fMOST) method.

of ~70 gigabytes (GB). A complete visualization can be achieved by switching to 3D scanning of *z*-volume stacks between the mechanical sectioning steps, which allows the entire mouse brain to be imaged, for instance, at 1 µm *xy* and 2.5 µm *z* resolution in ~8 d, generating ~1.5 terabytes (TB) of data (Ragan et al., 2012). The instrument is commercially available from TissueVision (Cambridge, MA). The AIBS is using this methodology for its Mouse Connectivity project (see Mesoscopic Connectivity-Mapping Projects, below).

Two instruments have been designed to combine bright-field line-scan imaging and ultra-microtome sectioning of resin-embedded tissue into methods named knife-edge scanning microscopy (KESM) (Mayerich et al., 2008) and micro-optical sectioning tomography (MOST) (Li et al., 2011) (Fig. 1*b*). The latter was used to image Golgi-stained mouse brain at 0.33 × 0.33 × 1.0 µm *x-y-z* resolution, generating >8 TB of data in ~10 d (Mayerich et al., 2008; Li et al., 2011). The MOST instrument design was also recently built for fluorescent imaging (fMOST) by confocal laser scanning microscopy, with the throughput of one mouse brain at 1.0 µm voxel resolution in ~19 d (Gong et al., 2013). KESM imaging is now also available as a commercial service from 3Scan (San Francisco, CA).

The second, alternative, approach for automated whole-brain imaging is based on LSFM, also known as selective-plane illumination microscopy or SPIM (Huisken et al., 2004) and ultramicroscopy (Dodt et al., 2007) (Fig. 1*c*). Dodt et al. (2007) was the first to demonstrate the use of LSFM for imaging the entire mouse brain. This approach allows fast imaging of chemically cleared "transparent" mouse brains without the need for mechanical sectioning (Dodt et al., 2007; Niedworok et al., 2012), but at least until now, with some trade-offs for anatomical tracing applications. The chemical clearing procedures reduce the signal of fluorescent proteins, but this problem appears to be solved by a new hydrogel-based tissue transformation and clearing method called CLARITY (Chung et al., 2013; Chung and Deisseroth, 2013) (See the Short Course chapters "Advanced CLARITY Methods for Rapid and High-Resolution Imaging of Intact Tissues" by R. Tomer and K. Deisseroth and "CLARITY and Beyond: Tools for Integrated Brain Mapping" by K. Chung.) The spatial resolution of LSFM for the mouse brain has also been limited by the requirement for large field-of-view objectives with low power and low NA that were used for the visualization of the whole brain (Dodt et al., 2007; Leischner et al., 2009). However, new objectives with long working distance (WD) and high NA, such as 8 mm WD/0.9 NA objective from Olympus, promise to enable LSFM of the whole mouse brain at submicron resolution. If necessary, LSFM can also be combined with one of several forms of structured illumination (SI) to reduce out-of-focus background fluorescence and improve contrast (Kalchmair et al., 2010; Keller et al., 2010; Mertz and Kim, 2010). Taken together, these modifications are likely to enhance the applicability of LSFM to anterograde tracing of thin axons at high resolution in the whole mouse brain, as done by STP tomography in the AIBS Mouse Connectivity project (see Mesoscopic Connectivity-Mapping Projects, below) and by fMOST in a recent report (Gong et al., 2013).

In addition, LSFM is well suited for retrograde tracing in the mouse brain, which relies on detection of retrogradely fluorescently labeled neuronal somas that are typically >10 µm in diameter. Such application was recently demonstrated for mapping retrograde connectivity of granule cells of the mouse olfactory bulb (Niedworok et al., 2012) using rabies viruses that achieve high levels of fluorescent protein labeling (Wickersham et al., 2007a, b). (Wickersham et al., 2007a, described a genetically modified rabies virus designed to specifically label direct presynaptic input onto a given cell population.)

Mesoscopic Connectivity-Mapping Projects

The labeling of neurons and subsequent neuroanatomical tract tracing by LM methods has been used for more than a century to interrogate the anatomical substrate of information transmission in the brain. Throughout those years, the credo of neuroanatomy, "The gain in brain is mainly in the stain," meant to signify that progress was made mainly through the development of new anatomical tracers. Yet despite the decades of neuroanatomical research, the laborious nature of tissue processing and data visualization kept the progress in our knowledge of brain circuitry at a disappointingly slow pace (Bohland et al., 2009). Today, neuroanatomy stands to greatly benefit from the application of high-throughput automated LM instruments and powerful informatics tools for the analysis of mouse brain data (Ng et al., 2009; Jones et al., 2011). The high-resolution capacity these LM methods afford, and the fact that an entire brain dataset can be captured, makes these systems well suited for systematic

NOTES

charting of the spatial profile and connectivity of populations of neurons and even individual cells projecting over long distances.

The pioneering effort in the field of anatomical projects applied at the scale of whole animal brains was the Allen Mouse Brain Atlas of Gene Expression, which catalogued *in situ* hybridization maps of more than 20,000 genes in an online 3D digital mouse brain atlas (Lein et al., 2007; Dong, 2008; Ng et al., 2009). (Lein et al., 2007, pioneered large-scale LM-based whole-brain anatomy and introduced the Allen Mouse Brain Atlas and online data portal.)

The proposal by a consortium of scientists led by Partha Mitra (CSHL) to generate similar LM-based atlases of "brainwide neuroanatomical connectivity" in several animal models (Bohland et al., 2009) has in short time spurred three independent projects, each promising to trace all efferent and afferent anatomical pathways in the mouse brain. The Mitra team's Mouse Brain Architecture Project (http://brainarchitecture.org) at CSHL aims to image >1000 brains; the Allen Mouse Brain Connectivity Atlas project (http://connectivity.brain-map.org), led by Hongkui Zeng at AIBS, plans for >2000 brains; and the Mouse Connectome Project (www.mouseconnectome.org), led by Hong-Wei Dong at UCLA, plans for 500 brains, each brain injected with 4 tracers. While the CSHL and UCLA projects use automated wide-field fluorescence microscopy (Hamamatsu Nanozoomer 2.0 [Hamamatsu Photonics, Hamamatsu City, Japan] and Olympus VS110) to image manually sectioned brains, the Mouse Connectivity project at the AIBS is being done entirely by STP tomography (Ragan et al., 2012).

The main complementary strength of these efforts, however, comes from the broad range of tracers used. Given that each tracer has its own advantages and problems (Lanciego and Wouterlood, 2011), the information derived from all three projects will ensure generalizable interpretation of the projection results throughout the brain. The CSHL group uses a combination of traditional anterograde and retrograde tracers, fluorophore-conjugated dextran amine (BDA) (Glover et al., 1986), and cholera toxin B (CTB) subunit (Llewellyn-Smith et al., 2000), respectively, which are complemented by a combination of viral-vector-based tracers, green fluorescent protein (GFP)–expressing adeno-associated virus (AAV) (Grinevich et al., 2005) for anterograde tracing (Fig. 2*a*), and modified rabies virus (Wickersham et al., 2007a) for retrograde tracing. Although the virus-based methods are less tested, they offer advantages in terms of the brightness of labeling and the possibility of cell-type-specific targeting using Cre-dependent viral vectors (Atasoy et al., 2008) and transgenic lines expressing the Cre recombinase enzyme under the control of cell-type-specific promoters (Madisen et al., 2010, 2012; Taniguchi et al., 2011). The AIBS team uses solely anterograde tracing by AAV-GFP viruses (Harris et al., 2012) (Fig. 2*b*), in many cases taking advantage of Cre driver mouse lines for cell-type-specific labeling. Finally, the team at UCLA is using a strategy of two injections per brain, each with a mix of anterograde and retrograde tracers (Thompson and Swanson, 2010), CTB together with *Phaseolus vulgaris* leucoagglutinin (PHA-L) (Gerfen and Sawchenko, 1984), and FluoroGold (FG) (Naumann et al., 2000) together with BDA (Reiner et al., 2000; Thompson and Swanson, 2010). This approach has an added advantage because it allows direct visualization of the convergence of inputs and outputs from across different areas in one brain (Conte et al., 2009; Thompson and Swanson, 2010; Hintiryan et al., 2012).

The unprecedented amounts of data being collected by these projects means that the significant person-hours historically spent performing microscopy have largely shifted toward data analysis. The first step of such data analysis comprises the compilation of the serial section images for viewing as whole-brain datasets at resolutions beyond the minimum geometric volume of the neuronal structures of interest: somas for retrograde and axons for anterograde tracing. All three projects offer a convenient way to browse the datasets online, including high-resolution zoom-in views that in most cases are sufficient for visual determination of labeled somas and axons. Importantly, all three projects use the Allen Mouse Brain Atlas for the registration of the coronal sections, which will provide significant help in the cross-validation of results obtained from the different tracers. The Allen Mouse Brain Connectivity Atlas website (http://connectivity.brain-map.org/static/brainexplorer) also offers the option to view the data after projection segmentation, which selectively highlights labeled axons, as well as in 3D in the Brain Explorer registered to the Allen Mouse Brain Atlas (Sunkin et al., 2013) (Fig. 2*b*).

The second step of data analysis requires the development of informatics methods for quantitation of the datasets, which will facilitate the interpretation of the online available data. The Allen Mouse Brain Connectivity Atlas online tools allow the user to search the projections between injected regions and display the labeled pathways as tracks in 3D in the Brain Explorer. The CSHL and UCLA connectomes can

currently be viewed online as serial section datasets. The data from the Cre driver mouse lines in the AIBS project provide a unique feature of cell-type specificity for the interpretation of the anterograde projections. The main strength of the CSHL and UCLA efforts lies in the multiplicity of the anatomical tracers utilized. The use of multiple retrograde tracers in particular will yield useful information, since retrogradely labeled somas (>10 μm in diameter) are easier to quantitate than thin (<1 μm) axon fibers. These experiments will also provide an important comparison between the traditional CTB and FluoroGold tracers and the rabies-virus tracer that is also being used in transsynaptic labeling (see below), but is less studied and may show some variation in transport affinity at different types of synapses.

In summary, the LM-based mesoscopic mapping projects are set to transform the study of the circuit wiring of the mouse brain by providing online access to whole-brain datasets from several thousand injections of anterograde and retrograde tracers. The informatics tools being developed to search the databases will greatly aid in parsing the large amounts of data and in accessing specific brain samples for detailed scholarly analyses by the neuroscience community.

Mapping Connectivity Using Transsynaptic Tracers

In contrast to EM methods, which provide a readout of neuronal connectivity with synapse resolution over small volumes of tissue, the whole-brain LM methods permit the assessment of projection-based connectivity between brain regions and, in some cases, between specific cell types in those regions, but without the option to visualize the underlying synaptic contacts. Transsynaptic viruses that cross either multiple or single synapses can help circumvent the requirement to confirm connectivity at the EM resolution, since such connectivity may be inferred from the known direction and mechanism of spread of the transsynaptic tracer. Transsynaptic tracers based on rabies (RV), pseudorabies (PRV), and herpes simplex (HSV) viruses, which repeatedly cross

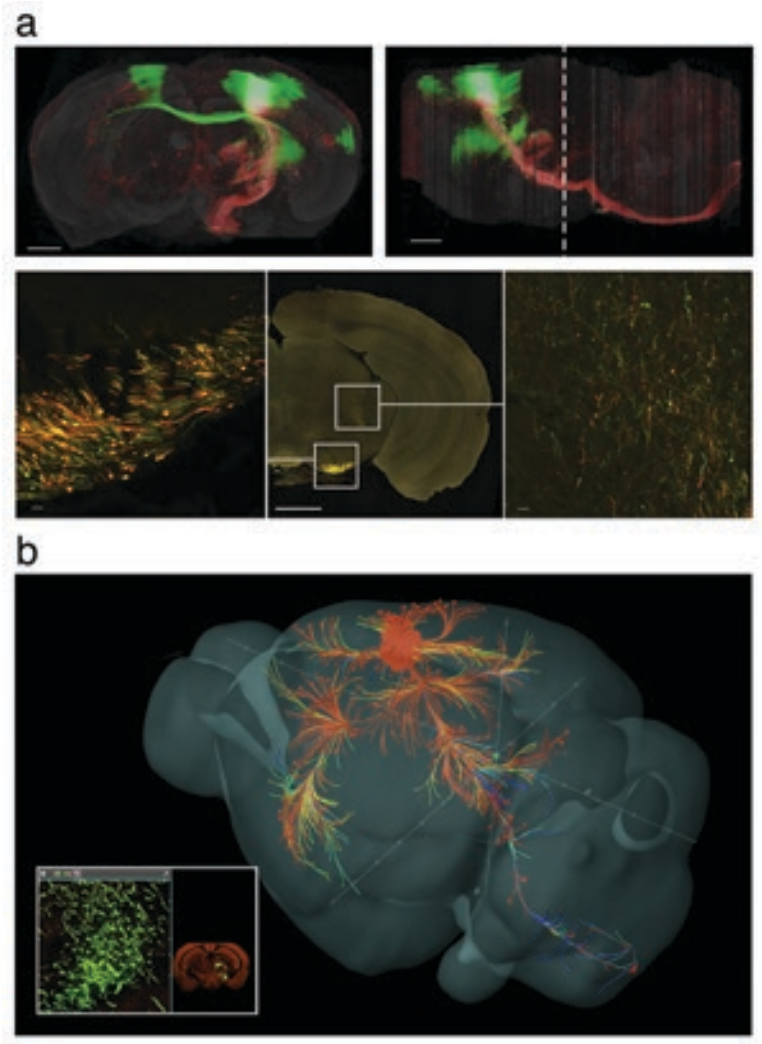

Figure 2. Primary motor cortex (MOp) projection maps. ***a,*** Mouse Brain Architecture (http://brainarchitecture.org) data of AAV-GFP injected into the supragranular layers and AAV–red fluorescent protein (RFP) injected in the infragranular layers (F. Mechler and P. Mitra, CSHL, unpublished observations). Top panels, Frontal (left) and lateral (right) views of the volume-rendered brain. Scale bars, 1000 μm. Bottom panels, High-zoom views of the regions highlighted in the central image. Left, Axonal fibers in the cerebral peduncle; Right, Projections to the midbrain reticular nucleus. Scale bars, 20 μm. ***b,*** Mouse Connectivity (http://connectivity.brain-map.org) data of a similar AAV-GFP injection show the MOp projectome reconstructed in the Allen Brain Explorer (Sunkin et al., 2013; H. Zeng, AIBS, unpublished observations). Lower left inset, High-zoom view and coronal section overview of projections in the ventral posteromedial nucleus of the thalamus (VPM).

NOTES

synaptic connections in a retrograde or anterograde direction, are powerful tools for elucidating multistep pathways both up and downstream from the starter cell population (Song et al., 2005; Ekstrand et al., 2008; Ugolini, 2010). Furthermore, modified transsynaptic RVs have been developed that are restricted in their spread to a single synaptic jump and thus can be used to identify monosynaptic connections onto and downstream of specific neuronal populations and even individual cells (Wickersham et al., 2007a; Callaway, 2008; Marshel et al., 2010; Arenkiel et al., 2011; Miyamichi et al., 2011; Rancz et al., 2011; Wickersham and Feinberg, 2012; Takatoh et al., 2013).

RV spreads from the initially infected cells in a transsynaptic retrograde manner (Finke and Conzelmann, 2005; Ugolini, 2010). RV infection does not occur via spurious spread or uptake by fibers of passage and, since it cannot cross via electrical synapses, it is an effective tool for unidirectional anatomical tracing (Ugolini, 1995). In the modified RV system, the infection can also be cell-type-targeted by encapsulating the glycoprotein-deficient RV with an avian virus envelope protein (SAD-ΔG-EnvA). This restricts infection to only those cells that express an avian tumor virus receptor A gene (TVA), which is natively found in birds but not in mammals (Young et al., 1993; Federspiel et al., 1994). Thus, the delivery of vectors driving the expression of both TVA and RV-glycoprotein (RV-G) into a single cell (Wickersham et al., 2007b; Marshel et al., 2010; Rancz et al., 2011) (see Integrating Brain Anatomy and Function, below) or a specific population of cells (Wall et al., 2010; Miyamichi et al., 2011) ensures that only the targeted cell or cells will (1) be susceptible to initial infection and (2) provide the replication-incompetent virus with RV-G required for transsynaptic infection (Etessami et al., 2000). In this system, the virus can spread from the primarily infected cell(s) to the presynaptic input cells, which become labeled by the fluorescent protein expression. However, because the presynaptic cells do not express RV-G (Wickersham et al., 2007b), the virus cannot spread further. This approach thus allows the discovery of the identity and location of the upstream input network relative to a defined population of neurons (Arenkiel et al., 2011; Takatoh et al., 2013).[2]

Brain-region and cell-type specificity for mapping connectivity by the modified RV system can be achieved by using a Cre recombinase–dependent helper virus driving expression of TVA and RV-G and transgenic mouse lines that express Cre in specific cell types or cortical layers (Madisen et al., 2010; Wall et al., 2010; Taniguchi et al., 2011). This strategy is particularly useful for brain regions comprising many different cell types that could not otherwise be selectively targeted. Moreover, the engineering of other neurotropic transsynaptic viruses is adding new tools for anatomical tracing, including Cre-dependent anterograde tracers based on a modified H129 strain of HSV (Lo and Anderson, 2011) and vesicular stomatitis virus (Beier et al., 2011), and retrograde tracers based on a modified PRV (H. Oyibo and A. Zador, CSHL, personal communication). The use of retrograde and anterograde transsynaptic viruses, in combination with whole-brain LM methods, thus promises to afford unprecedented access to the upstream and downstream connectivity of specific cell types in the mouse brain.

Current Challenges and Opportunities for Whole-Brain LM Methods

As highlighted above, LM instruments for whole-brain imaging are expected to make a significant contribution in large-scale projects that focus on anatomical connectivity at the level of the whole mouse brain. It has also become clear that the use of these instruments will have an impact in many experimental applications in different neuroscience laboratories. It is therefore imperative that there exist broadly applicable image processing, warping, and analytical tools that will facilitate data sharing and across-laboratory collaboration and validation in future neuroscience studies focusing on, for example, mapping whole-brain anatomical changes during development and in response to experience.

One practical problem arising from the choice to scan entire mouse brains at high resolution relates to the handling of large datasets (up to several TB per brain), which necessitates automated analytical pipelining. STP tomography is currently the most broadly used method among the whole-brain LM instruments, and there are freely available informatics tools for compiling STP tomography image stacks and viewing them as 3D data, including algorithms that automate seamless stitching (Ragan et al., 2012). Another key challenge for charting the distribution of the labeled elements in the whole mouse brain is the process of accurate registration

[2] Rancz et al. (2011) were the first to combine intracellular neuronal recording with DNA delivery. The authors used this method to map the synaptic function of a single cell *in vivo* and then target RV-based retrograde labeling of the cells' synaptic input. Marshel et al. (2010) described an electroporation method for single-cell delivery of DNA for targeted infection of modified RV.

of the individual brain datasets onto an anatomical reference atlas. To this end, scientists at AIBS have generated the open-source, segmented Allen Mouse Brain Atlas for the adult C57BL/6 mouse (Lein et al., 2007; Dong, 2008; Ng et al., 2009; Sunkin et al., 2013), which is also available for registration of datasets generated by STP tomography (Figs. 2*b*, 4). In addition, the so-called Waxholm space (WHS) for standardized digital atlasing (Hawrylycz et al., 2011) allows comparisons of registered mouse brain data using multiple brain atlases, including the Allen Mouse Brain Atlas, the digital Paxinos and Franklin Mouse Brain Atlas (Paxinos and Franklin, 2004), and several MRI reference mouse brains. The continuing development of the WHS and other online data analysis platforms (Moene et al., 2007; Swanson and Bota, 2010; Jones et al., 2011) will be essential for making standardized comparisons of mouse brain data collected by different laboratories using different instruments.

The completion of the three mesoscopic connectome projects in the next several years will yield a comprehensive map of point-to-point connectivity between anatomical regions in the mouse brain (Bohland et al., 2009). Determining the cell-type identity of the neurons sending and receiving the connections in the brain regions will be essential for interpreting the function of the brainwide neural circuits. Immunohistochemical analyses of labeled circuits have proven invaluable for ascertaining the identity of specific classes of neurons (Klausberger and Somogyi, 2008; O'Rourke et al., 2012; Defelipe et al., 2013) and synaptic connections (Callaway, 2008; Emes and Grant, 2012). The combination of immunohistochemical analysis by array tomography (Micheva and Smith, 2007; Micheva et al., 2010) and anatomical tracing by the whole-brain LM instruments promises to be particularly powerful, since it will bring together two largely automated methodologies with complementary focus on synaptic and mesoscopic connectivity, respectively. STP tomography outputs sectioned tissue (typically, 50-µm-thick sections [Ragan et al., 2012]), which can be further resectioned, processed and reimaged by array tomography for integrating cell-type-specific information into the whole-brain datasets. Industrial-level automation of slice capture and immunostaining can be developed to minimize manual handling and enhance the integration of immunohistochemistry and STP tomography. In addition, sectioning and immunostaining can be applied to LSFM-imaged mouse brains (Niedworok et al., 2012).

A related, cell-type-focused application of whole-brain LM imaging will be to quantitatively map the distribution (the cell counts) of different neuronal cell types in all anatomical regions in the mouse brain. Several such cell-count-based anatomical studies have been done previously at smaller scales, revealing, for example, cell densities with respect to cortical vasculature (Tsai et al., 2009) or the density of neuronal cell types per layers in a single cortical column (Meyer et al., 2010, 2011; Oberlaender et al., 2012). Using the whole-brain LM methods, a comprehensive anatomical atlas of different GABAergic inhibitory interneurons (Petilla Interneuron Nomenclature Group et al., 2008) can now be generated by imaging cell-type-specific Cre knock-in mouse lines (Madisen et al., 2010; Taniguchi et al., 2011) crossed with Cre-dependent reporter mice expressing nuclear GFP. These and similar datasets for other neuronal cell types will complement the mesoscopic brain region connectivity data and help the interpretation of the immunohistochemistry data by providing a reference for total numbers of specific cell types per anatomical brain region.

Integrating Brain Anatomy and Function

The anterograde, retrograde, and transsynaptic tracing approaches described above will yield the structural scaffold of anatomical projections and connections throughout the mouse brain. However, such data will not be sufficient to identify how specific brain regions connect to form functional circuits driving different behaviors. Bridging whole-brain structure and function is the next frontier in systems neuroscience, and the development of new technologies and methods will be crucial in achieving progress.

The structure–function relationship of single neurons can be examined by *in vivo* intracellular delivery of the DNA vectors required for targeting and driving transsynaptic virus expression via patch pipettes in loose cell-attached mode for electroporation (Marshel et al., 2010) or via whole-cell recording (Rancz et al., 2011) (Fig. 3). Used in combination with two-photon microscopy, this single-cell delivery technique may also be targeted at fluorescently labeled neurons of specific cell types (Margrie et al., 2003; Kitamura et al., 2008; Marshel et al., 2010). The whole-cell method is particularly informative, since its intracellular nature permits recording the intrinsic biophysical profile of the target cell, which, in turn, may reflect its functional connectivity status within the local network (Angelo et al., 2012). In addition, by recording sensory-evoked inputs, it is possible to compare single-cell

NOTES

synaptic receptive fields with anatomical local and long-range connectivity traced by LM methods (Rancz et al., 2011). This combinatorial approach, involving single-cell electrophysiology and genetic manipulation designed for connection mapping, makes it possible to test long-standing theories regarding the extent to which emergent features of sensory cortical function manifest via specific wiring motifs (Reid, 2012).

As has recently been achieved for serial EM–based reconstruction (Bock et al., 2011; Briggman et al., 2011), it will also be valuable to functionally characterize larger local neuronal populations for registration against LM-based connectivity data. In this sense, genetically encoded calcium indicators (GECIs), which permit physiological characterization of neuronal activity in specific cell types (Mank et al., 2008; Wallace et al., 2008; Akerboom et al., 2012), alongside viral vectors for transsynaptic labeling and LM-based tracing, will play critical complementary roles. Large-volume *in vivo* two-photon imaging of neuronal activity before *ex vivo* whole-brain imaging will establish the extent to which connectivity patterns relate to function (Ko et al., 2011) at the level of single cells and local and long-range circuits. Interpolation of such experiments will rely on the ability to cross-register *in vivo* functional imaging with complete *ex vivo* LM connectivity data. Preliminary experiments (already hinting at the spatial spread of monosynaptic connectivity of individual principal cortical cells) suggest that the combination of functional imaging with traditional anatomical circuit reconstruction may be feasible only at the local network level, where connection probability is the highest (Thomson et al., 2002; Holmgren et al., 2003; Song et al., 2005). Given the broad, sparse expanse of connectivity in most brain regions—and especially in cortical areas—high-throughput whole-brain LM methods will be imperative for complete anatomical circuit reconstruction of the functionally characterized local networks.

The amalgamation of whole-brain LM and physiological methods for single neurons and small networks offers a powerful means to study the mouse brain. A promising application of this approach will be to trace the synaptic circuits of neurons functionally characterized in head-fixed behaving animals engaged in tasks related to spatial navigation, sensorimotor integration, and other complex brain functions (Harvey et al., 2009, 2012; Huber et al., 2012). (Harvey et al., 2009, introduced the method of physiological recording in head-restrained mice on a spherical treadmill performing spatial tasks in virtual environment.) This research will lead to the generation of whole-brain structure–function

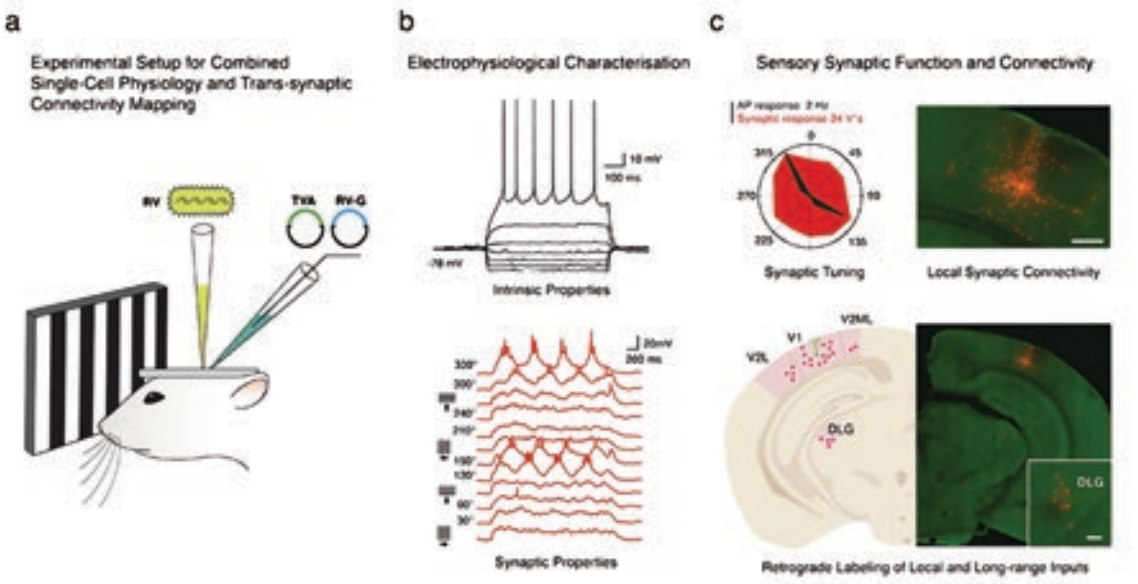

Figure 3. Mapping the function and connectivity of single cells in the mouse brain *in vivo*. ***a***, Patch pipettes (with internal solutions containing DNA vectors used to drive the expression of the TVA and RV-G proteins) are used to perform a whole-cell recording of the intrinsic and sensory-evoked synaptic properties of a single layer 5 neuron in primary visual cortex. ***b,*** Following the recording, the encapsulated modified RV is injected into the brain in proximity to the recorded neuron. ***c,*** After a period of ≤12 d that ensures retrograde spread of the modified RV from the recorded neuron, the brain is removed and imaged for identification of the local and long-range presynaptic inputs underlying the tuning of the recorded neuron to the direction of visual motion (polar plot). Top and bottom scale bars, 300 µm and 50 µm, respectively. Images modified from Rancz et al. (2011), their Fig. 4. AP, action potential; DLG, dorsal lateral geniculate.

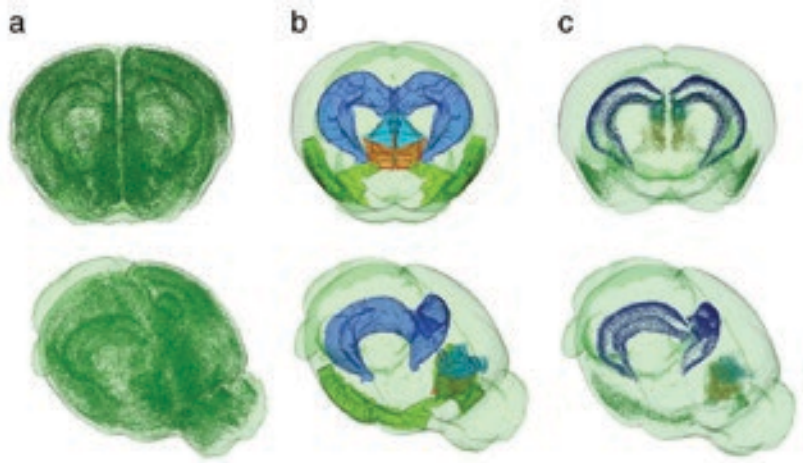

Figure 4. Imaging c-fos induction as a means to map whole-brain activation. ***a,*** 3D visualization of 367,378 c-fos-GFP cells detected in 280 coronal sections of an STP tomography dataset of a mouse brain after novelty exploration. ***b,*** Examples of anatomical segmentation of the brain volume with the Allen Mouse Brain Reference Atlas labels (Sunkin, et al., 2013) modified for the 280-section STP tomography datasets: hippocampus (blue), prelimbic (aqua blue), infralimbic (orange), and piriform (green) cortex. ***c,*** Visualization of c-fos-GFP cells in the hippocampus (38,170 cells), prelimbic (3305 cells), infralimbic (3827 cells), and piriform (10,910 cells) cortex (P. Osten, Y. Kim, and K. Umadevi Venkataraju, CSHL, unpublished observations).

hypotheses for specific behaviors, which can then be tested for causality by optogenetic methods targeted to the identified cell types and brain regions (Fenno et al., 2011). Furthermore, the LM, physiological, and optogenetic methods can be applied to interrogate entire brain systems in large-scale projects, as is currently being done for the mouse visual cortex in an effort led by Christof Koch and R. Clay Reid at AIBS (Koch and Reid, 2012).

Finally, the neuroscience community has begun to discuss the feasibility of mapping activity at cellular resolution in whole brains and linking the identified activity patterns to brain anatomy (Alivisatos et al., 2013). Today, such experiments are possible in small, transparent organisms, as was demonstrated by two-photon microscopy and LSFM-based imaging of brain activity in larval zebrafish expressing the calcium indicator GCaMP (Ahrens et al., 2012; Akerboom et al., 2012; Ahrens and Keller, 2013). Understandably, however, LM-based approaches will not be useful for *in vivo* whole-brain imaging in larger, nontransparent animals; thus, the invention of new, disruptive technologies will likely be needed to achieve the goal of real-time brain activity mapping at cellular resolution in, for example, the mouse. On the other hand, LM methods can be used to map patterns of whole-brain activation indirectly, by post hoc visualization of activity-induced expression of immediate early genes (IEGs), such as *c-fos*, *Arc*, or *Homer 1a* (Herrera and Robertson, 1996). Transgenic fluorescent IEG-reporter mice, like c-fos-GFP or Arc-GFP mice (Barth et al., 2004; Reijmers et al., 2007; Grinevich et al., 2009), can be trained in a specific behavior, their brains subsequently imaged *ex vivo*, and the exact distribution of GFP-positive neurons mapped and analyzed by computational methods (Fig. 4). In this approach, a statistical analysis of the counts of GFP-labeled neurons can be used to identify brain regions and cell types activated during behaviors, but without providing any information on the temporal sequence of brain region activation or the firing patterns of the activated cells. However, the development of more sensitive (e.g., fluorescent RNA-based) methods may allow calibration of the cellular signal with respect to the temporal window and the pattern of activity related to the IEG induction. Such calibration would significantly enhance the power of LM-based whole-brain IEG mapping, which, in combination with the connectomic data, could then be used to begin to build cellular resolution models of function-based whole-brain circuits.

Conclusion

The advances in automated LM methods, anatomical tracers, physiological methods, and informatics tools have begun to transform our understanding of the circuit wiring in the mouse brain. The focus on the mouse as an animal model is, of course, not accidental. In addition to the generation of cell-type-specific knock-in mouse lines (Madisen et al., 2010, 2012; Taniguchi et al., 2011) that allow the study of specific neuronal populations in the normal brain, mouse genetics are used in hundreds of laboratories to model gene mutations linked to heritable human disorders, including complex cognitive disorders such as autism and schizophrenia. Without doubt,

NOTES

understanding the relationships between brain structure and function in the genetic mouse models will be crucial to understanding the underlying brain circuit mechanisms of these disorders. The toolbox of LM methods described here, and the continuing development of new methods, promise to transform the study of brain circuits in animal models and to decipher the structure–function relationships essential to understanding complex brain functions and their deficits in human brain disorders.

Acknowledgments

We thank Partha Mitra, Hongkui Zeng, and Christian Niedworok for comments on the manuscript and J. Kuhl for the graphics. P.O. is supported by National Institute of Mental Health Grant 1R01MH096946-01 and Simons Foundation for Autism Research Grants 204719 and 253447. T.W.M. is a Wellcome Trust Investigator and is supported by the Medical Research Council MC U1175975156. This chapter was previously published in full as Osten P, Margrie TW (2013) Mapping brain circuitry with a light microscope, Nat Methods 10:515–523.

References

Ahrens MB, Keller PJ (2013) Whole-brain functional imaging at cellular resolution using light-sheet microscopy. Nat Methods 10:413–420.

Ahrens MB, Li JM, Orger MB, Robson DN, Schier AF, Engert F, Portugues R (2012) Brain-wide neuronal dynamics during motor adaptation in zebrafish. Nature 485:471–477.

Akerboom J, Chen TW, Wardill TJ, Tian L, Marvin JS, Mutlu S, Calderón NC, Esposti F, Borghuis BG, Sun XR, Gordus A, Orger MB, Portugues R, Engert F, Macklin JJ, Filosa A, Aggarwal A, Kerr RA, Takagi R, Kracun S, et al. (2012) Optimization of a GCaMP calcium indicator for neural activity imaging. J Neurosci 32:13819–13840.

Alivisatos AP, Chun M, Church GM, Deisseroth K, Donoghue JP, Greenspan RJ, McEuen PL, Roukes ML, Sejnowski TJ, Weiss PS, Yuste R (2013) Neuroscience. The brain activity map. Science 339:1284–1285.

Angelo K, Rancz EA, Pimentel D, Hundahl C, Hannibal J, Fleischmann A, Pichler B, Margrie TW (2012) A biophysical signature of network affiliation and sensory processing in mitral cells. Nature 488:375–378.

Arenkiel BR, Hasegawa H, Yi JJ, Larsen RS, Wallace ML, Philpot BD, Wang F, Ehlers MD (2011) Activity-induced remodeling of olfactory bulb microcircuits revealed by monosynaptic tracing. PLoS ONE 6:e29423.

Atasoy D, Aponte Y, Su HH, Sternson SM (2008) A FLEX switch targets channelrhodopsin-2 to multiple cell types for imaging and long-range circuit mapping. J Neurosci 28:7025–7030.

Barth AL, Gerkin RC, Dean KL (2004) Alteration of neuronal firing properties after *in vivo* experience in a FosGFP transgenic mouse. J Neurosci 24:6466–6475.

Beier KT, Saunders A, Oldenburg IA, Miyamichi K, Akhtar N, Luo L, Whelan SP, Sabatini B, Cepko CL (2011) Anterograde or retrograde transsynaptic labeling of CNS neurons with vesicular stomatitis virus vectors. Proc Natl Acad Sci USA 108:15414–15419.

Bock DD, Lee WC, Kerlin AM, Andermann ML, Hood G, Wetzel AW, Yurgenson S, Soucy ER, Kim HS, Reid RC (2011) Network anatomy and *in vivo* physiology of visual cortical neurons. Nature 471:177–182.

Bohland JW, Wu C, Barbas H, Bokil H, Bota M, Breiter HC, Cline HT, Doyle JC, Freed PJ, Greenspan RJ, Haber SN, Hawrylycz M, Herrera DG, Hilgetag CC, Huang ZJ, Jones A, Jones EG, Karten HJ, Kleinfeld D, Kötter R, et al. (2009) A proposal for a coordinated effort for the determination of brainwide neuroanatomical connectivity in model organisms at a mesoscopic scale. PLoS Comput Biol 5:e1000334.8

Briggman KL, Helmstaedter M, Denk W (2011) Wiring specificity in the direction-selectivity circuit of the retina. Nature 471:183–188.

Callaway EM (2008) Transneuronal circuit tracing with neurotropic viruses. Curr Opin Neurobiol 18:617–623.

Chung K, Deisseroth K (2013) CLARITY for mapping the nervous system. Nat Methods 10:508–513

Chung K, Wallace J, Kim SY, Kalyanasundaram S, Andalman AS, Davidson TJ, Mirzabekov JJ, Zalocusky KA, Mattis J, Denisin AK, Pak S, Bernstein H, Ramakrishnan C, Grosenick L, Gradinaru V, Deisseroth K (2013) Structural and molecular interrogation of intact biological systems. Nature 497:332–337.

Conte WL, Kamishina H, Reep RL (2009) Multiple neuroanatomical tract-tracing using fluorescent Alexa Fluor conjugates of cholera toxin subunit B in rats. Nat Protoc 4:1157–1166.

Craddock RC, Jbabdi S, Yan CG, Vogelstein JT, Castellanos FX, Di Martino A, Kelly C, Heberlein K, Colcombe S, Milham M (2013) Imaging human connectomes at the macroscale. Nat Methods 10:524–539.

Defelipe J, López-Cruz PL, Benavides-Piccione R, Bielza C, Larrañaga P, Anderson S, Burkhalter A, Cauli B, Fairén A, Feldmeyer D, Fishell G, Fitzpatrick D, Freund TF, González-Burgos G, Hestrin S, Hill S, Hof PR, Huang J, Jones EG, Kawaguchi Y, et al. (2013) New insights into the classification and nomenclature of cortical GABAergic interneurons. Nat Rev Neurosci 14:202–216.

Denk W, Strickler JH, Webb WW (1990) Two-photon laser scanning fluorescence microscopy. Science 248:73–76.

Dodt HU, Leischner U, Schierloh A, Jährling N, Mauch CP, Deininger K, Deussing JM, Eder M, Zieglgänsberger W, Becker K (2007) Ultramicroscopy: three-dimensional visualization of neuronal networks in the whole mouse brain. Nat Methods 4:331–336.

Dong HW (2008) The Allen reference atlas: a digital color brain atlas of the C57Bl/6J male mouse. Hoboken, NJ: Wiley.

Ekstrand MI, Enquist LW, Pomeranz LE (2008) The alpha-herpesviruses: molecular pathfinders in nervous system circuits. Trends Mol Med 14:134–140.

Emes RD, Grant SG (2012) Evolution of synapse complexity and diversity. Ann Rev Neurosci 35:111–131.

Etessami R, Conzelmann KK, Fadai-Ghotbi B, Natelson B, Tsiang H, Ceccaldi PE (2000) Spread and pathogenic characteristics of a G-deficient rabies virus recombinant: an *in vitro* and *in vivo* study. J Gen Virol 81:2147–2153.

Ewald AJ, McBride H, Reddington M, Fraser SE, Kerschmann R (2002) Surface imaging microscopy, an automated method for visualizing whole embryo samples in three dimensions at high resolution. Dev Dyn 225:369–375.

Federspiel MJ, Bates P, Young JA, Varmus HE, Hughes SH (1994) A system for tissue-specific gene targeting: transgenic mice susceptible to subgroup A avian leukosis virus–based retroviral vectors. Proc Natl Acad Sci USA 91:11241–11245.

Felleman DJ, Van Essen DC (1991) Distributed hierarchical processing in the primate cerebral cortex. Cereb Cortex 1:1–47.

Fenno L, Yizhar O, Deisseroth K (2011) The development and application of optogenetics. Ann Rev Neurosci 34:389–412.

Finke S, Conzelmann KK (2005) Replication strategies of rabies virus. Virus Res 111:120–131.

Gerfen CR, Sawchenko PE (1984) An anterograde neuroanatomical tracing method that shows the detailed morphology of neurons, their axons and terminals: immunohistochemical localization of an axonally transported plant lectin, *Phaseolus vulgaris* leucoagglutinin (PHA-L). Brain Res 290:219–238.

Glover JC, Petursdottir G, Jansen JK (1986) Fluorescent dextran-amines used as axonal tracers in the nervous system of the chicken embryo. J Neurosci Methods 18:243–254.

Golgi C (1873) Sulla struttura della sostanza grigia del cervello. Gazz Med Ital (Lombardia) 33:244–246.

Gong H, Zeng S, Yan C, Lv X, Yang Z, Xu T, Feng Z, Ding W, Qi X, Li A, Wu J, Luo Q (2013) Continuously tracing brain-wide long-distance axonal projections in mice at a one-micron voxel resolution. Neuroimage 74:87–98.

Grinevich V, Brecht M, Osten P (2005) Monosynaptic pathway from rat vibrissa motor cortex to facial motor neurons revealed by lentivirus-based axonal tracing. J Neurosci 25:8250–8258.

Grinevich V, Kolleker A, Eliava M, Takada N, Takuma H, Fukazawa Y, Shigemoto R, Kuhl D, Waters J, Seeburg PH, Osten P (2009) Fluorescent Arc/Arg3.1 indicator mice: a versatile tool to study brain activity changes *in vitro* and *in vivo*. J Neurosci Methods 184:25–36.

Harris JA, Wook Oh S, Zeng H (2012) Adeno-associated viral vectors for anterograde axonal tracing with fluorescent proteins in nontransgenic and cre driver mice. Curr Prot Neurosci (Crawley JN, et al., eds.), Chap 1, Unit 1.20, pp. 21–18.

Harvey CD, Collman F, Dombeck DA, Tank DW (2009) Intracellular dynamics of hippocampal place cells during virtual navigation. Nature 461:941–946.

Harvey CD, Coen P, Tank DW (2012) Choice-specific sequences in parietal cortex during a virtual-navigation decision task. Nature 484:62–68.

Hawrylycz M, Baldock RA, Burger A, Hashikawa T, Johnson GA, Martone M, Ng L, Lau C, Larson SD, Nissanov J, Puelles L, Ruffins S, Verbeek F, Zaslavsky I, Boline J (2011) Digital atlasing and standardization in the mouse brain. PLoS Comput Biol 7:e1001065.

Helmstaedter M (2013) Cellular-resolution connectomics: challenges of dense neural circuit reconstruction. Nat Methods 10:501–507.

Herrera DG, Robertson HA (1996) Activation of c-fos in the brain. Prog Neurobiol 50:83–107.

NOTES

Hintiryan H, Gou L, Zingg B, Yamashita S, Lyden HM, Song MY, Grewal AK, Zhang X, Toga AW, Dong HW (2012) Comprehensive connectivity of the mouse main olfactory bulb: analysis and online digital atlas. Front Neuroanat 6:30.

Holmgren C, Harkany T, Svennenfors B, Zilberter Y (2003) Pyramidal cell communication within local networks in layer 2/3 of rat neocortex. J Physiol 551:139–153.

Huber D, Gutnisky DA, Peron S, O'Connor DH, Wiegert JS, Tian L, Oertner TG, Looger LL, Svoboda K (2012) Multiple dynamic representations in the motor cortex during sensorimotor learning. Nature 484:473–478.

Huisken J, Swoger J, Del Bene F, Wittbrodt J, Stelzer EH (2004) Optical sectioning deep inside live embryos by selective plane illumination microscopy. Science 305:1007–1009.

Jones EG, Stone JM, Karten HJ (2011) High-resolution digital brain atlases: a Hubble telescope for the brain. Ann NY Acad Sci 1225(Suppl 1):E147–E159.

Kalchmair S, Jahrling N, Becker K, Dodt HU (2010) Image contrast enhancement in confocal ultramicroscopy. Opt Lett 35:79–81.

Keller PJ, Schmidt AD, Santella A, Khairy K, Bao Z, Wittbrodt J, Stelzer EH (2010) Fast, high-contrast imaging of animal development with scanned light sheet-based structured-illumination microscopy. Nat Methods 7:637–642.

Kitamura K, Judkewitz B, Kano M, Denk W, Hausser M (2008) Targeted patch–clamp recordings and single-cell electroporation of unlabeled neurons *in vivo*. Nat Methods 5:61–67.

Klausberger T, Somogyi P (2008) Neuronal diversity and temporal dynamics: the unity of hippocampal circuit operations. Science 321:53–57.

Ko H, Hofer SB, Pichler B, Buchanan KA, Sjöström PJ, Mrsic-Flogel TD (2011) Functional specificity of local synaptic connections in neocortical networks. Nature 473:87–91.

Koch C, Reid RC (2012) Neuroscience: observatories of the mind. Nature 483:397–398.

Lanciego JL, Wouterlood FG (2011) A half century of experimental neuroanatomical tracing. J Chem Neuroanat 42:157–183.

Lein ES, Hawrylycz MJ, Ao N, Ayres M, Bensinger A, Bernard A, Boe AF, Boguski MS, Brockway KS, Byrnes EJ, Chen L, Chen L, Chen TM, Chin MC, Chong J, Crook BE, Czaplinska A, Dang CN, Datta S, Dee NR, et al. (2007) Genome-wide atlas of gene expression in the adult mouse brain. Nature 445:168–176.

Leischner U, Zieglgansberger W, Dodt HU (2009) Resolution of ultramicroscopy and field of view analysis. PLoS ONE 4:e5785.

Li A, Gong H, Zhang B, Wang Q, Yan C, Wu J, Liu Q, Zeng S, Luo Q (2011) Micro-optical sectioning tomography to obtain a high-resolution atlas of the mouse brain. Science 330:1404–1408.

Llewellyn-Smith IJ, Martin CL, Arnolda LF, Minson JB (2000) Tracer-toxins: cholera toxin B-saporin as a model. J Neurosci Methods 103:83–90.

Lo L, Anderson DJ (2011) A Cre-dependent, anterograde transsynaptic viral tracer for mapping output pathways of genetically marked neurons. Neuron 72:938–950.

Madisen L, Zwingman TA, Sunkin SM, Oh SW, Zariwala HA, Gu H, Ng LL, Palmiter RD, Hawrylycz MJ, Jones AR, Lein ES, Zeng H (2010) A robust and high-throughput Cre reporting and characterization system for the whole mouse brain. Nat Neurosci 13:133–140.

Madisen L, Mao T, Koch H, Zhuo JM, Berenyi A, Fujisawa S, Hsu YW, Garcia AJ 3rd, Gu X, Zanella S, Kidney J, Gu H, Mao Y, Hooks BM, Boyden ES, Buzsáki G, Ramirez JM, Jones AR, Svoboda K, Han X, et al. (2012) A toolbox of Cre-dependent optogenetic transgenic mice for light-induced activation and silencing. Nat Neurosci 15:793–802.

Mank M, Santos AF, Direnberger S, Mrsic-Flogel TD, Hofer SB, Stein V, Hendel T, Reiff DF, Levelt C, Borst A, Bonhoeffer T, Hübener M, Griesbeck (2008) A genetically encoded calcium indicator for chronic *in vivo* two-photon imaging. Nat Methods 5:805–811.

Margrie TW, Meyer AH, Caputi A, Monyer H, Hasan MT, Schaefer AT, Denk W, Brecht M (2003) Targeted whole-cell recordings in the mammalian brain *in vivo*. Neuron 39:911–918.

Marshel JH, Mori T, Nielsen KJ, Callaway EM (2010) Targeting single neuronal networks for gene expression and cell labeling *in vivo*. Neuron 67:562–574.

Mayerich D, Abbott L, McCormick B (2008) Knife-edge scanning microscopy for imaging and reconstruction of three-dimensional anatomical structures of the mouse brain. J Microsc 231:134–143.

Mertz J, Kim J (2010) Scanning light-sheet microscopy in the whole mouse brain with HiLo background rejection. J Biomed Opt 15:016027.

Meyer HS, Wimmer VC, Oberlaender M, de Kock CP, Sakmann B, Helmstaedter M (2010) Number and laminar distribution of neurons in a thalamocortical projection column of rat vibrissal cortex. Cereb Cortex 20:2277–2286.

Meyer HS, Schwarz D, Wimmer VC, Schmitt AC, Kerr JN, Sakmann B, Helmstaedter M (2011) Inhibitory interneurons in a cortical column form hot zones of inhibition in layers 2 and 5A. Proc Natl Acad Sci USA 108:16807–16812.

Micheva KD, Smith SJ (2007) Array tomography: a new tool for imaging the molecular architecture and ultrastructure of neural circuits. Neuron 55:25–36.

Micheva KD, Busse B, Weiler NC, O'Rourke N, Smith SJ (2010) Single-synapse analysis of a diverse synapse population: proteomic imaging methods and markers. Neuron 68:639–653.

Miyamichi K, Amat F, Moussavi F, Wang C, Wickersham I, Wall NR, Taniguchi H, Tasic B, Huang ZJ, He Z, Callaway EM, Horowitz MA, Luo L (2011) Cortical representations of olfactory input by trans-synaptic tracing. Nature 472:191–196.

Moene IA, Subramaniam S, Darin D, Leergaard TB, Bjaalie JG (2007) Toward a workbench for rodent brain image data: systems architecture and design. Neuroinformatics 5:35–58.

Naumann T, Hartig W, Frotscher M (2000) Retrograde tracing with Fluoro-Gold: different methods of tracer detection at the ultrastructural level and neurodegenerative changes of back-filled neurons in long-term studies. J Neurosci Methods 103:11–21.

Ng L, Bernard A, Lau C, Overly CC, Dong HW, Kuan C, Pathak S, Sunkin SM, Dang C, Bohland JW, Bokil H, Mitra PP, Puelles L, Hohmann J, Anderson DJ, Lein ES, Jones AR, Hawrylycz M (2009) An anatomic gene expression atlas of the adult mouse brain. Nat Neurosci 12:356–362.

Niedworok CJ, Schwarz I, Ledderose J, Giese G, Conzelmann KK, Schwarz MK (2012) Charting monosynaptic connectivity maps by two-color light-sheet fluorescence microscopy. Cell Rep 2:1375–1386.

Oberlaender M, de Kock CP, Bruno RM, Ramirez A, Meyer HS, Dercksen VJ, Helmstaedter M, Sakmann B (2012) Cell type-specific three-dimensional structure of thalamocortical circuits in a column of rat vibrissal cortex. Cereb Cortex 22:2375–2391.

Odgaard A, Andersen K, Melsen F, Gundersen HJ (1990) A direct method for fast three-dimensional serial reconstruction. J Microsc 159:335–342.

O'Rourke NA, Weiler NC, Micheva KD, Smith SJ (2012) Deep molecular diversity of mammalian synapses: why it matters and how to measure it. Nat Rev Neurosci 13:365–379.

Osten P, Margrie TW (2013) Mapping brain circuitry with a light microscope. Nat Methods 10:515–523.

Paxinos G, Franklin KB (2004) The mouse brain in stereotaxic coordinates. Gulf Professional Publishing.

Petilla Interneuron Nomenclature Group, Ascoli GA, Alonso-Nanclares L, Anderson SA, Barrionuevo G, Benavides-Piccione R, Burkhalter A, Buzsáki G, Cauli B, Defelipe J, Fairén A, Feldmeyer D, Fishell G, Fregnac Y, Freund TF, Gardner D, Gardner EP, Goldberg JH, Helmstaedter M, Hestrin S, et al. (2008) Petilla terminology: nomenclature of features of GABAergic interneurons of the cerebral cortex. Nat Rev Neurosci 9:557–568.

Ragan T, Sylvan JD, Kim KH, Huang H, Bahlmann K, Lee RT, So PT (2007) High-resolution whole organ imaging using two-photon tissue cytometry. J Biomed Opt 12:014015.

Ragan T, Kadiri LR, Venkataraju KU, Bahlmann K, Sutin J, Taranda J, Arganda-Carreras I, Kim Y, Seung HS, Osten P (2012) Serial two-photon tomography for automated *ex vivo* mouse brain imaging. Nat Methods 9:255–258.

Ramón Y Cajal S (1904) Textura del sistema nervioso del hombre y de los vertebrados. Vol 2. Nicholas Moya.

Rancz EA, Franks KM, Schwarz MK, Pichler B, Schaefer AT, Margrie TW (2011) Transfection via whole-cell recording *in vivo*: bridging single-cell physiology, genetics and connectomics. Nat Neurosci 14:527–532.

NOTES

Reid RC (2012) From functional architecture to functional connectomics. Neuron 75:209–217.

Reijmers LG, Perkins BL, Matsuo N, Mayford M (2007) Localization of a stable neural correlate of associative memory. Science 317:1230–1233.

Reiner A, Veenman CL, Medina L, Jiao Y, Del Mar N, Honig MG (2000) Pathway tracing using biotinylated dextran amines. J Neurosci Methods 103:23–37.

Rockland KS, Pandya DN (1979) Laminar origins and terminations of cortical connections of the occipital lobe in the rhesus monkey. Brain Res 179:3–20.

Sands GB, Gerneke DA, Hooks DA, Green CR, Smaill BH, Legrice IJ (2005) Automated imaging of extended tissue volumes using confocal microscopy. Microsc Res Tech 67:227–239.

Song CK, Enquist LW, Bartness TJ (2005) New developments in tracing neural circuits with herpesviruses. Virus Res 111:235–249.

Song S, Sjöström PJ, Reigl M, Nelson S, Chklovskii DB (2005) Highly nonrandom features of synaptic connectivity in local cortical circuits. PLoS Biol 3:e68.

Sunkin SM, Ng L, Lau C, Dolbeare T, Gilbert TL, Thompson CL, Hawrylycz M, Dang C (2013) Allen Brain Atlas: an integrated spatio-temporal portal for exploring the central nervous system. Nucleic Acids Res 41:D996-D1008.

Swanson LW, Bota M (2010) Foundational model of structural connectivity in the nervous system with a schema for wiring diagrams, connectome, and basic plan architecture. Proc Natl Acad Sci USA 107:20610–20617.

Takatoh J, Nelson A, Zhou X, Bolton MM, Ehlers MD, Arenkiel BR, Mooney R, Wang F (2013) New modules are added to vibrissal premotor circuitry with the emergence of exploratory whisking. Neuron 77:346–360.

Taniguchi H, He M, Wu P, Kim S, Paik R, Sugino K, Kvitsiani D, Fu Y, Lu J, Lin Y, Miyoshi G, Shima Y, Fishell G, Nelson SB, Huang ZJ (2011) A resource of Cre driver lines for genetic targeting of GABAergic neurons in cerebral cortex. Neuron 71:995–1013.

Thompson RH, Swanson LW (2010) Hypothesis-driven structural connectivity analysis supports network over hierarchical model of brain architecture. Proc Natl Acad Sci USA 107:15235–15239.

Thomson AM, West DC, Wang Y, Bannister AP (2002) Synaptic connections and small circuits involving excitatory and inhibitory neurons in layers 2–5 of adult rat and cat neocortex: triple intracellular recordings and biocytin labelling *in vitro*. Cereb Cortex 12:936–953.

Tsai PS, Friedman B, Ifarraguerri AI, Thompson BD, Lev-Ram V, Schaffer CB, Xiong Q, Tsien RY, Squier JA, Kleinfeld D (2003) All-optical histology using ultrashort laser pulses. Neuron 39:27–41.

Tsai PS, Kaufhold JP, Blinder P, Friedman B, Drew PJ, Karten HJ, Lyden PD, Kleinfeld D (2009) Correlations of neuronal and microvascular densities in murine cortex revealed by direct counting and colocalization of nuclei and vessels. J Neurosci 29:14553–14570.

Ugolini G (1995) Specificity of rabies virus as a transneuronal tracer of motor networks: transfer from hypoglossal motoneurons to connected second-order and higher order central nervous system cell groups. J Comp Neurol 356:457–480.

Ugolini G (2010) Advances in viral transneuronal tracing. J Neurosci Methods 194:2–20.

Wall NR, Wickersham IR, Cetin A, De La Parra M, Callaway EM (2010) Monosynaptic circuit tracing *in vivo* through Cre-dependent targeting and complementation of modified rabies virus. Proc Natl Acad Sci USA 107:21848–21853.

Wallace DJ, Meyer zum Alten Borgloh S, Astori S, Yang Y, Bausen M, Kügler S, Palmer AE, Tsien RY, Sprengel R, Kerr JN, Denk W, Hasan MT (2008) Single-spike detection *in vitro* and *in vivo* with a genetic Ca^{2+} sensor. Nat Methods 5:797–804.

Wickersham IR, Feinberg EH (2012) New technologies for imaging synaptic partners. Curr Opin Neurobiol 22:121–127.

Wickersham IR, Finke S, Conzelmann KK, Callaway EM (2007a) Retrograde neuronal tracing with a deletion-mutant rabies virus. Nat Methods 4:47–49.

Wickersham IR, Lyon DC, Barnard RJ, Mori T, Finke S, Conzelmann KK, Young JA, Callaway EM (2007b) Monosynaptic restriction of transsynaptic tracing from single, genetically targeted neurons. Neuron 53:639–647.

Young JA, Bates P, Varmus HE (1993) Isolation of a chicken gene that confers susceptibility to infection by subgroup A avian leukosis and sarcoma viruses. J Virol 67:1811–1816.

CLARITY and Beyond: Tools for Integrated Brain Mapping

Kwanghun Chung, PhD

Institute of Medical Engineering and Science
Department of Chemical Engineering
Picower Institute for Learning and Memory
Massachusetts Institute of Technology
Cambridge, Massachusetts

Introduction

A major challenge in biology remains obtaining detailed high-resolution information from a complex system while maintaining the global perspective needed to understand system function. Here we address this challenge using the CLARITY method for efficient transformation of intact tissue into a nanoporous hydrogel-hybridized form (cross-linked to a three-dimensional [3D] network of hydrophilic polymer chains) that is fully assembled but optically transparent and macromolecule-permeable. We demonstrate transformation of rodent brains using this method, which enables intact-tissue imaging of many elements: long-range circuit projections, local circuit wiring, cellular relationships, subcellular structures, protein complexes, nucleic acids, and neurotransmitters. We also show how CLARITY is compatible with both immunocytochemistry and *in situ* hybridization in nonsectioned tissue, enabling the delivery and retrieval of exogenous macromolecules throughout the intact mouse brain for molecular phenotyping and allowing sequential rounds of staining and destaining. Finally, we demonstrate that CLARITY enables fine-structural analysis of clinical samples, including nonsectioned human tissue banked for years in formalin from a psychiatric disease clinical setting. These capabilites open the door to transmuting human tissue into a physically stable, intact form suitable for probing the structural and molecular underpinnings of physiological function and disease.

Extracting detailed structural and molecular information from intact biological systems has long been a fundamental challenge across fields of investigation and has spurred considerable technological innovation (Denk et al., 1990; Helmchen and Denk, 2005; Dodt et al., 2007; Livet et al., 2007; Micheva and Smith, 2007; Li et al., 2010; Susaki et al., 2014). In particular, the study of brain structure–function relationships may benefit from intact-system tools (Kasthrui and Lichtman, 2007; Defelipe, 2010); in general, much valuable information on intrasystem relationships and joint statistics will become accessible from undertaking the full structural analysis of intact systems rather than piecemeal reconstruction across preparations. Yet even tissue structure in itself provides only a certain level of insight without detailed molecular phenotyping, which is difficult to achieve within intact tissue.

We have set the goal of rapidly transforming intact tissue into an optically transparent and macromolecule-permeable construct while preserving native molecular information and structure. We took note of the fact that packed lipid bilayers are implicated in rendering tissue poorly accessible both to molecular probes and to photons; these bilayers simultaneously create diffusion-barrier properties relevant to chemical penetration and light-scattering properties at the lipid-aqueous interface. Thus, we reasoned that if lipid bilayers could be removed nondestructively, light and macromolecules might penetrate deep into tissue, allowing 3D imaging and immunohistological analysis without disassembly. However, removing lipid membranes that provide structural integrity and retain biomolecules would inevitably damage tissue with profound loss of cellular and molecular information. Therefore, first providing a physical framework would be required to physically support the tissue and secure biological information.

Hydrogel–Electrophoretic Tissue Transmutation

We began providing a physical framework for the tissue by infusing hydrogel monomers (here, acrylamide and bisacrylamide), formaldehyde, and thermal initiators into tissue at 4°C (Fig. 1). In this step, formaldehyde not only cross-links the tissue but also covalently links the hydrogel monomers to biomolecules, including proteins, nucleic acids, and small molecules. Next, polymerization of the biomolecule-conjugated monomers into a hydrogel mesh is thermally initiated by incubating infused tissue at 37°C for 3 h, at which point tissue and hydrogel become a hybrid construct. This hydrogel–tissue hybridization physically supports tissue structure and chemically incorporates biomolecules into the hydrogel mesh. Importantly, lipids and biomolecules lacking functional groups for conjugation remain unbound and therefore can be removed from the hybrid. To efficiently extract lipids, we developed an active-transport organ electrophoresis approach, which we termed ETC (electrophoretic tissue clearing), capitalizing on the highly charged nature of ionic micelles. This method expedites lipid extraction by orders of magnitude.

Whole Adult Mouse Brain Imaging

To test anticipated features of the technology, we used CLARITY to process the brain of a 3-month-old *Thy1*-EYFP line-H mouse, in which the cytosolic fluorescent protein enhanced yellow fluorescent protein (EYFP) is expressed in projection neurons (Feng et al., 2000). Within 8 d, the intact adult brain was transmuted into a lipid-extracted and structurally stable hydrogel–tissue hybrid. Scattering still occurs owing to heterogeneously distributed protein/nucleic acid complexes in the hybrid. However,

NOTES

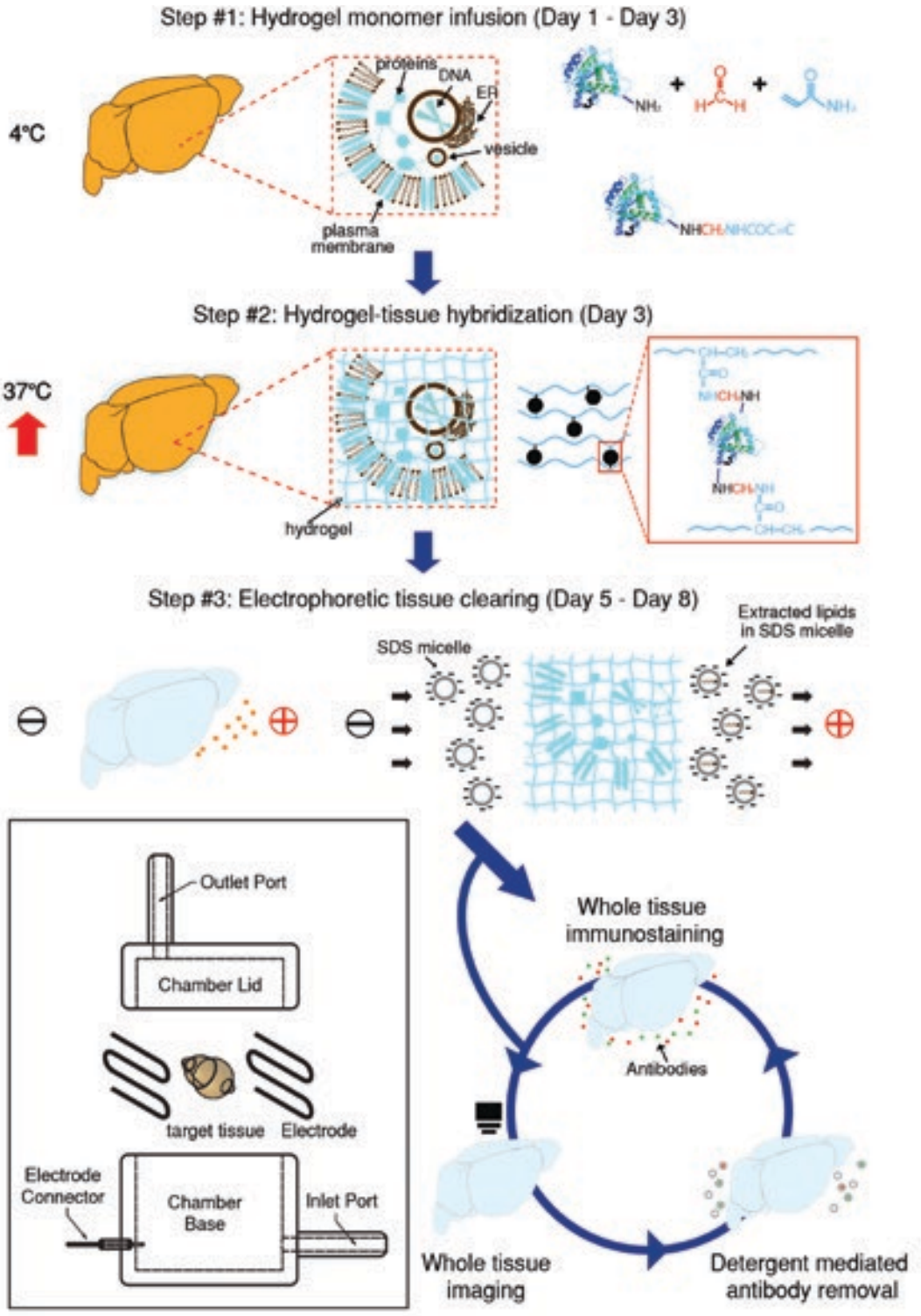

Figure 1. CLARITY. Tissue is cross-linked with formaldehyde (red) in the presence of hydrogel monomers (blue), covalently linking tissue elements to monomers, which are then polymerized into a hydrogel mesh. Electric fields applied across the sample in ionic detergent actively transport micelles into (and lipids out of) the tissue, leaving fine structure and cross-linked biomolecules in place. Bottom left boxed region, ETC chamber. Reprinted with permission from Chung et al. (2013), their Fig. 1.

after immersion in refractive index (RI)–specified solutions matching the CLARITY hybrid (e.g., 85% glycerol or FocusClear, both RI ~1.45), the intact brain becomes uniformly transparent (Figs. 2*a–c*).

Imaging depth in clarified tissue appeared to be limited only by working distance (WD) of the objective (here 3.6 mm, though 8 mm WD/0.9 NA objectives are available). Therefore, to image the 5- to 6-mm-thick adult mouse brain, we next imaged the dorsal half of the brain followed by inversion and imaging of the ventral half (Fig. 2*d*, *e*). Figure 2*f* shows a volume of unsectioned mouse brain with visualization through cortex, hippocampus, alveus, and thalamus (Fig. 2*g–l*). We observed that tissue expanded slightly with ETC and returned to original size after RI matching. This transient change did not cause net tissue deformation, and fine structural details such as membrane-localized

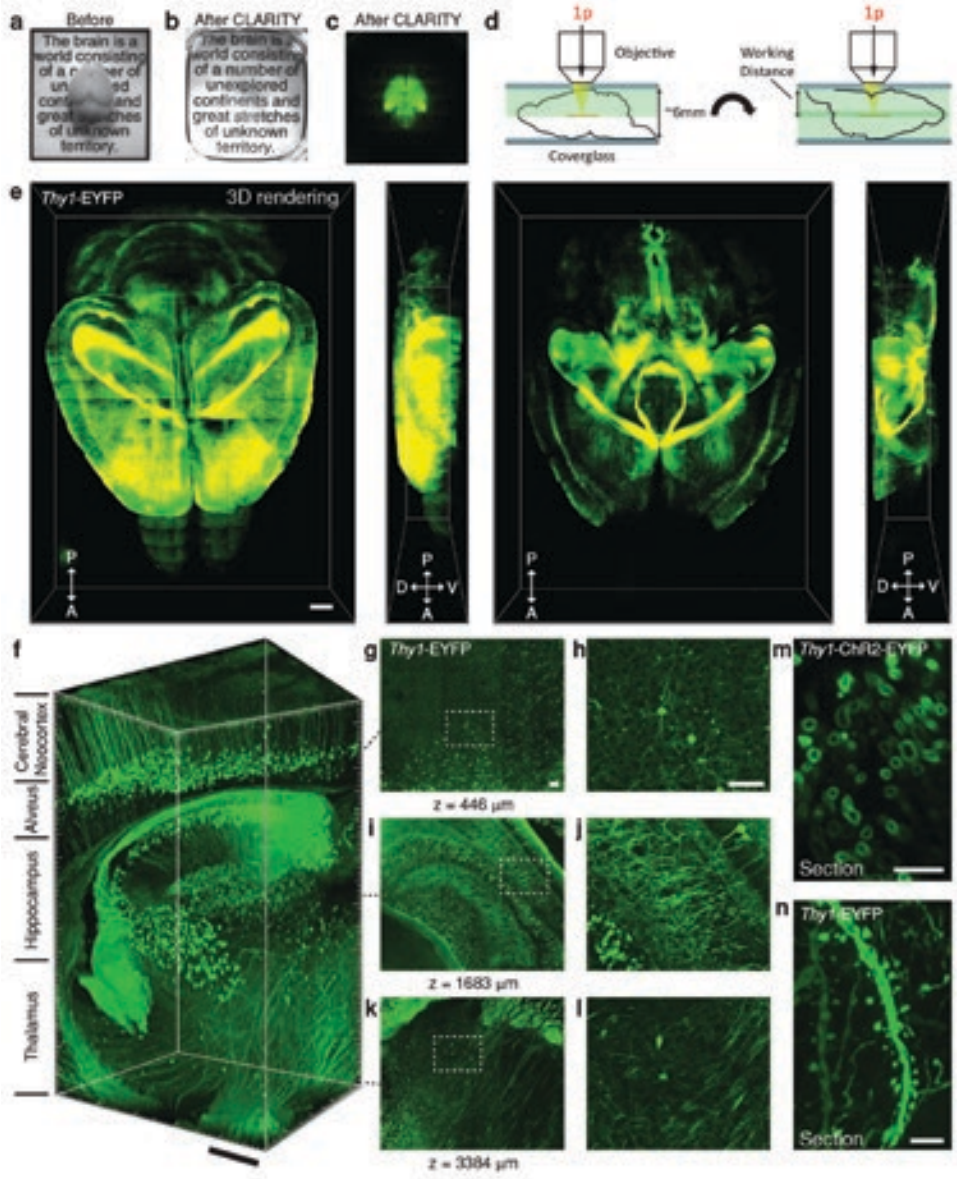

Figure 2. Intact adult mouse brain imaging. ***a–d***, Whole mouse brains (3 months old): ***a,*** before CLARITY (quote from Ramón Y Cajal, 1904); ***b***, after CLARITY. *Thy1*–eYFP line-H mouse brain after hydrogel–tissue hybridization, ETC, and refractive-index matching. ***c***, Fluorescence image of brain in ***b. d***, Dorsal aspect is imaged using single-photon (1p) microscopy, then the brain is inverted and ventral aspect imaged. ***e***, 3D rendering of clarified mouse brain. Left, dorsal half; Right, ventral half. Scale bar, 1 mm. ***f***, Nonsectioned mouse brain tissue showing cortex, hippocampus, and thalamus. Scale bar, 400 μm. (***g–l***). Optical sections from ***f*** showing negligible resolution loss even at ~3400 μm depth. ***g, h,*** z = 446 μm; i, j, z = 1683 μm; ***k, l,*** z = 3384 μm. ***h, j***, and ***l***, Boxed regions in ***g, i,*** and ***k***. Scale bars, 100 μm. ***m***, Cross-section of axons in clarified striatum of *Thy1*-ChR2-EYFP line: membrane-localized ChR2-EYFP. Scale bar, 5 μm. ***n***, Dendrites and spines of neurons in clarified *Thy1*-EYFP line-H cortex. Scale bar, 5 μm. Reprinted with permission from Chung et al. (2013), their Fig. 2.

NOTES

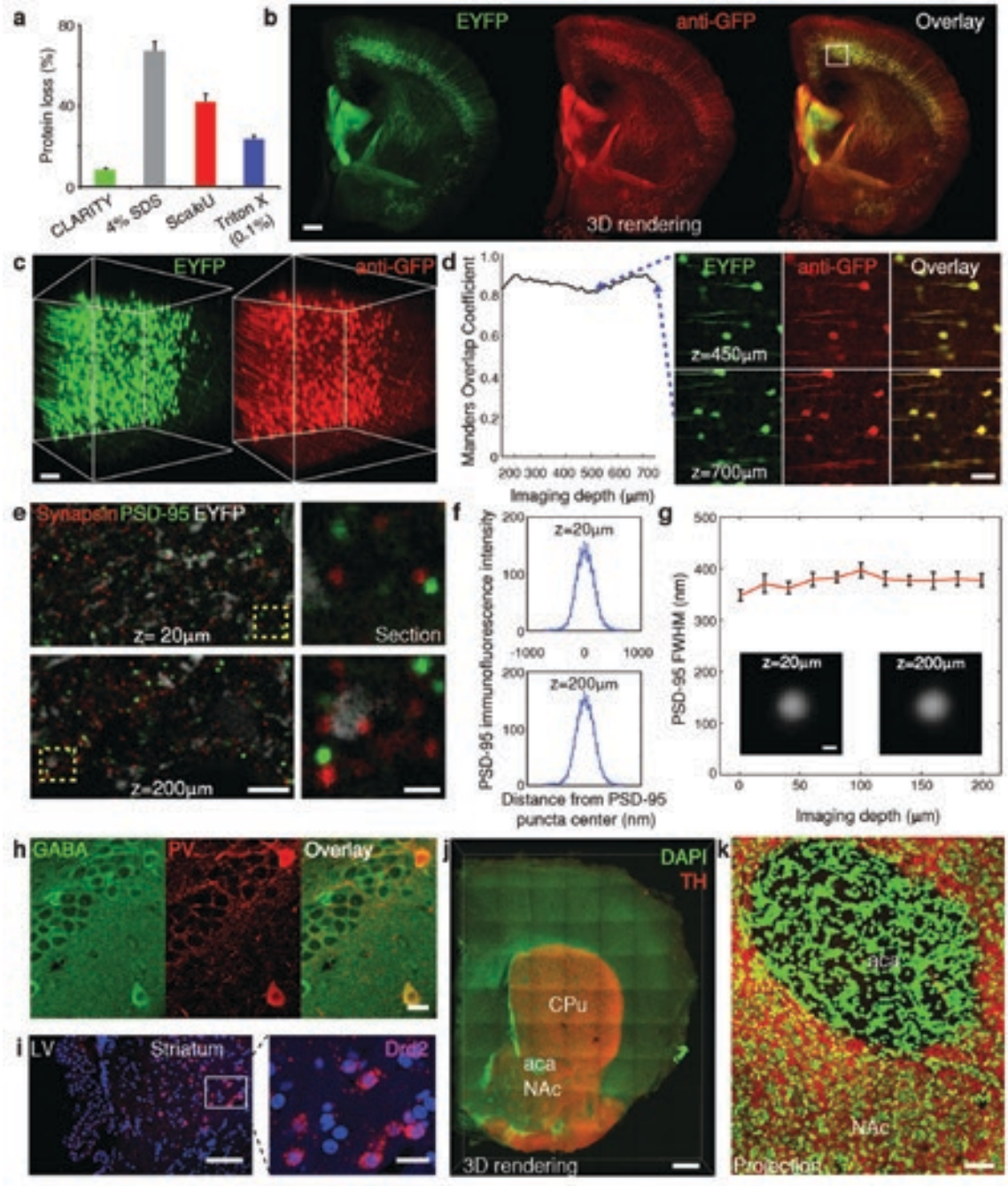

Figure 3. Molecular phenotyping in intact tissue. ***a***, Protein loss percentages in clarified mouse brain compared with conventional methods; $n = 4$ for each condition. ***b***, Rendering of 1-mm-thick, nonsectioned coronal block of *Thy1*-EYFP mouse immunostained for GFP. Scale bar, 500 μm. ***c***, 3D rendering of boxed region in cortex in ***b*** shows EYFP fluorescence (left) and anti-GFP staining (right). ***d***, Left, Colocalization of GFP staining. Right, Optical sections at different depths in 3D rendering. Scale bar, 100 μm. ***e–f***, 500-μm-thick block of line-H brain immunostained for synapsin-I (red)/PSD-95 (blue) for 3 *d*. ***e***, Left, Optical sections. Right, enlarged images of boxed regions on left. Individual synaptic puncta resolved throughout depth. EYFP: white. ***f***, Average immunofluorescence cross-section of PSD-95 puncta. ***g***, Full width at half maximum (FWHM) of average immunofluorescence cross-section of PSD-95 puncta versus depth. Insets: average puncta at $z = 20$ μm, $z = 200$ μm. ***h***, Staining in hippocampus. Left, GABA; middle, PV; right, overlay. Scale bar, 20 μm. ***i***, *In situ* hybridization in clarified 500 μm mouse brain block showing dopamine receptor D2 (Drd2) mRNA in striatum. LV, lateral ventricle. Blue, DAPI. Scale bars: Left, 100 μm; Right, 20 μm. ***j, k,*** Axonal fibers of TH-positive neurons in NAc and CPu. ***j,*** 3D rendering of 1-mm-thick clarified mouse brain block stained for TH (red) and DAPI (green). aca, anterior commissure. Scale bar, 500 μm. ***k***, Maximum projection, NAc/aca volume in ***j***. Scale bar, 50 μm. Reprinted with permission from Chung et al. (2013), their Fig. 3.

proteins (Fig. 2*m*), dendritic spines (Fig. 2*n*), and synaptic puncta (Fig. 3*e–g*) remained securely in place.

Molecular Phenotyping of Intact Tissue Volumes

Interrogating molecular features at subcellular resolution in an intact brain with known global wiring properties may be of value; however, conventional labeling techniques involve (1) loss of native molecules after permeabilization required for access to intracellular targets, (2) time-intensive thin sectioning and reconstruction, or (3) when multiple rounds of labeling are attempted, damage due to harsh probe removal processes. We hypothesized that CLARITY could overcome these three major difficulties by enabling intact-tissue and multiple-round molecular phenotyping.

First, CLARITY may preserve native antigens with unusual completeness owing to the hydrogel-hybridization process. To quantify molecular preservation associated with tissue–hydrogel fusion, we compared protein loss in clarified mouse brain to loss from conventional methods (Fig. 3*a*). Of total protein, ~65% was solubilized (lost) when conventionally PFA-fixed tissue blocks were cleared by 4% SDS for one week. Scale, a tissue-clearing method using 4M urea, allowed ~41% protein loss over the same interval. Even PFA-fixed tissue treated only with 0.1% Triton X-100/PBS, a mild detergent–based permeabilization buffer used in conventional histology, allowed significant loss of ~24% protein. However, when hydrogel-hybridized tissue was cleared with the stringent 4% SDS solution of CLARITY, only ~8% protein loss was seen, indicating that chemical tethering of biomolecules into hydrogel mesh can enhance the preservation of molecular components.

Second, we found that CLARITY, which increases tissue permeability by replacing lipid bilayers with nanoporous hydrogel, enables rapid diffusion of molecular probes deep into intact tissue, and thereby allows access to preserved biomolecules without sectioning. In a 1-mm-thick clarified coronal block of mouse brain, uniformly antibody-stained over 3 d (Fig. 3*b*), quantitative colocalization analysis revealed that EYFP fluorescence and anti–green fluorescent protein (GFP) staining overlapped throughout the block (Figs. 3*c*, *d*).

Third, CLARITY was found to enable multiround molecular phenotyping (Fig. 4); the stable framework allowed effective removal of antibodies without fine-structural damage or degraded antigenicity. We performed three consecutive rounds of staining in 1-mm-thick coronal blocks from a *Thy1*-EYFP H-line mouse brain, observing effective antibody removal and preserved EYFP-positive neuronal morphology as well as restaining capability. Although extensive validation would be required to fully map the extent to which CLARITY secures molecular information, this result demonstrates that elution largely preserves integrity of tissue structure, cellular architecture, fluorescence signals (Figs. 3*d–f*), and diamino-phenyl-indol (DAPI) DNA staining (Fig. 3*g*). Moreover, repeated TH staining in the first and third rounds revealed identical staining patterns and signal intensity, confirming that antigenicity is retained throughout multiple rounds of staining/elution. To investigate axonal projections of the tyrosine hydroxylase (TH) neurons further, we clarified 1-mm-thick coronal blocks of mouse brain that were stained and imaged using tyrosine hydroxylase. As shown in Figures 3*j* and *k*, projections of tyrosine hydroxylase–positive fibers were readily visualized in the neocortex, nucleus accumbens, caudate putamen, and amygdala. We also found that the CLARITY hydrogel-conjugation process preserves small molecules, such as the neurotransmitter GABA (Fig. 3*h*).

Human Tissue Imaging and Molecular Phenotyping

We found that CLARITY functioned in long-banked human brain, enabling immunohistological visualization and identification of neurons and projections over large volumes (Figs. 5*a–g*). In 0.5-mm-thick blocks of frontal lobe from an autistic patient, stored in formalin for >6 years, we were able to stain for axons with neurofilament protein (NP) and myelin basic protein (MBP) and to trace individual fibers (Fig. 5*e*). In addition, by staining for parvalbumin (PV), we could visualize the distribution of PV-positive interneurons in neocortex over large volumes (6.7 × 4.7 × 0.5 mm) and trace individual PV-labeled processes (Figs. 5*g–n*).

Unlike mechanical sectioning methods, which may involve deformation of tissue and uncertainty in registration across sections, CLARITY preserves continuity of structure, which not only allows tracing of neurites over distances but also provides a class of distinct information about the morphology of traced neurons. As one example, we found that many PV-positive interneurons in this human sample, selectively in deep layers, displayed isoneuronal and heteroneuronal dendritic bridges (Figs. 5*g–m*). These ladder-like connections (not typical of control brain) instead resemble abnormalities observed with mutations in the Down syndrome cell-adhesion molecule (Dscam) protein or protocadherins

NOTES

(Pcdhs); mutations in the latter family are associated with autism-spectrum disorder (Morrow et al., 2008). Although extensive work would be required to define the incidence and implications of abnormal PV neurons, the observation illustrates the structural and molecular capability that clarified tissue provides by virtue of volumetric continuity, which may help shed light on the structural underpinnings of neuropsychiatric disease (de Anda et al., 2012).

Discussion

Using this hydrogel–tissue fusion and ETC technology, intact tissue can be rapidly transformed into optically and chemically accessible form while retaining structural and molecular information, thereby enabling the imaging of entire adult vertebrate brains as well as multiple-round molecular phenotyping without thin sectioning. CLARITY-optimized long-WD objectives will improve imaging

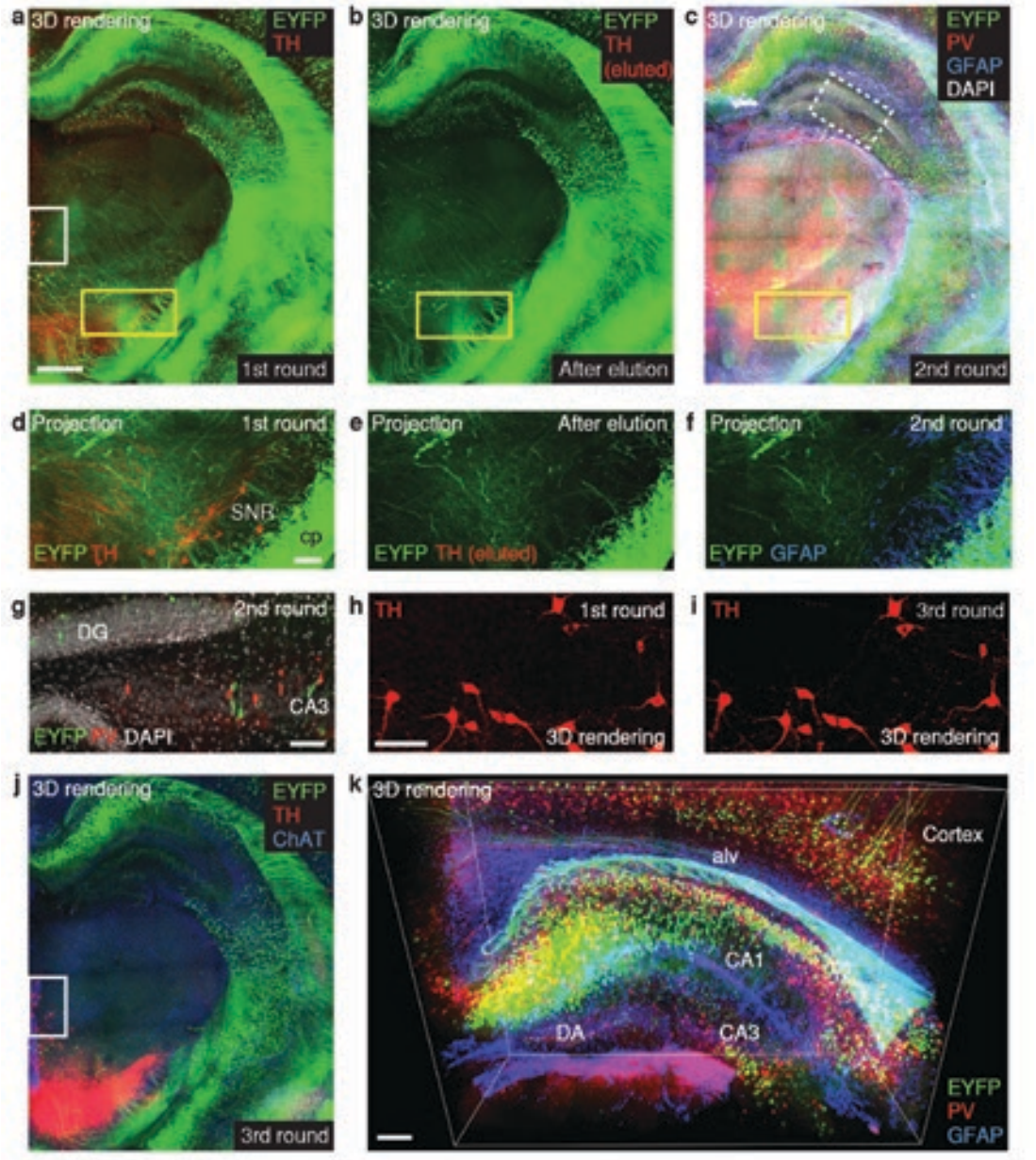

Figure 4. Multiround molecular phenotyping of intact tissue. ***a***, First round. Volume rendering of 1-mm-thick block of *Thy1*-EYFP mouse immunostained for TH in nonsectioned form. Scale bar, 500 µm. ***b***, Antibodies eluted from block in ***a***. ***c,*** Second round. 3D rendering of same block now immunostained for PV (red)/GFAP (blue)/DAPI (white). ***d–f***, Maximum projections of 100 µm volume of yellow-boxed region in ***a, b,*** and ***c,*** respectively. Scale bar, 100 µm. ***g***, Optical section of white/dotted-box region in ***c*** showing DAPI. CA, cornu ammonis; DG, dentate gyrus. Scale bar, 100 µm. ***h–i***, TH channel of white-box region in ***a*** (***h***) and ***j*** (***i***). TH antigenicity preserved through multiple elutions. Scale bar, 100 µm. ***j***, Third round. Block in ***a–c*** immunostained for TH (red) and choline acetyltransferase (ChAT) (blue). ***k***, 3D view of hippocampus in ***c*** showing EYFP-expressing neurons (green)/PV-positive neurons (red)/GFAP (blue). Scale bar, 200 µm. Alv, alveus. Reprinted with permission from Chung et al. (2013), their Fig. 4.

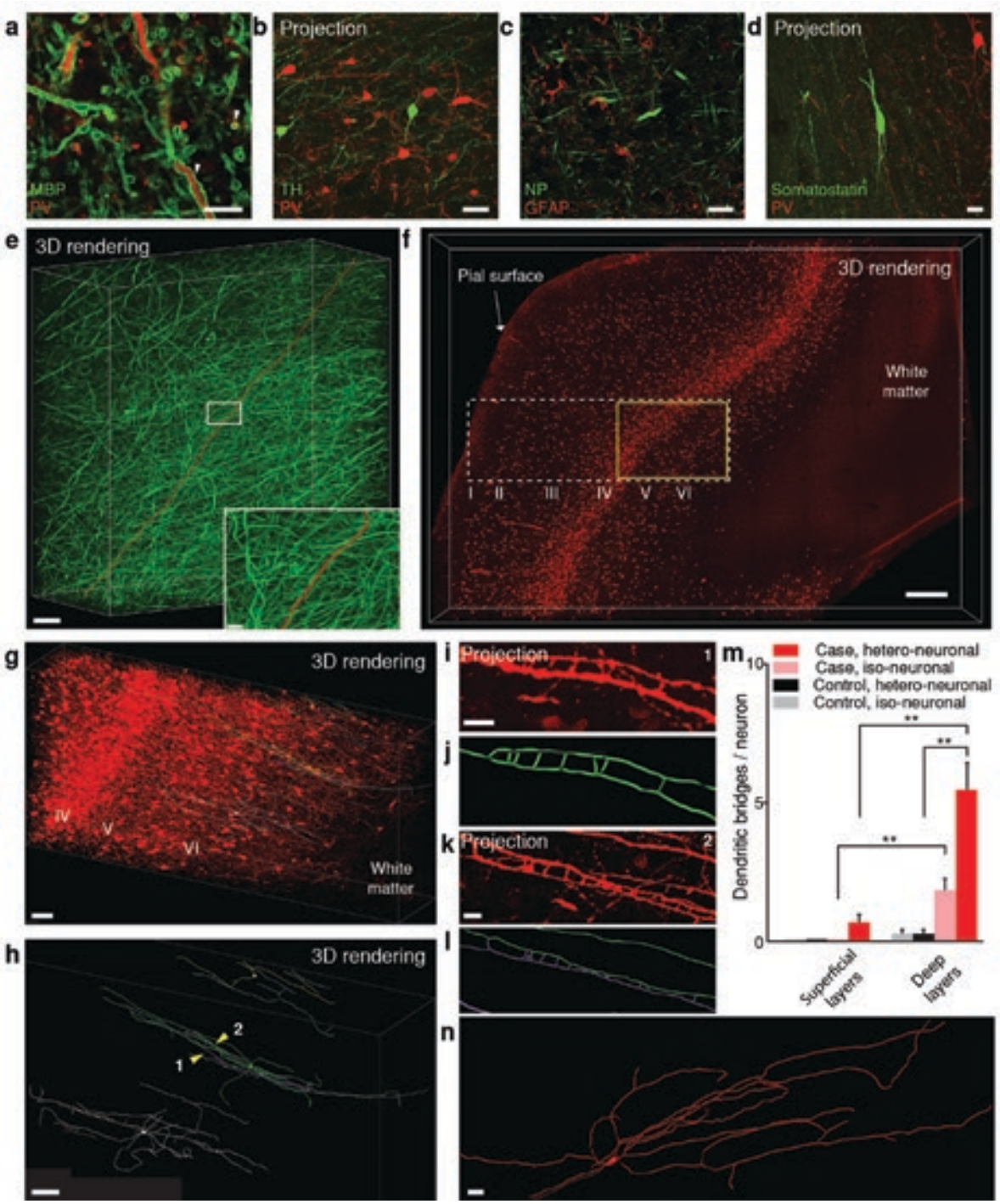

Figure 5. Human brain structural/molecular phenotyping. Human BA10 500-µm-thick intact blocks. ***a***, Optical section: myelin basic protein (MBP)/PV staining. White arrowheads indicate membrane-localized MBP around PV-positive projections. Scale bar, 10 µm. ***b***, TH and PV staining. Scale bar, 50 µm. ***c***, Optical section: NP and GFAP. Scale bar, 20 µm. ***d***, Somatostatin and PV staining. Scale bar, 20 µm. ***e***, Rendering of NP-positive axonal fibers. Red, traced axon across volume. Scale bar, 500 µm. Inset: boxed region. Scale bar, 20 µm. ***f***, Visualization of PV-positive neurons in neocortex of autism case (Morrow et al., 2008). Scale bar, 500 µm. ***g***, Yellow-boxed region in ***f*** showing PV-positive cell bodies and fibers in layers IV, V, and VI. Scale bar, 100 µm. ***h***, 3D rendering of abnormal neurons in ***g***. Yellow arrowheads (1, 2) indicate ladder-shaped structures shown below in ***i*** and ***k***. Scale bar, 80 µm. ***i***, Zoomed-in maximum projection of 8 µm volume showing morphology of ladder-shaped structure formed by neurites from a single neuron. Scale bar, 10 µm. ***j***, Tracing of structure in ***i***. ***k***, Maximum projection of 18 µm volume showing ladder-shaped structure formed by neurites from 2 different neurons. Scale bar, 10 µm. ***l***, Tracing of structure in ***k***. ***m***, Isoneuronal and heteroneuronal dendritic bridges per neuron. $^{**}p<0.05$; error bars indicate SEM; $n = 6$ neurons for both superficial and deep layers of autism case; $n = 4$ neurons for both superficial and deep layers of control case. ***n***, 3D reconstruction of a neuron in layer 2 (superficial) of the autism case. Scale bar, 10 µm. Reprinted with permission from Chung et al. (2013), their Fig. 5.

NOTES

depth and resolution, further enhancing the acquisition of integrated structural and molecular information from intact systems.

Turning immense datasets into useful insights remains a key challenge. Computational approaches to image segmentation, 3D registration, and automated tracing require further development. Although much remains to be refined, new approaches to intact-systems biology may dovetail with existing optogenetic-control or activity-imaging methods. Moreover, efficient molecular phenotyping (as with c-Fos) may help map populations with altered activity downstream of the directly modulated population, across the same intact brain. Together with its capability for intersectional definition of cells via sequential rounds of labeling, and broad application domain (including mouse, zebrafish, and human), these data suggest that CLARITY provides access to structural and molecular information that may help support a newly integrative understanding of large-scale intact biological systems.

Acknowledgments

This chapter was adapted and excerpted from a previously published article: Chung et al. (2013), Structural and molecular interrogation of intact biological systems, Nature 497:332–337.

References

Chung K, Wallace J, Kim SY, Kalyanasundaram S, Andalman AS, Davidson TJ, Mirzabekov JJ, Zalocusky KA, Mattis J, Denisin AK, Pak S, Bernstein H, Ramakrishnan C, Grosenick L, Gradinaru V, Deisseroth K (2013) Structural and molecular interrogation of intact biological systems. Nature 497:332–337.

de Anda FC, Rosario AL, Durak O, Tran T, Graff J, Meletis K, Rei D, Soda T, Madabhushi R, Ginty DD, Kolodkin AL, Tsai LH (2012) Autism spectrum disorder susceptibility gene *TAOK2* affects basal dendrite formation in the neocortex. Nat Neurosci 15:1022–1031.

DeFelipe J (2010) From the connectome to the synaptome: an epic love story. Science 330:1198–1201.

Denk W, Strickler JH, Webb WW (1990) Two-photon laser scanning fluorescence microscopy. Science 248:73–76.

Dodt H, Leischner U, Schierloh A (2007) Ultramicroscopy: three-dimensional visualization of neuronal networks in the whole mouse brain. Nat Methods 4:331–336.

Feng G, Mellor RH, Bernstein M, Keller-Peck C, Nguyen QT, Wallace M, Nerbonne JM, Lichtman JW, Sanes JR (2000) Imaging neuronal subsets in transgenic mice expressing multiple spectral variants of GFP. Neuron 28:41–51.

Helmchen F, Denk W (2005) Deep tissue two-photon microscopy. Nat Methods 2:932–940.

Kasthuri N, Lichtman JW (2007) The rise of the "projectome." Nat Methods 4:307–308.

Li A, Gong H, Zhang B, Wang Q, Yan C, Wu J, Liu Q, Zeng S, Luo Q (2010) Micro-optical sectioning tomography to obtain a high-resolution atlas of the mouse brain. Science 330:1404–1408.

Livet J, Weissman TA, Kang H, Draft RW, Lu J, Bennis RA, Sanes JR, Lichtman JW (2007) Transgenic strategies for combinatorial expression of fluorescent proteins in the nervous system. Nature 450:56–62.

Micheva KD, Smith SJ (2007) Array tomography: a new tool for imaging the molecular architecture and ultrastructure of neural circuits. Neuron 55:25–36.

Morrow EM, Yoo SY, Flavell SW, Kim TK, Lin Y, Hill RS, Mukaddes NM, Balkhy S, Gascon G, Hashmi A, Al-Saad S, Ware J, Joseph RM, Greenblatt R, Gleason D, Ertelt JA, Apse KA, Bodell A, Partlow JN, Barry B, et al. (2008) Identifying autism loci and genes by tracing recent shared ancestry. Science 321:218–23.

Ramón Y Cajal S (1904) Textura del sistema nervioso del hombre y de los vertebrados. Vol 2. Nicholas Moya.

Susaki EA, Tainaka K, Perrin D, Kishino F, Tawara T, Watanabe TM, Yokoyama C, Onoe H, Eguchi M, Yamaguchi S, Abe T, Kiyonari H, Shimizu Y, Miyawaki A, Yokota H, Ueda HR (2014) Whole-brain imaging with single-cell resolution using chemical cocktails and computational analysis. Cell 157:726–739.

Advanced CLARITY Methods for Rapid and High-Resolution Imaging of Intact Tissues

Raju Tomer, PhD, and Karl Deisseroth, PhD

Department of Bioengineering
Department of Psychiatry and Behavioral Sciences
CNC Program, Howard Hughes Medical Institute
Stanford University
Stanford, California

Introduction

CLARITY is a method for chemical transformation of intact biological tissues into a hydrogel-tissue hybrid, which becomes amenable to interrogation with light and macromolecular labels while retaining fine structure and native biological molecules. This emerging accessibility of information from large intact samples has created both new opportunities and new challenges. In this chapter, we describe next-generation methods spanning multiple dimensions of the CLARITY workflow. These methods range from a novel approach to simple, reliable, and efficient lipid removal without electrophoretic instrumentation (passive CLARITY), to optimized objectives and integration with light-sheet optics (CLARITY-optimized light-sheet microscopy, or COLM) for accelerating data collection from clarified samples by several orders of magnitude while maintaining or increasing quality and resolution. These methods may find application in the structural and molecular analysis of large assembled biological systems such as the intact mammalian brain.

One goal of modern neuroscience is to map the architecture of neural circuits with both high (wiring-level) resolution and broad (brainwide) perspective. This challenge has drawn the attention of generations of scientists, beginning with Ramón Y Cajal's detailed representations of neurons visualized at high resolution with the Golgi staining technique while embedded within semi-intact brain tissue (Ramón Y Cajal, 1904). Principles fundamental to the understanding of neural systems can result from such an integrative approach, but although progress has been made, many challenges and opportunities remain.

Over the last few decades, electron microscopy (EM) has emerged as a foundational method for deciphering details of neuronal circuit structure (Bock et al., 2011; Briggman et al., 2011; Kim et al., 2014). The key advantage of EM in this regard (relative to light microscopy) is the identification of presynaptic active zones containing neurotransmitter vesicles apposed to postsynaptic structures. In addition, EM facilitates visualization of some of the very finest branches of axons. However, EM tissue mapping requires relatively slow steps involving ultrathin sectioning/ablation and reconstruction; most importantly, the sample contrast preparation is largely incompatible with rich molecular phenotyping that could provide critical information on cell and synapse type. Ideally, datasets resulting from intact-brain mapping should be linkable to molecular information on the types of cells and synapses that are imaged structurally, and even to dynamical information on natural activity pattern history (in these same circuits) known to be causally relevant to animal behavior. Suitable light-based imaging approaches, combined with specific genetic or histochemical molecular labeling methods, have emerged as important tools for visualizing the structural, molecular, and functional architecture of biological tissues, with a particularly vital role to play in emerging brainwide, high-resolution neuroanatomy.

Confocal methods revolutionized light microscopy by enabling optical sectioning in thick (tens of micrometers) fluorescently labeled samples, thereby allowing three-dimensional (3D) reconstruction without the need for ultrathin physical sectioning. (Conchello and Lichtman, 2005). Two-photon microscopy further increased the accessible imaging depth (to hundreds of micrometers) even in living tissue samples (Helmchen and Denk, 2005), and adaptive-optics approaches have improved imaging depth further (Tang et al., 2012). However, light microscopy remains limited for imaging throughout intact vertebrate nervous systems. (For example, mouse brains span many millimeters even in the shortest spatial dimension, and are opaque on this scale owing chiefly to light scattering.)

As a step in this direction, new methods have emerged to increase tissue transparency (Dodt et al., 2007; Hama et al., 2011; Ke et al., 2013) by chemically reducing the scattering of light traveling through the tissue sample. Although intriguing and effective, these approaches are not generally suitable for detailed molecular phenotyping, since most tissues (e.g., the intact mature brain) remain largely impenetrable to macromolecular antibody or oligonucleotide labels. These limitations motivated the recent development of CLARITY (Chung et al., 2013; Tomer et al., 2014), which involves the removal of lipids in a stable hydrophilic chemical environment to achieve transparency of intact tissue, preservation of ultrastructure and fluorescence, and accessibility of native biomolecular content to antibody and nucleic acid probes.

Clarifying Large Tissue Volumes

CLARITY builds on chemical principles to grow hydrogel polymers from inside the tissue in order to provide a support framework for structural and biomolecular content (Fig. 1). This is achieved first by infusing a cold (4°C) cocktail of hydrogel monomers (for example, acrylamide with bisacrylamide), formaldehyde, and thermally triggered initiators into the tissue, followed by polymerization of the hydrogel at 37°C. Formaldehyde serves the dual purposes of cross-linking amine-containing tissue components to each other, as well as covalently binding the hydrogel monomers to these native biomolecules, which include

NOTES

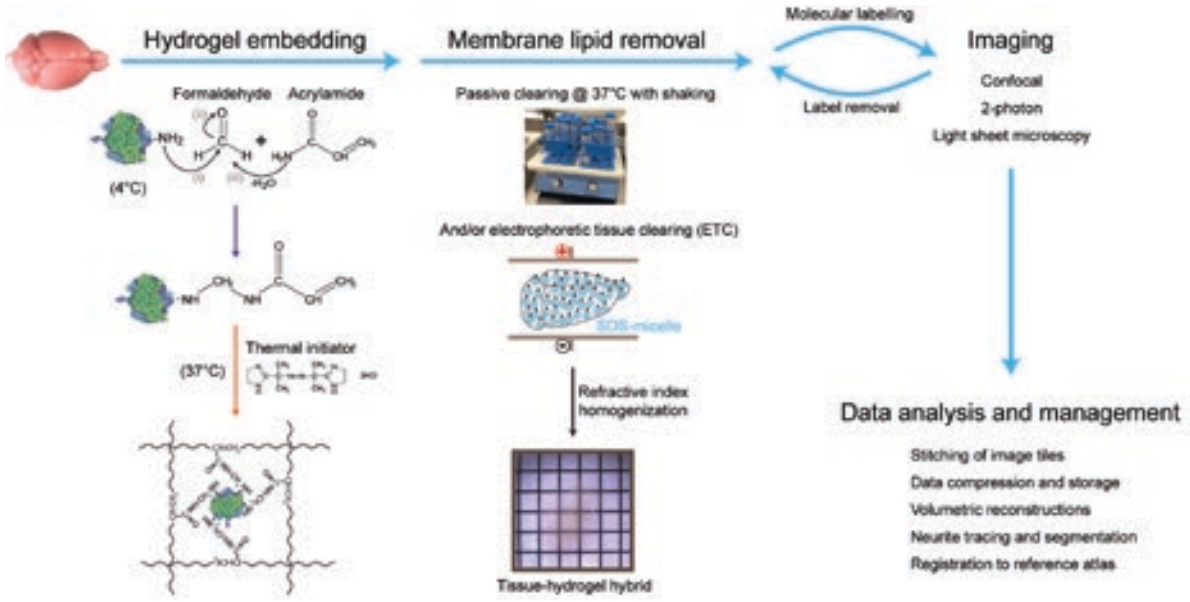

Figure 1. CLARITY pipeline overview. The tissue sample, e.g., an intact mouse brain, is perfused with cold hydrogel monomer solution that contains a cocktail of acrylamide, bisacrylamide, formaldehyde, and thermal initiator. Formaldehyde mediates cross-linking of biomolecules to acrylamide monomers via amine groups; presumptive chemistry of this process is shown. Hydrogel polymerization is initiated by incubating the perfused tissue at 37°C, resulting in a meshwork of fibers that preserves biomolecules and structural integrity of the tissue. Lipid membranes are removed by passive thermal clearing in SBC solution at 37°C or by electrophoretic tissue clearing (ETC). The resulting intact tissue–hydrogel hybrid can undergo multiple rounds of molecular and structural interrogation using immunohistochemistry and light microscopy. A dedicated computational infrastructure is needed to analyze and store the data. All animal experiments were carried out with Stanford University institutional review board approval.

proteins, nucleic acids, and other small molecules (Fig. 1), but not the vast majority of cellular membrane phospholipids. After the hydrogel polymerization is triggered, lipids (responsible for preventing access of both photons and molecular labels to deep structures) can then be readily removed without destroying or losing native tissue components using strong ionic detergent-based clearing solution (borate-buffered 4% sodium-dodecyl-sulfate) at 37°C, either passively with gentle recirculation or with active electrophoretic forcing (the latter greatly accelerates clearing but introduces some experimental complexity and risk). The resulting lipid-extracted and structurally stable tissue–hydrogel hybrid is immersed in a refractive index (RI) homogenization solution (e.g., 87% glycerol or FocusClear; RI ~1.454) to render the intact brain transparent to light. By allowing multiple rounds of histochemical labeling and elution in the same tissue, CLARITY provides unusually rich access to molecular and structural information.

Imaging Large Clarified Tissue Volumes

The next major challenge after achieving access to clarified large tissues is to develop optimized and high-resolution deep-imaging approaches. One of the most important components of any light microscopy system is the detection objective (Fig. 2*a*), which sets the resolution that can be achieved and the maximum sample size that can be imaged. We have accordingly advised objective manufacturers to facilitate development for CLARITY samples, and these new objectives are becoming available.

In addition to optimized detection optics, the nature of the microscopy system is important for achieving high imaging speed and minimizing photo-bleaching. While confocal and two-photon microscopes have been the workhorse systems in volumetric imaging for the reasons described above, over the past 20 years, light-sheet fluorescence microscopy has emerged as a powerful approach for high-speed volumetric imaging. Figure 2*b* compares the mechanistic foundations of these three imaging modalities. Confocal and two-photon are point-scanning techniques, detecting optical signals point by point to construct an image. Light-sheet microscopy, in contrast, builds on a hundred-year-old idea to illuminate the sample from the side with a thin sheet of light, and detect the emitted fluorescence signal with an in-focus, orthogonally arranged objective (Siedentopf and Zsigmondy, 1903; Huisken and Stainier, 2009). The optical sectioning

is achieved by confining illumination to a selective plane, which enables the use of fast charge-coupled device (CCD) or scientific complementary metal-oxide semiconductor (sCMOS) cameras to capture the whole image simultaneously, and results in an increase of 2–3 orders of magnitude in imaging speed compared with confocal and two-photon microscopy. Moreover, light-sheet microscopy minimizes photo-bleaching (Fig. 2*b*) by confining illumination to the plane of interest. Taken together, these properties of light-sheet microscopy may be well suited for imaging large clarified samples.

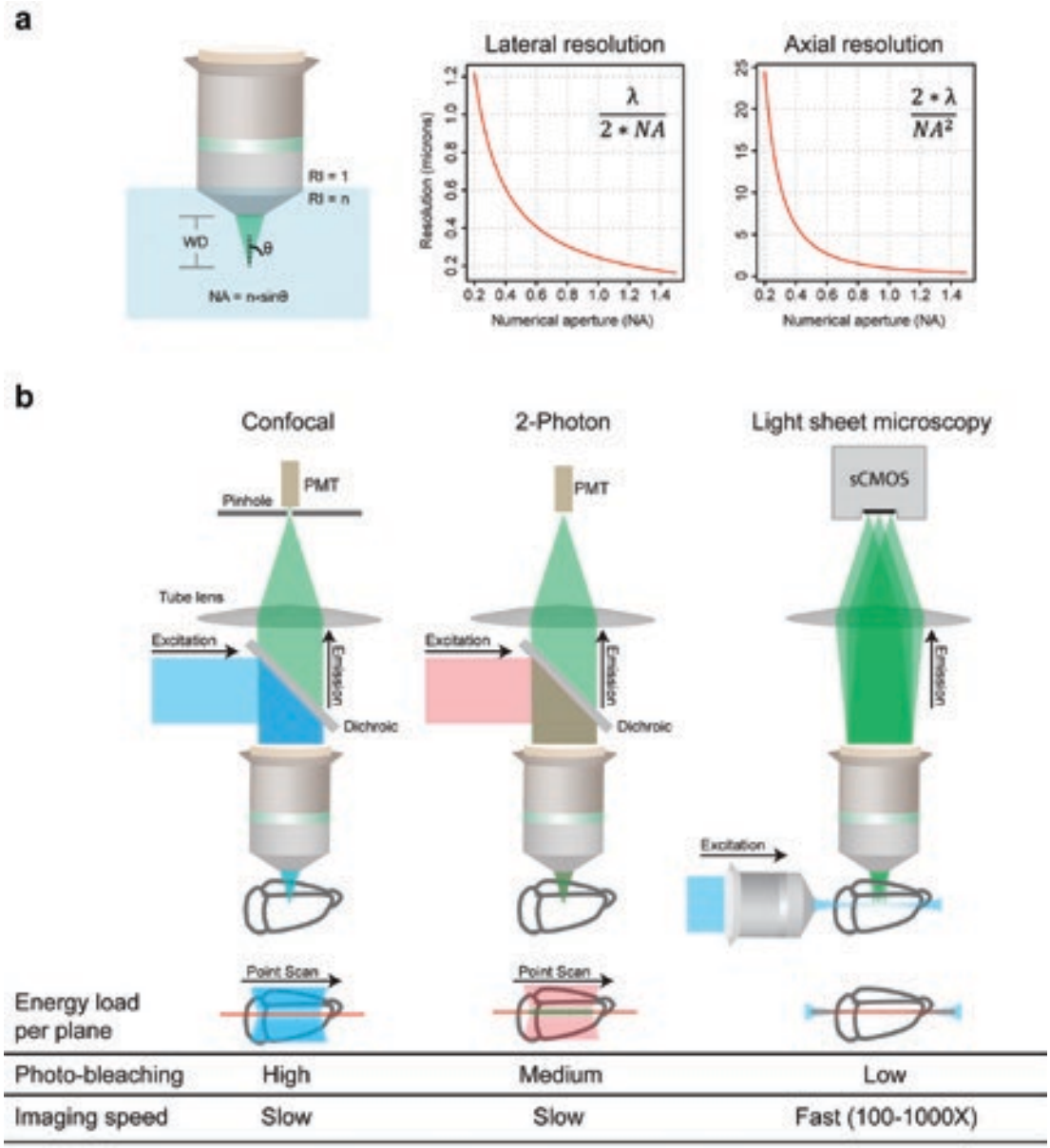

Figure 2. Imaging clarified samples. ***a,*** Key microscope objective parameters relevant to CLARITY are WD, NA, RI (n), and multicolor correction. WD is the distance between the objective lens and the focal plane. NA relates to the fraction of total emitted signal collected by an objective, and higher NA enables higher resolution. The graphs plot diffraction-limited lateral and axial resolution parameters as a function of NA, assuming λ = 500 nm. ***b***, Comparison of confocal, two-photon, and light-sheet microscopy. Confocal microscopy achieves optical sectioning by employing a pinhole in front of the photomultiplier tubes (PMTs). Two-photon microscopy utilizes the fact that only simultaneous absorption of two photons (of longer wavelengths) results in fluorescence signal emission, an event more likely to occur at the point of highest light intensity in the sample, i.e., the focal plane. Light-sheet fluorescence microscopy achieves optical sectioning by selectively confining the illumination to the plane of interest. Confocal and two-photon microscopy use point scanning and hence are inherently slow, whereas light-sheet microscopy uses fast sCMOS/CCD cameras to image the selectively illuminated focal plane, resulting in 2–3 orders of magnitude faster imaging speed and minimal photo-bleaching.

NOTES

CLARITY-optimized light-sheet microscopy

A light-sheet microscope consists of a standard wide-field detection optical arm, which includes the detection objective, the tube lens, and a camera, and the orthogonally arranged, independent illumination arm consisting of a low–numerical aperture (NA) objective, tube lens, and either a cylindrical lens to generate a static light sheet or galvanometer-scanners/*f*-theta lens for creating dynamic light sheets with a Gaussian or Bessel beams (Weber and Huisken, 2011). Conventional light-sheet microscopy suffers from image quality degradation due to out-of-focus scattered light. Thus, several methods have been developed to help reject out-of-focus light in light-sheet microscopy (at some cost in imaging speed, increased photo-bleaching, and instrumentation complexity), such as structured illumination.

We developed CLARITY-optimized light-sheet microscopy (COLM) to maximize the compatibility of clarified samples with light-sheet microscopy, using CLARITY objectives (25× and 10×, Olympus), a fast sCMOS camera, two-axis galvonometer scanners along with the *f*-theta lens, a low-NA objective to generate dynamic light sheets using a Gaussian beam, an optically homogeneous sample manipulation system (see below, Sample mounting apparatus for COLM), and an *xyz*-theta sample mount stage that provides a long travel range of 45 mm in each dimension to enable imaging of large samples (Fig. 3). COLM employs synchronized illumination detection to improve imaging quality, especially at higher depths (Fig. 3*c*), exploiting the unidirectional (as opposed to standard bidirectional) readout mode available in next-generation sCMOS cameras. The scanning beam (which creates the dynamic light sheet) is synchronized with the unidirectional single-line readout of the emitted signal, resulting in a virtual slit arrangement that rejects out-of-focal-plane signal caused by scattering deeper in the sample. Automated-alignment parameter calibration (using linear adaptation) in COLM corrects for misalignment artifacts across the whole sample space (Fig. 3*d*).

Sample mounting apparatus for COLM

The final component of COLM is a CLARITY-optimized sample mounting strategy that minimizes optical inhomogeneity along the detection path (Fig. 3*b*). Clarified whole mouse brain (or any large clarified intact tissue, such as a spinal cord) is mounted in a cuvette made of fused quartz glass (standard cuvettes used for spectrophotometer measurements) filled with FocusClear; note that the RI of fused quartz (~1.458) is nearly identical to that of FocusClear. Using a bottom adapter (Fig. 3*b*), the sample cuvette is mounted onto the *xyz*-theta stage, inside the sample chamber (Fig. 3*b*). The much larger chamber is then filled with a relatively economically priced custom RI matching liquid (RI 1.454), resulting in an optically homogeneous sample manipulation system.

Figure 3*b* compares the images taken using standard light-sheet microscopy or COLM. We performed imaging of whole-brain samples using 10× or 25× magnification objectives (Figs. 4, 5).

Discussion

CLARITY allows molecular and structural interrogation of tissue by allowing deep imaging of transgenic and/or biochemically labeled tissue samples. To achieve the best imaging quality, careful preparation of the sample and optical setup is crucial. First, as demonstrated in Figure 2, key relevant properties of the objective must be considered, including NA, working distance (WD), color correction, and RI correction. We explored the emerging commercially available and custom solutions, and found that it is indeed possible to achieve deep high-resolution and overall high-quality imaging in clarified samples (Figs. 4, 5). Other water immersion, oil immersion, or air objectives may also prove useful for quality imaging deep in tissue.

The major limitations of confocal and two-photon microscopes are as follows: (1) slow speed owing to point scanning mechanisms (Fig. 2) and (2) damage to tissues and fluorophores caused by redundant illumination of the whole sample for every optical plane imaged, limiting the sample size that can be imaged in a reasonable timeframe before the sample is completely photo-bleached (particularly in the case of confocal microscopy). Light-sheet microscopy now emerges as an alternative for fast 3D imaging of large clarified samples, as described above.

We assessed the compatibility of clarified samples with light-sheet microscopy, observing 2–3 orders of magnitude faster imaging speed with minimal photo-bleaching. For example, it was possible to image an entire mouse brain in ~4 h using a 10× magnification objective and in ~1.5 d using a 25× objective, as opposed to many days and months, respectively, with a confocal microscope. COLM is especially well suited for interrogation of large tissue samples labeled with transgenic or histochemical techniques. The increased speed of acquisition and higher quality of data generated via CLARITY using new microscopy methods, combined with high-speed CLARITY processing itself enabled by parallelized and efficient

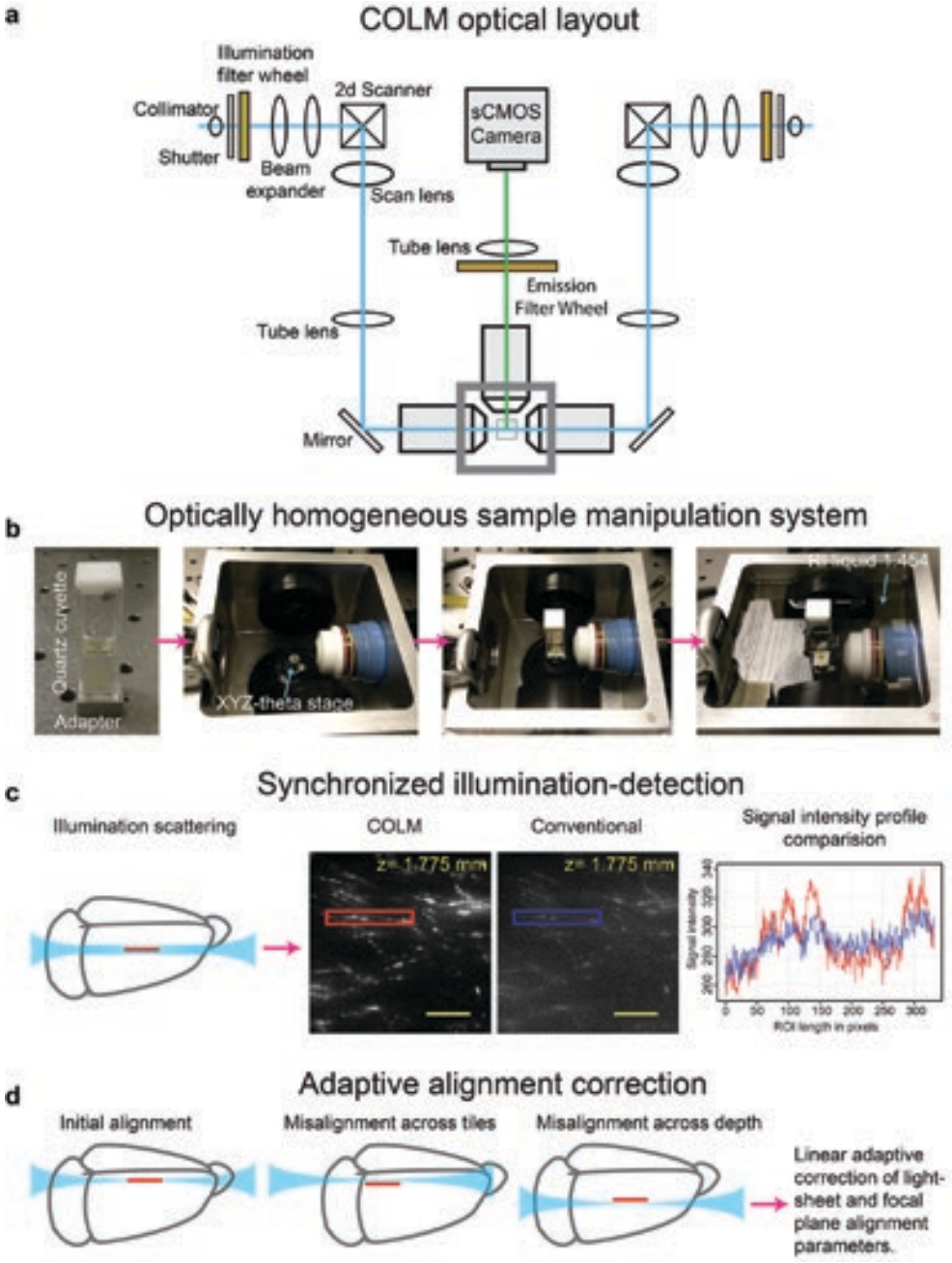

Figure 3. COLM for large intact samples. ***a,*** Optical layout of the COLM microscope. Two light sheets are created from opposite sides; shown are galvanometer scanners, scan lens, tube lens, and illumination objectives. The emitted fluorescence is imaged with an in-focus detection objective, tube lens, and sCMOS camera. Illumination and emission filter wheels (motorized) are used to generate well-defined excitation light and emission signal bands, respectively. The innovations required for COLM are discussed in ***b–d***, and the schematic is shown in Supplemental Figure 2 (http://clarityresourcecenter.com/COLM.html). ***b,*** Optically homogeneous sample mounting framework for large intact samples. Clarified samples, such as intact adult mouse brain, are mounted in a quartz cuvette filled with RI matching solution such as FocusClear. Note that the RI of quartz glass (~1.458) is nearly identical to that of FocusClear (~1.454). A bottom adapter is used to attach the cuvette to the *xyz*-theta stage in the sample chamber, which is then filled with a matching RI liquid (~1.454). This results in an optically homogenous sample manipulation system with minimal RI transition boundaries. ***c,*** Synchronized illumination and detection are achieved by synchronizing the scanning beam with the unidirectional readout of a sCMOS camera chip, resulting in a virtual-slit effect that enables substantially improved imaging quality, as illustrated by the images shown acquired from the same plane with COLM and with conventional light-sheet microscopy. The graph at right compares the signal intensity profile of a field acquired with COLM (red) with one acquired by conventional light-sheet microscopy (blue). ***d,*** Large clarified samples can have significant RI inhomogeneity, resulting in the need for correction of misalignment of illumination with the focal plane of the detection objective. We achieved this with a linear adaptive calibration procedure before starting the imaging experiment. Scale bars, ***a–d,*** 100 μm.

NOTES

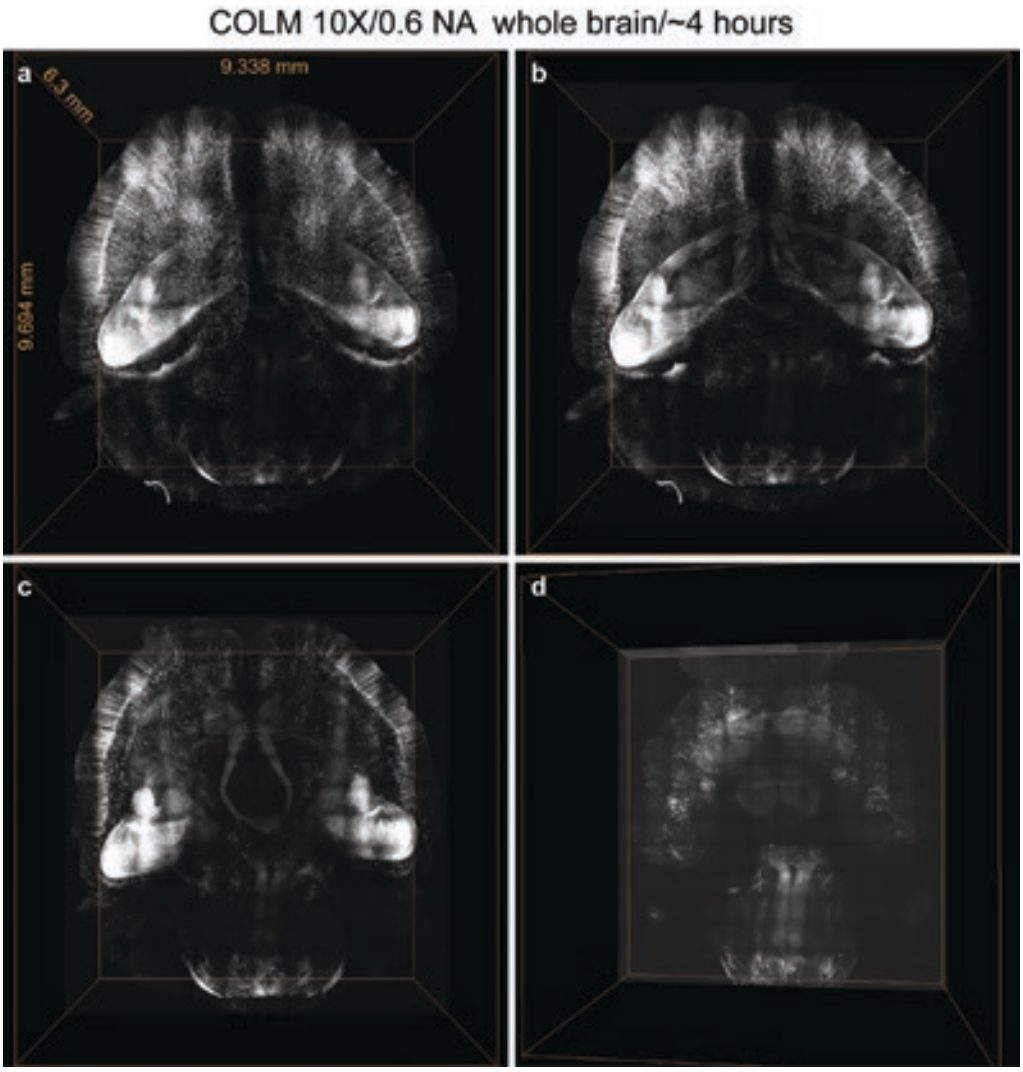

Figure 4. Ultrafast imaging of whole mouse brain using COLM. ***a,*** Volume rendering of whole mouse brain dataset acquired from an intact clarified *Thy1*-EYFP mouse brain using COLM. ***b, c, and d*** illustrate internal details of the intact mouse brain volume visualized by successive removal of occluding dorsal-side images. The brain was perfused with 0.5% (wt/vol) acrylamide monomer solution and clarified passively at 37°C with gentle shaking. Camera exposure time of 20 ms was used, and the RI liquid 1.454 was used as immersion media. The entire dataset was acquired in ~4 h using a 10×, 0.6 NA objective.

tissue transformation protocols described here, together define a versatile and efficient platform for structural and molecular interrogation of large and fully assembled tissues.

Acknowledgments

We thank the entire Deisseroth Lab for helpful discussions, Anna Lei for technical assistance, and Li Ye and Brian Hseuh for help with sample preparations. All CLARITY tools and methods described are distributed and supported freely (clarityresourcecenter.org, http://wiki.claritytechniques.org) and discussed in an open forum (forum.claritytechniques.org).

This chapter is excerpted from a previously published article in Nature Protocols 2014;9(7):1682–1697. All materials from the original article, including figures and videos, along with supplementary materials, are available in high resolution at http://clarityresourcecenter.com/COLM.html.

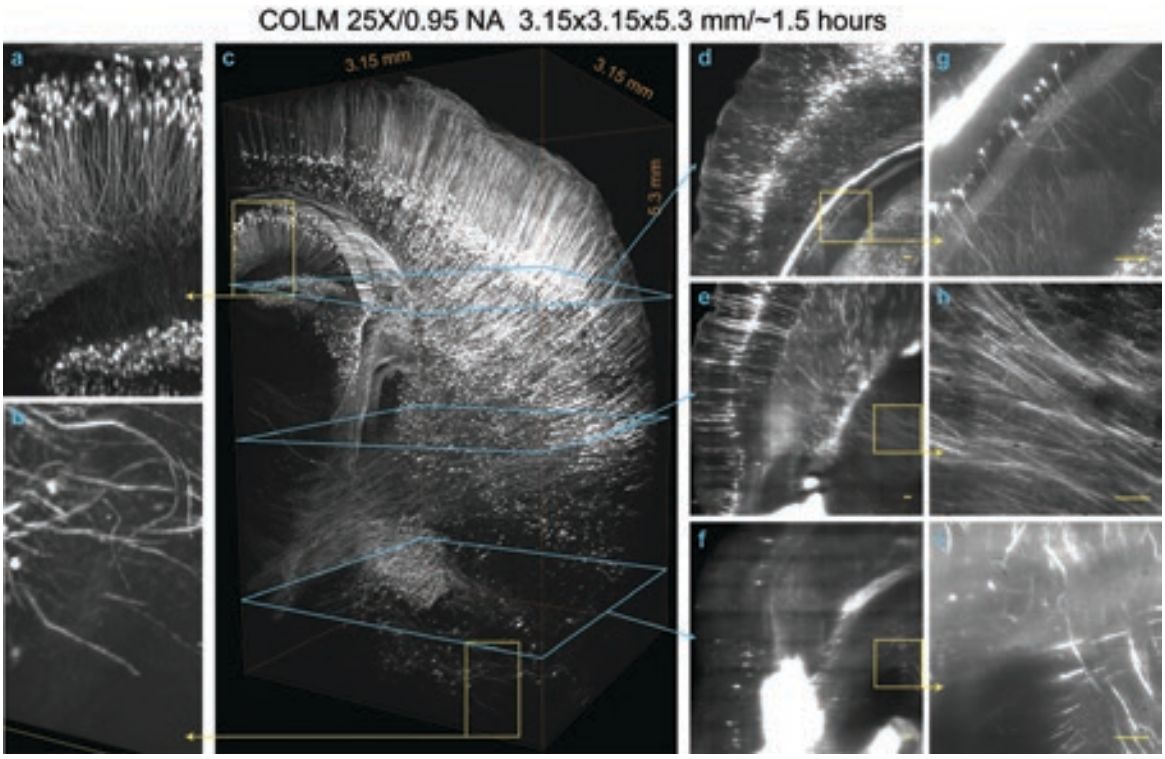

Figure 5. Fast high-resolution imaging of clarified brain using COLM. 3.15 × 3.15 × 5.3 mm volume acquired from an intact clarified *Thy1*-EYFP mouse brain using COLM with 25× magnification; the brain had been perfused with 0.5% (wt/vol) acrylamide monomer solution. The complete image dataset was acquired in ~1.5 h; for optimal contrast, the lookup table (LUT) of zoomed-in images was linearly adjusted between panels. ***a*** *and* ***b*** show magnified views from panel ***c*** regions defined by yellow squares. ***d–i*** show maximum-intensity projections over a 50 µm thick volume, as shown by the progression of cyan and yellow boxes and arrows. Camera exposure time of 20 ms was used; RI liquid 1.454 was used as the immersion medium. Scale bars, ***a–d,*** 100 µm.

References

Bock DD, Lee WC, Kerlin AM, Andermann ML, Hood G, Wetzel AW, Yurgenson S, Soucy ER, Kim HS, Reid RC (2011) Network anatomy and *in vivo* physiology of visual cortical neurons. Nature 471:177–182.

Briggman KL, Helmstaedter M, Denk W (2011) Wiring specificity in the direction-selectivity circuit of the retina. Nature 471:183–188.

Chung K, Wallace J, Kim SY, Kalyanasundaram S, Andalman AS, Davidson TJ, Mirzabekov JJ, Zalocusky KA, Mattis J, Denisin AK, Pak S, Bernstein H, Ramakrishnan C, Grosenick L, Gradinaru V, Deisseroth K (2013) Structural and molecular interrogation of intact biological systems. Nature 497:332–337.

Conchello JA, Lichtman JW (2005) Optical sectioning microscopy. Nat Methods 2:920–931.

Dodt HU, Leischner U, Schierloh A, Jahrling N, Mauch CP, Deininger K, Deussing JM, Eder M, Zieglgansberger W, Becker K (2007) Ultramicroscopy: three-dimensional visualization of neuronal networks in the whole mouse brain. Nat Methods 4:331–336.

Hama H, Kurokawa H, Kawano H, Ando R, Shimogori T, Noda H, Fukami K, Sakaue-Sawano A, Miyawaki A (2011) Scale: a chemical approach for fluorescence imaging and reconstruction of transparent mouse brain. Nat Neurosci 14:1481–1488.

Helmchen F, Denk W (2005) Deep tissue two-photon microscopy. Nat Methods 2:932–940.

Huisken J, Stainier DY (2009) Selective plane illumination microscopy techniques in developmental biology. Development 136:1963–1975.

Ke MT, Fujimoto S, Imai T (2013) SeeDB: a simple and morphology-preserving optical clearing agent for neuronal circuit reconstruction. Nat Neurosci 16:1154–1161.

NOTES

Kim JS, Greene MJ, Zlateski A, Lee K, Richardson M, Turaga SC, Purcaro M, Balkam M, Robinson A, Behabadi BF, Campos M, Denk W, Seung HS, EyeWirers (2014) Space–time wiring specificity supports direction selectivity in the retina. Nature 509:331–336.

Kim SY, Chung K, Deisseroth K (2013) Light microscopy mapping of connections in the intact brain. Trends Cogn Sci 17:596–599.

Ramón Y Cajal S (1904) Textura del sistema nervioso del hombre y de los vertebrados. Vol 2. Nicholas Moya.

Siedentopf H, Zsigmondy R (1903) Uber Sichtbarmachung und Grössenbestimmung ultramikroskopischer Teilchen, mit besonderer Anwendung auf Goldrubingläser. Annalen der Physik 10:1–39.

Tang J, Germain RN, Cui M (2012) Superpenetration optical microscopy by iterative multiphoton adaptive compensation technique. Proc Natl Acad Sci USA 109:8434–8439.

Tomer R, Ye L, Hsueh B, Deisseroth K (2014) Advanced CLARITY for rapid and high-resolution imaging of intact tissues. Nat Protocols 9:1682–1697.

Weber M, Huisken J (2011) Light sheet microscopy for real-time developmental biology. Curr Opin Gen Dev 21:566–572.

Computational Techniques for Constructing Brain Atlases

Lydia Ng, PhD

Allen Institute for Brain Science
Seattle, Washington

Introduction

The Allen Mouse Brain Connectivity Atlas is a comprehensive database of high-resolution images of axonal projections targeting different anatomical regions or various cell types using Cre-dependent specimens (Oh et al., 2014). Each specimen was injected with an enhanced green fluorescent protein (EGFP)–expressing adeno-associated anterograde viral tracer. EGFP-labeled axonal projections were systematically imaged using the TissueCyte 1000 serial two-photon (STP) tomography system (TissueVision, Cambridge, MA), which couples high-speed two-photon microscopy with automated vibratome sectioning (Ragan et al., 2012). By imaging the block-face, STP tomography essentially eliminates tissue distortions that occur in conventional section-based histological methods, yielding a series of highly conformed, inherently prealigned images amenable to precise three-dimensional (3D) spatial mapping (Fig. 1).

For each brain, 140 coronal plane high-resolution (0.35 μm) images were obtained at a *z*-sampling interval of 100 μm to span the entire brain during a continuous 18.5 h scanning period, resulting in an approximately 750 gigabyte dataset per brain. Background fluorescence in the red channel illustrated basic anatomy and brain structures. The injection site and axonal projection information were collected in the green channel. Each image series was processed through an informatics data pipeline (IDP) to obtain spatially mapped, quantified projection information. Key algorithms were developed to reliably extract labeled axons from the digitized images and to bring data from different sections and animals into registration to allow computational comparison (Fig. 2). Output of the pipeline supported the creation of whole-brain connectivity matrices and analysis of connectional strength distribution, symmetry, and other network properties (Oh et al., 2014). On the Web application (http://connectivity.brain-map.org), informatics results support key features, such as an interactive projection summary graph for each specimen, an image synchronization feature to browse images from multiple injections and reference data and atlases in a coordinated manner, and an on-the-fly search service to identify specimens with specific projection profiles.

Annotated 3D Reference Space

The backbone of the automated informatics pipeline is an annotated 3D reference space based on the same brain specimen used for the coronal Allen Reference Atlas (Dong, 2008). The reference brain was sectioned to span a nearly complete specimen resulting in 528 Nissl-stained sections, each 25 μm thick. A brain volume was reconstructed from the images using a combination of high-frequency section-to-section histology registration with low-frequency histology to (*ex cranio*) MRI registration (Yushkevich et al., 2006). This first-stage reconstruction was then aligned with a reconstructed sagittally sectioned specimen. Once a straight midsagittal plane was achieved, a synthetic symmetric space was created by reflecting one hemisphere to the other side of the volume. More than 800 structures were extracted from the 2D coronal reference plates (132 plates, 100 μm apart) and interpolated to create symmetric 3D annotations.

Image Registration

The two-photon tomography imaging platform generated images that are inherently prealigned, allowing the stacking of images together to form a coherent 3D reconstructed volume. This stacking

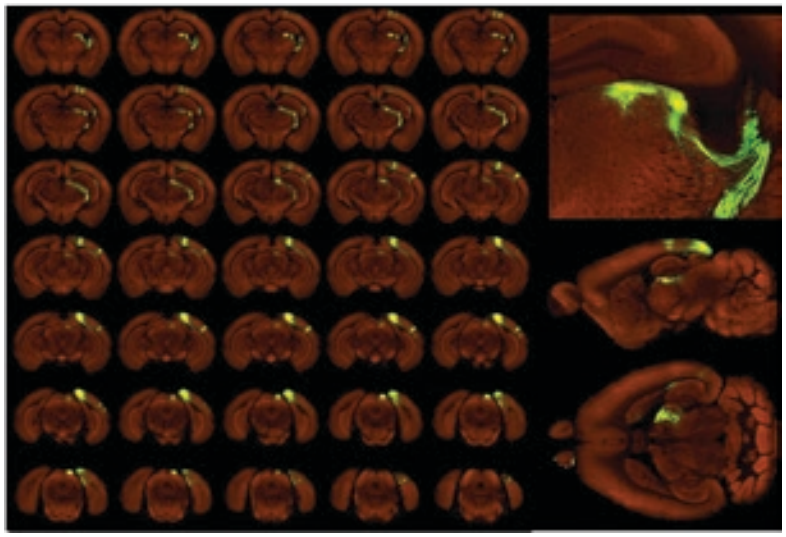

Figure 1. High-resolution images of a single specimen from the Allen Mouse Brain Connectivity Atlas shown as an example (injection into the primary visual area). The injection site and major targets can easily be seen. Block-face imaging generates inherently prealigned images amenable to precise 3D mapping.

NOTES

eliminates the 3D reconstruction step typically required if images were generated with conventional section-based histology.

Mapping a 3D specimen brain directly to the Nissl-based reference space is a multimodality registration problem because the intensity profile of background fluorescence does not have a straightforward relationship with the intensity profile of the Nissl volume. It is difficult to make multimodality registration methods robust through thousands of specimens because processing each specimen requires a large parameter optimization to "learn" both deformation as well as complex intensity relationships.

One strategy to reduce complexity is to introduce an intermediary registration template with the same intensity profile as the specimen brains. A simple option could be to select a single specimen as a template; however, careful selection is needed because any damage or abnormality will introduce biases as each brain is forced to match the abnormalities of the selected specimen. Instead, we created an unbiased template by averaging over many specimen brains (similar to Fonov et al., 2011; Ullmann et al., 2013). The creation of an averaged template and registration of specimen brains to the template are two iterative, intertwined processes.

The iterative process was bootstrapped by globally aligning the initial set of 41 specimen brains generated at the time to the Nissl-based reference space (Fig. 3*a*). A global alignment process consisted of three steps: first, a coarse registration was initialized by matching the image moments of the specimen brain and the target. The second step was a rigid (rotation and translation) registration, and the third step consisted of a 12-parameter affine (linear) registration. Each step was based on maximizing normalized mutual information between the specimen and target intensity. A multiresolution scheme was used where the optimization was first solved on smoothed and downsampled versions of the image stack. Smoothing out the details reduced complexity, driving the algorithm to match on large-scale shape features. The results from one resolution was then used to initialize the optimization at the next resolution, allowing finer details to be matched. After global alignment, the 41 specimens were averaged to create the first iteration of the template. All specimen brains were then globally aligned to the template, and then averaged to create the next iteration of the template (Fig. 3*b*).

A local alignment stage was then introduced to increase alignment accuracy by modeling local deformations. Similar to the global alignment stage, B-spline-based deformable registration was also conducted sequentially, from coarse to fine, in four resolution levels. In this method, deformation between specimen and template was parameterized as 3D B-splines where the knots are placed on a regularly spaced 3D grid. A coarse grid implicitly allows only smooth or stiff deformations, whereas a finer grid allows more elastic transformations. Deformable registration can easily become trapped in a local minimum, especially when there is specimen damage, and hence a coarse-to-fine approach is essential. The initial coarse-level alignments allow large-scale anatomy to be matched, which is used to initialize finer levels of alignment, allowing local neighborhoods to be more accurately matched.

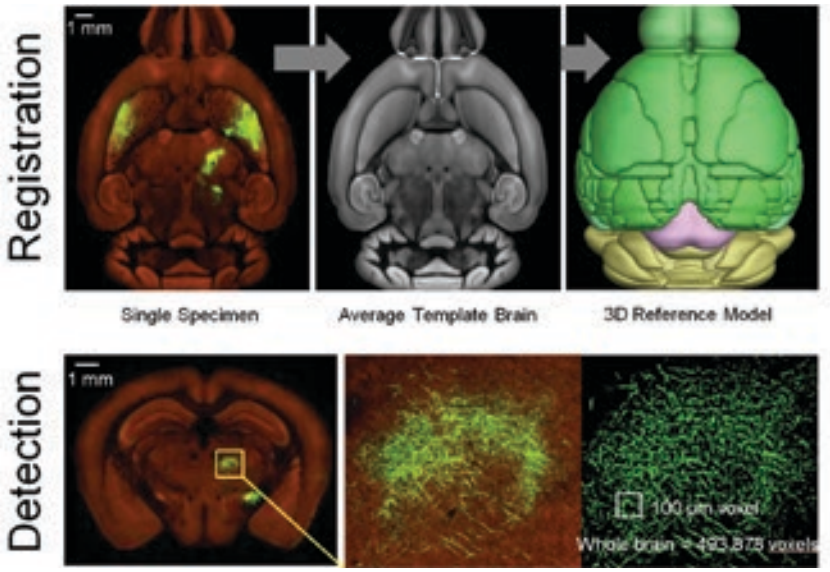

Figure 2. Key algorithms were developed to extract labeled axons from the digitized images (detection) and to bring all data into the common coordinates of a 3D reference space. Scale bars, 1 mm.

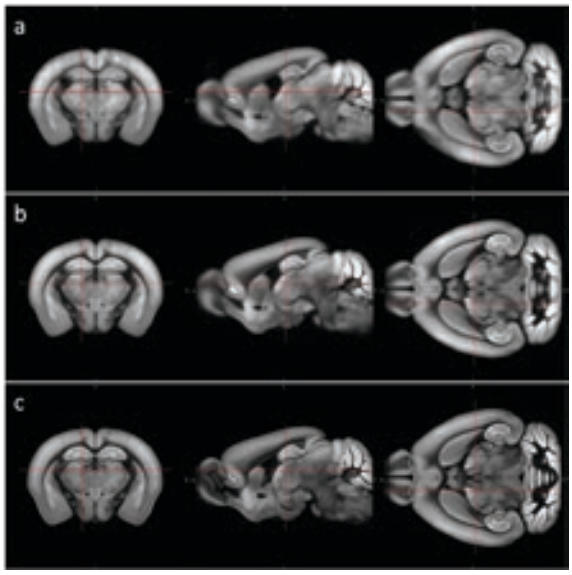

Figure 3. Evolution of the averaged registration template. *a,* Average of 41 brains globally aligned to the Nissl-based 3D reference space. *b,* Average of ~700 globally aligned brains. *c,* Average of ~1200 locally aligned brains after four iterations of average template generation.

All specimen brains were locally aligned to the template, then averaged to create the next iteration of the template. This process continues for multiple rounds until the algorithm converges and the template change is below threshold. The final average template (averaged from 1231 brains) shows remarkably clear anatomical features and boundaries (Fig. 3c). The last step consisted of deformable registration of the average template with the original annotated reference space by maximizing mutual information of large-structure annotation and template intensity.

Because meaningful information data quantification is highly dependent on mapping precision, registration variability was investigated in two ways (Oh et al., 2014). First, three independent raters selected and identified 10 widely distributed 3D anatomical fiducial points in the Nissl reference space, registration template, and 30 experimental brains. They found a high degree of concordance among individual brains, with median variation <49 μm in each dimension between each brain and the average template brain, which is comparable with the median interrater variation of <39 μm. The median difference was <71 μm between each brain and the annotated reference space. Second, manual and informatics annotation of the injection sites was compared for approximately 500 specimens. Informatics-derived assignment of injection-site structures had >75% voxel-level concordance with manual expert annotation for almost all injection sites. These analyses confirmed the relatively high fidelity in the registration method, in which a large contribution of error was derived from imperfect alignment between the average template brain and the Nissl reference space.

Signal Detection

The signal detection algorithm was applied to each image to segment positive fluorescent signal from background. Owing to scanner, biological, and specimen variations, image intensity was first rescaled by square-root transform to remove second-order effects, followed by histogram matching at the midpoint to a template profile. Fitting all specimens to a standard profile enabled uniform selection of thresholds and other parameters. Median filtering and a large-kernel low-pass filter were then applied to remove noise.

Signal detection on the processed images was based on combining adaptive edge/line detection with morphological processing. Edge detection kernels of different sizes and orientations were used to identify edge-like features in the image. Next, high-threshold "strong" edges and low-threshold "weak" edges were joined if they were spatially close to form candidate signal object sets. Candidate objects were then filtered based on their morphological attributes, such as length and area, using connected component labeling. Separately, clumped signals (e.g., near the injection site or at strong target locations) were detected using adaptive thresholding. In a postsegmentation step, objects detected near hyperintense artifacts occurring in multiple channels were removed. It should be noted that passing fibers and terminals were not distinguished by these methods. The resulting output was a full-resolution "segmentation mask" that classified each 0.35 μm pixel as either signal or background.

Data Voxelization

An isotropic 3D summary of each specimen brain was constructed by dividing each image into a 100 × 100 μm grid. Total signal was computed for each division or voxel by summing the number of signal-positive pixels in that voxel. The deformation field computed by the registration algorithm was then used to resample the voxelized data within the common coordinates of the 3D reference space. Total signal for each structure was obtained by combining voxels from the same structure in the 3D reference model (Fig. 4).

Computational Paths

The ability to reconstruct projection trajectories would be particularly useful for investigating the relationship between projection fields and pathways, understanding

NOTES

the impact of white-matter lesions, or helping to explain brain model dynamics. In this experiment, for each specimen, computational paths were created by using the fast marching algorithm (Sethian, 1999) to generate a time-of-arrival map. This map represents the arrival of a front propagating out from the injection site. The speed of the front is defined by projection density (proportion of signal-positive pixels in a voxel). The higher the density, the lower the viscosity and the faster moving the front; the lower the density, the higher the viscosity and the slower moving the front. Fast marching methods also result in a vector at each voxel pointing back toward the injection site. Computational paths are then generated by tracing back through this vector field. Generally speaking, computational paths represent the minimum cost paths through the highest projection-density areas.

Search Services

An on-the-fly search service within the Allen Mouse Brain Connectivity Atlas allows users to instantly search the whole dataset to find experiments with specific projection profiles:

- The **Source Search** function retrieves specimens by anatomical location of the injection site.
- The **Target Search** function returns a ranked list of specimens by signal volume in the user-specified target structure(s).
- The **Spatial Search** function returns a ranked list of specimens by density of signal in the user-specified target voxel location.
- The **Injection Coordinate Search** function returns a ranked list of specimens by distance from their injection site to a user-specified seed location.
- The **Correlation Search** function enables the user to find specimens that have a similar spatial projection profile to a seed specimen when compared over a user-specified domain.

In order to perform these computations quickly over the entire dataset, all 489,393 nonbackground voxels

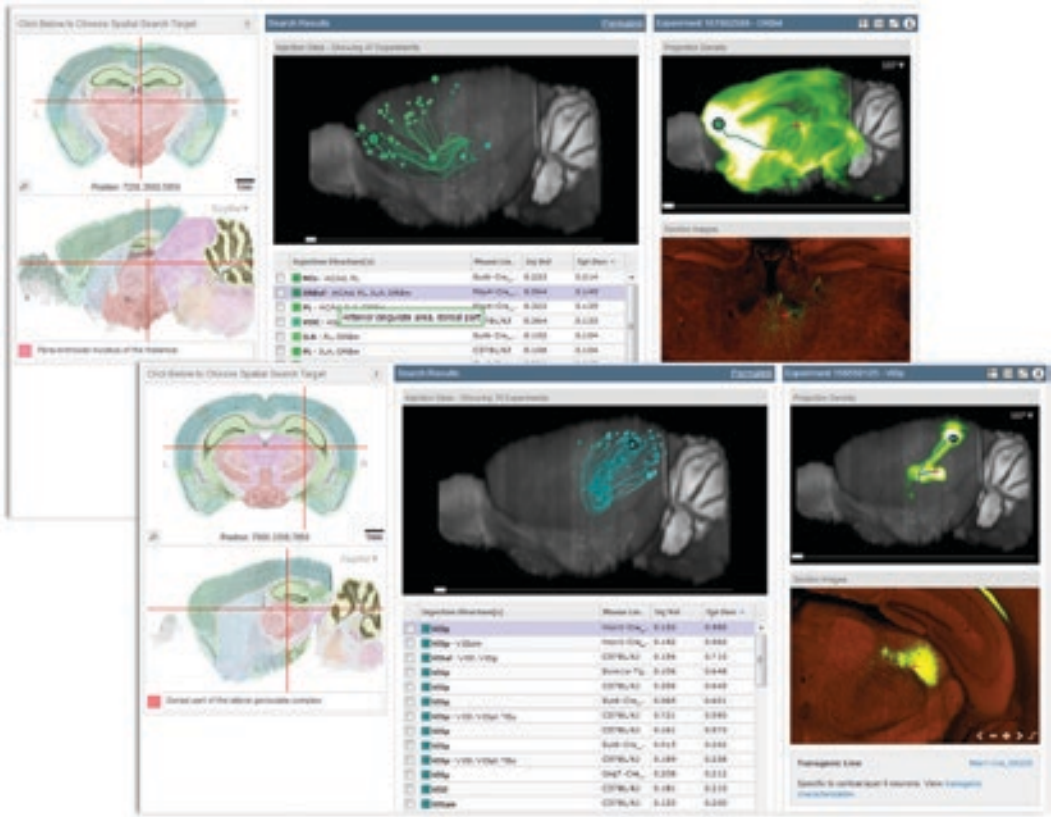

Figure 4. The voxelized data search services enable the creation of on-the-fly "virtual retrograde projection" maps at any spatial location in the brain by finding injections that project to the targeted position. Two examples are shown with different seeds in the thalamus. A tightly integrated browser enables interactive exploration of topology while conferring instant access to the primary image data.

from every experiment have been loaded into the server memory as a matrix. Each user search request is computed on demand.

Discussion

Connectivity defines function, so the lack of full comprehensive knowledge of connectivity impedes the understanding of the brain (Van Essen, 2013). Availability of a comprehensive map would help with experimental design in electrophysiology, provide constraints on neural network models, and advance comparative and evolutionary studies, among other benefits. The Allen Mouse Brain Connectivity Atlas is a mesoscale connectome that can begin to fill in some of these knowledge gaps.

The Allen Mouse Brain Connectivity Atlas has all the desired features summarized in a mesoscale connectome position essay by Bohland et al. (2009): brainwide coverage, validated and versatile experimental techniques, a single standardized data format, a quantifiable and integrated neuroinformatics resource, and an open-access public online database.

Moreover, systematically generating data and methodically mapping the data to the common coordinates of reference space allow connectomics to go beyond mere 2D structure-to-structure analysis using predefined anatomical parcellations. Spatially mapped data allow projection topography to be explored. Projection data, like gene expression, can then be used to define spatial relationships and neuroanatomical organizations.

References

Bohland JW, Wu C, Barbas H, Bokil H, Bota M, Breiter HC, Cline HT, Doyle JC, Freed PJ, Greenspan RJ, Haber SN, Hawrylycz M, Herrera DG, Hilgetag CC, Huang ZJ, Jones A, Jones EG, Karten HJ, Kleinfeld D, Kötter R, et al. (2009). A proposal for a coordinated effort for the determination of brainwide neuroanatomical connectivity in model organisms at a mesoscopic scale. PLoS Comput Biol 5:e1000334.

Dong HW (2008) The Allen reference atlas: a digital color brain atlas of the C57BL/6J male mouse. Hoboken, NJ: Wiley.

Fonov V, Evans AC, Botteron K, Almli CR, McKinstry RC, Collins DL (2011) Unbiased average age-appropriate atlases for pediatric studies. Neuroimage 54:313–327.

Oh SW, Harris JA, Ng L, Winslow B, Cain N, Mihalas S, Wang Q, Lau C, Kuan L, Henry AM, Mortrud MT, Ouellette B, Nguyen TN, Sorensen SA, Slaughterbeck CR, Wakeman W, Li Y, Feng D, Ho A, Nicholas E, et al. (2014) A mesoscale connectome of the mouse brain. Nature 508:207–214.

Ragan T, Kadiri LR, Venkataraju KU, Bahlmann K, Sutin J, Taranda J, Arganda-Carreras I, Kim Y, Seung HS, Osten P (2012) Serial two-photon tomography for automated *ex vivo* mouse brain imaging. Nat Methods 9:255–258.

Sethian JA (1999) Level set methods and fast marching methods: evolving interfaces in computational geometry, fluid mechanics. Cambridge, UK: Cambridge University Press.

Ullmann JF, Watson C, Janke AL (2013). A segmentation protocol and MRI atlas of the C57BL/6J mouse neocortex. Neuroimage 78:196–203.

Van Essen DC (2013) Cartography and connectomes. Neuron 80:775–790.

Yushkevich P, Avants B, Ng L, Hawrylycz M, Burstein P, Zhang H, Gee J (2006) 3-D mouse brain reconstruction from histology using a coarse-to-fine approach. In: Third International Workshop on Biomedical Image Registration (WBIR), July 9–11, 2006, Utrecht, Netherlands. Proceedings (Pluim JPW, Likar B, Gerritsen FA, eds.), pp. 230–237.

The Isotropic Fractionator: A Fast, Reliable Method to Determine Numbers of Cells in the Brain

Suzana Herculano-Houzel, PhD

Institute of Biomedical Sciences
Federal University of Rio de Janeiro, Brazil

Institute of Translational Neuroscience
Ministry of Science and Technology
Sao Paulo, Brazil

Introduction

Stereological techniques that estimate cell numbers require specific training and elaborate sampling strategies to infer total numbers of cells in well-defined structures of measurable volume. The isotropic fractionator is a fast and inexpensive method that requires little specific training and few materials before it can be used to quantify total numbers of neuronal and nonneuronal cells in the whole brain or any dissectable regions thereof. It transforms highly anisotropic (paraformaldehyde-fixed and dissected) brain structures into homogeneous, isotropic suspensions of cell nuclei, which can be counted and identified morphologically and immunocytochemically as neuronal or nonneuronal. Estimates of total cell, neuronal, and nonneuronal numbers can be obtained within 24 h and vary by less than 10% among samples of the same structure. And, because the estimates obtained are independent of brain volume, they can be used in comparative studies of brain volume variation among species and in studies of phylogenesis, development, adult neurogenesis, and pathology.

Traditionally, stereological methods such as the optical disector and fractionator have been the gold standard for estimating numbers of cells in discrete brain regions and determining how they compare across structures, species, ages, conditions, or experimental manipulations (West, 1999). These methods, however, are very time-consuming. They require familiarity with stereological techniques, depend on accurate measurement of structure volume, and either must be restricted to well-defined structures of isotropic architecture and measurable volume, or require elaborate sampling strategies to ensure that the counted samples are representative.

To circumvent these drawbacks, we created an alternative method: the isotropic fractionator (Herculano-Houzel and Lent, 2005), which estimates the total number of neuronal and nonneuronal cells independently from tissue volume and anisotropy, and can be applied to the whole brain or any dissectable structure. It does not require familiarity with stereological techniques and yields reproducible estimates of total numbers of cells and neurons within a single day. The isotropic fractionator has recently been compared with stereology by two independent groups and was found to yield similar results in far less time (Bahney and von Bartheld, 2014; Miller et al., 2014). We have already used this method in comparative studies of the cellular composition of the brain of different mammalian species (Herculano-Houzel et al., 2006, 2007, 2011, 2014; Sarko et al., 2009; Gabi et al., 2010; Neves et al., 2014). These include studies of the entire human brain (Azevedo et al., 2009), of the distribution of neurons across functional areas of the mouse cerebral cortex (Herculano-Houzel et al., 2013), across the human cerebral cortex (Ribeiro et al., 2013), and of the changes in the cellular composition of the developing rat brain (Bandeira et al., 2009). Other possible uses of the isotropic fractionator include the analysis of pathological alterations in the cellular composition of the brain and of experimental manipulations expected to affect it.

The isotropic fractionator relies on the single assumption that every cell in the brain contains one and only one nucleus. This method consists of processing fixed brains, either as a whole or dissected into subregions, into an isotropic suspension of isolated nuclei in which cytoarchitectural heterogeneities have been literally dissolved. Because this suspension has a known, defined volume and can be made homogeneous by agitation, the total number of nuclei therein (and, therefore, the total number of cells in the original tissue) can be estimated by determining the density of nuclei in small aliquots of the suspension. Once the total cell number is known, the proportion of neurons is determined by immunocytochemical detection of neuronal nuclear antigen (NeuN), which is expressed in all nuclei of most neuronal cell types (notable exceptions are Purkinje cells, inferior olive neurons, mitral cells, and photoreceptors) but not in nonneuronal cells (Mullen et al., 1992; Gittins and Harrison, 2004). Then, the number of nonneuronal cells can be derived by subtraction. Alternatively, morphological criteria can be used to determine the numbers of readily identifiable nuclear types, such as those of Purkinje cells.

The single most important limitation of the isotropic fractionator is that it relies on nuclear labels to identify specific subpopulations of cell nuclei. This eliminates several useful neuronal and glial cell markers, which are restricted to the cytoplasm, such as MAP2 (microtubule-associated protein-2) and GFAP (glial fibrillary acidic protein). On the other hand, more and more cell-type-specific transcription factors are being discovered, thereby expanding the applications of the method.

Isotropic Fractionator Steps

The isotropic fractionator is a simple, fast, and reliable method for counting cells in brain (and other) tissue that consists of only a few steps.

NOTES

1. Tissue fixation
The tissue to be analyzed is ideally perfusion-fixed, and postfixation by immersion in 4% paraformaldehyde is required. Good fixation is mandatory for the technique to work; two weeks of postfixation suffice to render the cell nuclei extremely resistant to mechanical friction.

2. Tissue dissection
This step limits how reliable individual counts are, so the technique is best applied to easily dissectable structures. Whole brain can also be used, which requires little dissection.

3. Tissue dissociation
The dissected structures are homogenized by mechanical friction in a saline detergent solution, which dissolves the cell membranes while maintaining the nuclear membranes intact, thus turning the tissue into a suspension of free nuclei.

4. Counting total cell numbers
Samples of the diamino-phenyl-indol (DAPI)–stained nuclei suspension (made homogeneous by agitation) are counted in a hemocytometer. Typically, this step takes 15–20 min per structure to be counted.

5. Heat-induced epitope retrieval
This is a necessary step when tissue has been overfixed, that is, when it has been postfixed for more than 2 months.

6. Immunocytochemical identification of specific nuclear types
Neuronal nuclei in most structures can be identified by the expression of the NeuN antigen. Alternatively, morphological criteria can be used. Immunocytochemical processing takes 5–6 h, after which it takes ~30 min to determine the proportion of specific nuclear types in each structure. Alternatively, flow cytometry can be used in this step to speed up the determination of the proportion of immunolabeled nuclei (Collins et al. 2009). However, visual identification of immunolabeled nuclei has several advantages: (1) It ensures quality control over the samples, since stained debris is easily discernible from labeled nuclei under the microscope; (2) it allows the identification of specific cell types by their nuclear morphology; and (3) it is readily accessible to any laboratory equipped with an upright fluorescence microscope.

7. Storage of free nuclei
Since the immunocytochemical identification of specific nuclear types requires only a small aliquot of the nuclear suspension, the remaining volume can be stored in antifreezing solution for later reanalysis, for instance, when other antibodies become available, or for photographical documentation.

Materials
1. Tissue fixation
- Saline (NaCl, 0.9%)
- Paraformaldehyde (4% solution in 0.1M phosphate buffer)
- Peristaltic pump

2. Tissue dissection
- Surgical instruments
- Stereoscopic microscope
- Analytic balance

3. Tissue dissociation
- Tenbroeck tissue grinder (glass homogenizer, 2, 7, or 40 ml capacity, depending on the size of the tissue of interest)
- Dissociation solution: 1 l of 1% Triton X-100 in 40 mM sodium citrate
- Pasteur pipettes
- Centrifuge tubes (15 or 50 ml)
- PBS
- Clinical centrifuge

4. Counting total cell numbers
- DAPI (Molecular Probes, Life Technologies, Grand Island, NY), 10 mg/l
- Neubauer chamber (hemocytometer), improved to allow simultaneous visualization of DAPI-stained nuclei and the counting grid
- Micropipette, 10 µl
- Fluorescence microscope, upright (inverted microscopes will not do)

5. Heat-induced epitope retrieval
- 0.2 M boric acid, pH 9.0 (adjusted with lentils of NaOH)
- PBS
- 1.5 ml Eppendorf tubes (Eppendorf, Hauppauge, NY)
- Microcentrifuge
- Heating bath or oven at 70°C

6. Immunocytochemical identification of specific nuclear types
- Anti-NeuN mouse IgG (MAB377), or Cy3-conjugated polyclonal rabbit anti-NeuN IgG (in which case a secondary antibody will not be necessary; EMD Millipore, Billerica, MA)

- Normal goat serum
- Fluorescent antimouse secondary antibody
- DAPI (Molecular Probes, Life Technologies), 10 mg/l

7. Storage of free nuclei
- Sucrose, 30% in PBS
- Antifreezing solution (30% glycerol and 30% ethylene glycol in 0.024M phosphate buffer; use 10× dilution of 0.24M phosphate buffer, which is 30.8 g NaOH and 117.12 g NaH_2PO_4 in 4 l of distilled water)

Methods

Tissue fixation

1. Perfuse the animal of interest with saline followed by 4% paraformaldehyde. This step can be skipped for small tissues, such as embryonic mouse brains or invertebrate ganglia, which can be immersion-fixed.

2. Remove the brain from the skull; remove the dura mater and major superficial blood vessels from the fixed brain (for other body structures, remove any connective tissue and blood vessels).

3. Allow the tissue to postfixate by immersion in 4% paraformaldehyde. The ideal postfixation time is 2–4 weeks.

Tissue dissection

4. Under a stereoscope, dissect the regions of interest (ROIs).

5. Weigh the dissociated ROIs to be counted so that cell densities can be determined later.

6. Store the dissected ROIs in 4% paraformaldehyde if further postfixation is required (that is, if the tissue is not yet well fixed or has not been immersion-fixed for ≥2 weeks). Store them in PBS for immediate use, or in antifreezing solution for long-term storage until dissociation (see step 45, below).

Tissue dissociation

7. Place the dissociated tissue inside the homogenizer tube. Small tissues (approximately ≤50 mg, or 2 mm diameter) can be dissociated directly. Large tissues, such as whole cortical areas (≤1 g of tissue), need to be diced in a petri dish before homogenizing. Wash any leftovers in the dish and in your scalpel into the homogenizer tube using the dissociation solution. Note: It is fundamental that all tissue be homogenized. Much larger tissues (e.g., very large cortical areas, whole cerebella, spinal cords, or whole brains) must be divided into smaller portions of ~1 g to be dissociated separately and combined in a graduated cylinder.

8. Add dissociation solution to the homogenizer to a final volume that is approximately 10 times larger than the tissue to be dissociated, and large enough for the glass tube to be filled with fluid when the piston is fully inserted into the homogenizer. Use this volume to wash down into the tube any tissue fragments that stick to the walls of the homogenizer.

9. Insert the piston, and homogenize the tissue by making simultaneous up-and-down and rotating movements with the piston. Hold the tube upright at all times to avoid any spills. Use care not to let air into the tube, or foam will result.

10. Homogenization is over when no more tissue fragments are visible; this should take 10–30 min of grinding. To check for remaining tissue fragments, raise the homogenizer against the light, with the piston fully inserted, and look for small specks of tissue while gently rotating the piston. When no more specks are visible, proceed to the next step.

11. Wash the walls of the homogenizer. First, place the tube in a stand, remove the piston carefully, and use a fresh volume of dissociation solution to wash the walls of the piston into the tube. Once no material is left on the piston, place it on the bench and use another fresh volume of dissociation solution to wash the material left on the walls of the homogenizer into the tube. This collects into the main suspension any nuclei left behind on the glass walls.

12. Collect the nuclei suspension into a 15 ml or 50 ml graduated centrifuge tube. To do this, do not pour the contents of the homogenizer into the graduated tube. Rather, use a long Pasteur pipette to pick up the suspension (starting from the bottom of the tube, where the nuclei are densest) and transfer it to the graduated tube. Once all the suspension is transferred, use a fresh volume of dissociation solution to wash the walls of the homogenizer, collecting into the bottom of the tube any nuclei left on the glass walls. Transfer this volume to the same graduated tube. Repeat the wash approximately two more times or as needed, using small volumes in each wash, until the fluid in the transfer pipette is perfectly clear.

NOTES

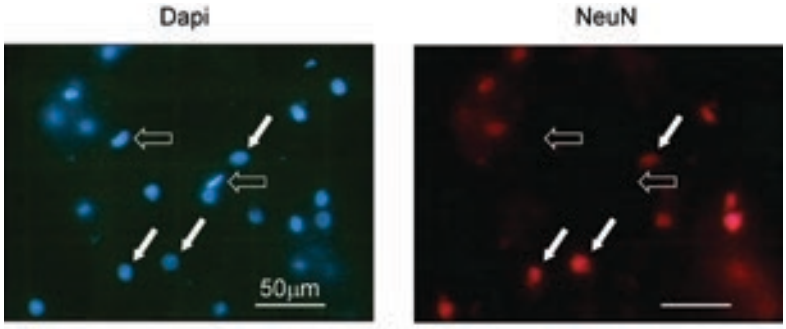

Figure 1. Appearance of isolated, DAPI-stained, and NeuN-stained nuclei. Left, Isolated nuclei have clearly delimited contours, indicating that the nuclear membrane is intact, and are brightly stained with DAPI. Notice that the nuclear morphology is preserved by the fixation. Right, Nuclei that are also stained by labeling with anti-NeuN antibody are readily identifiable against a dark background of virtually nonexistent, nonespecific staining. Filled arrows, examples of NeuN-positive nuclei; open arrows, examples of NeuN-negative nuclei. Scale bar, 50 µm.

13. Now that the entire suspension containing all cell nuclei in the original structure is in the graduated tube, add DAPI to it, diluting it 20–50 times from a 10 mg/l stock solution. The dilution required depends on how dense the nuclei suspension is; for a same-suspension volume, denser structures such as the cerebellum will require more DAPI (for instance, a 20× dilution only) to achieve sufficient labeling that is stable under UV illumination.

14. Use PBS to complete the suspension volume to a defined value in the graduated tube. The precise value is not important, as long as it can be read with precision on the tube.

Counting total cell numbers

15. Make the nuclei suspension homogeneous by inverting the graduated tube 10–20 times, taking care to avoid forming foam.

16. Immediately after making the suspension homogeneous, collect four 10 µl samples and place them in different chambers of two hemocytometers. Allow 1–2 min for nuclei to sink.

17. Under low magnification in the fluorescence microscope, verify the quality of the preparation. Check to see whether the nuclei are free and well distributed, without clumps (Fig. 1, left). Under high magnification (400×), verify that the nuclei are well labeled with DAPI, appearing brightly blue under UV illumination, and that the vast majority are intact, with preserved contours.

18. Count the number of nuclei in a same, known volume for each chamber. For instance, if nuclei in all 25 fields of the center grid are counted, that amounts to the number of cell nuclei in a volume of 0.0001 ml of the suspension. If there are ≥50–60 nuclei in the ensemble of the 25 central fields, then proceed to step 19. If not, then go to step 18A.

18A. Increase the density of nuclei in the suspension to be counted. This step is necessary to ensure that the counts will be reproducible and not subject to Poisson variation. To do this, spin down the graduated tube with the nuclei suspension in a clinical centrifuge (the exact time required depends on the diameter of the rotor; typically, 8 min at 3200 rpm suffice to ascertain that all nuclei are collected in a pellet). Remove the supernatant with a Pasteur pipette without disturbing the pellet; then add PBS to a precise final volume that is small enough to ensure that there will be >60 nuclei per 0.0001 ml of the suspension. Repeat step 18.

19. Average the number of nuclei counted in the same volume across the four samples, and verify whether the coefficient of variation (CV), which amounts to the SD of the values divided by the average value, is <0.15. Typically, the CV is <0.10. If it is not, make the suspension more homegeneous by agitation and count new samples. Additional samples can also be counted until CV <0.15.

20. Calculate the total number of nuclei in the suspension by simply multiplying the number of nuclei per ml by the total suspension volume. If you determined the average number of nuclei in

a volume of 0.0001 ml (that is, the 25 central fields of the chamber), then multiply that average by 10,000 to find the number of nuclei per ml of the suspension. Next, multiply that value by the total volume of the suspension.

21. Make the suspension homogeneous again by inverting the graduated tube and collecting 1 ml into an Eppendorf tube.

22. Spin down nuclei for 5 min in a microcentrifuge. Remove supernatant with a micropipette without disturbing the pellet.

23. If the tissue of interest has been in fixative for <6 weeks, then proceed to step 28. If not, proceed to step 24.

Heat-induced epitope retrieval

24. Add 1 ml of PBS to the pellet and dissolve it completely, using the micropipette if necessary. Do not vortex. Spin down nuclei again and remove supernatant.

25. Repeat step 24 a total of 3 times (that is, wash nuclei 3 times in PBS).

26. Add 1 ml of 0.2 M boric acid, pH 9.0, to the pellet (to break down the excess of aldehydes and the autofluorescence they cause), and dissolve the pellet completely, using the micropipette if necessary. Do not vortex.

27. Incubate at 70°C for 45 min, then spin down nuclei to remove supernatant.

Immunocytochemical identification of specific nuclear types

28. Add 1 ml of PBS to the pellet and dissolve it completely, using the micropipette if necessary. Do not vortex. Spin down nuclei again and remove supernatant.

29. Repeat step 28 a total of 3 times (that is, wash nuclei 3 times in PBS).

30. Add 199 µl of PBS to the pellet and 1 µl of anti-NeuN primary antibody (1:200 dilution). Alternatively, use the appropriate dilution of the desired antibody. Dissolve the pellet completely, using the micropipette. Do not vortex.

31. Incubate at room temperature for 2 h, preferably under agitation.

32. Spin down the nuclei for 5 min in a microcentrifuge. Remove supernatant with a micropipette without disturbing the pellet.

33. Add 1 ml of PBS to the pellet and dissolve it completely, using the micropipette if necessary. Do not vortex. Spin down nuclei again and remove supernatant.

34. Repeat step 33 a total of 3 times (that is, wash nuclei 3 times in PBS).

35. Add the secondary antibody in the required dilution in the presence of 10% normal goat serum and 10% DAPI. Dissolve the pellet completely, using the micropipette. Do not vortex.

36. Incubate at room temperature for 2 h, preferably under agitation.

37. Spin down the nuclei for 5 min in a microcentrifuge. Remove supernatant with a micropipette without disturbing the pellet.

38. Add 1 ml of PBS to the pellet and dissolve it completely, using the micropipette if necessary. Do not vortex. Spin down nuclei again and remove supernatant.

39. Repeat step 38 a total of 3 times (that is, wash nuclei 3 times in PBS).

40. Add 1 ml of PBS to the pellet and dissolve it completely, using the micropipette if necessary. Do not vortex.

41. After agitating the tube, remove a 4 µl sample and place it in the Neubauer chamber. Allow 1–2 min for the nuclei to set.

42. Under 400× magnification, determine the percentage of DAPI-labeled nuclei that also show labeling with the antibody (Fig. 1). The total number of nuclei that needs to be counted depends on the frequency of antibody-stained nuclei; the smaller the percentage of stained nuclei, the larger the total number of nuclei that must be counted. Given that usually 30%–90% of nuclei in any brain structure are NeuN-positive, a minimum of 500 nuclei should be counted.

NOTES

43. Determine the total number of neurons (that is, NeuN-positive nuclei) in the structure using the formula (% $NeuN^+$ nuclei × total number of nuclei)/100.

44. Determine the total number of nonneuronal cells (that is, NeuN-negative nuclei) in the structure as (total number of cells – $NeuN^+$ cells).

Storage of free nuclei

45. For later reanalysis of nuclei (e.g., with another antibody or morphological criterion), collect the remaining nuclei for storage by spinning them down in a centrifuge.

46. Discard the supernatant and resuspend the nuclei in 30% sucrose in PBS. Allow ≥2 h for the nuclei to equilibrate and start to descend in the tube.

47. Spin down the nuclei, discard the supernatant, and resuspend the nuclei in antifreezing solution. Allow ≥2 h for the nuclei to equilibrate and start to descend in the tube.

48. Store at –20°C until the next use. Frozen nuclear suspensions can be utilized for immunocytochemistry. In that case, agitate the frozen suspension before taking a 1 ml sample for processing, spin down the nuclei, and proceed either to step 24 (if epitope retrieval is required) or to step 28.

Acknowledgments

Thanks to Roberto Lent for encouraging and supporting the creation of this method, to Jon Kaas for continued support, to Christine Collins for improving the method with the FACS variation, and to Paul Manger for insights on tissue storage. The development and improvement of this method was made possible by grants from Conselho Nacional de Desenvolvimento Cientifico e Tecnológico (CNPq) and Fundação de Amparo à Pesquisa do Estado do Rio de Janeiro (FAPERJ).

This chapter has been published previously as The isotropic fractionator: a fast, reliable method to determine numbers of cells in the brain or other tissues (2012) In: Neuronal network analysis: concepts and experimental approaches (Fellin T, Halassa M, eds), pp. 391–403. New York: Humana Press.

References

Azevedo FAC, Carvalho LRB, Grinberg LT, Farfel JM, Ferretti REL, Leite REP, Jacob Filho W, Lent R, Herculano-Houzel S (2009) Equal numbers of neuronal and non-neuronal cells make the human brain an isometrically scaled-up primate brain. J Comp Neurol 513:532–541.

Bahney J, von Bartheld CS (2014) Validation of the isotropic fractionator: Comparison with unbiased stereology and DNA extraction for quantification of glial cells. J Neurosci Meth 222:165–174.

Bandeira FC, Lent R, Herculano-Houzel S (2009) Changing numbers of neuronal and non-neuronal cells underlie postnatal brain growth in the rat. Proc Natl Acad Sci USA 106:14108–14113.

Collins CE, Young NA, Flaherty DK, Airey DC, Kaas JH (2009) A rapid and reliable method of counting neurons and other cells in brain tissue: a comparison of flow cytometry and manual counting methods. Front Neuroanat 9:5.

Gabi M, Collins CE, Wong P, Kaas JH, Herculano-Houzel S (2010) Cellular scaling rules for the brain of an extended number of primate species. Brain Behav Evol 76:32–44.

Gittins R, Harrison PJ (2004) Neuronal density, size and shape in the human anterior cingulated cortex: a comparison of Nissl and NeuN staining. Brain Res Bull 63:155–160.

Herculano-Houzel S, Lent R (2005) Isotropic fractionator: a simple, rapid method for the quantification of total cell and neuron numbers in the brain. J Neurosci 25:2518–2521.

Herculano-Houzel S, Mota B, Lent R (2006) Cellular scaling rules for rodent brains. Proc Natl Acad Sci USA 103:12138–12143.

Herculano-Houzel S, Collins C, Wong P, Kaas JH (2007) Cellular scaling rules for primate brains. Proc Natl Acad Sci USA 104:3562–3567.

Herculano-Houzel S, Ribeiro P, Campos L, da Silva AV, Torres LB, Catania KC, Kaas JH (2011) Updated neuronal scaling rules for the brains of Glires (rodents/lagomorphs). Brain Behav Evol 78:302–314.

Herculano-Houzel S, Watson C, Paxinos G (2013) Distribution of neurons in functional areas of the mouse cerebral cortex reveals quantitatively different cortical zones. Front Neuroanat 7:35.

Herculano-Houzel S, Avelino-de-Souza K, Neves K, Porfírio J, Messeder D, Calazans I, Mattos L, Maldonado J, Manger PM (2014) The elephant brain in numbers. Front Neuroanat 8:46.

Miller DJ, Balaram P, Young NA, Kaas JH. Three counting methods agree on cell and neuron number in chimpanzee primary visual cortex. Front Neuroanat 8:36.

Mullen RJ, Buck CR, Smith AM (1992) NeuN, a neuronal specific nuclear protein in vertebrates. Development 116:201–211.

Neves K, Ferreira Meireles F, Tovar-Moll F, Gravett N, Bennett NC, Kaswera C, Gilissen E, Manger PR, Herculano-Houzel S (2014) Cellular scaling rules for the brain of afrotherians. Front Neuroanat 8:5.

Ribeiro PFM, Ventura-Antunes L, Gabi M, Mota B, Grinberg LT, Farfel JM, Ferretti REL, Leite REP, Jacob Filho W, Herculano-Houzel S (2013) The human cerebral cortex is neither one nor many: neuronal distribution reveals two quantitatively different zones in the grey matter, three in the white matter, and explains local variations in cortical folding. Front Neuroanat 7:28.

Sarko DK, Catania KC, Leitch DB, Kaas JH, Herculano-Houzel S (2009) Cellular scaling rules of insectivore brains. Front Neuroanat 3:8.

West MJ (1999) Stereological methods for estimating the total number of neurons and synapses: issues of precision and bias. Trends Neurosci 22:51–61.

The Filament Editor: An Interactive Software Environment for Visualization, Proof-Editing, and Analysis of 3D Neuron Morphology

Vincent J. Dercksen,[1] Hans-Christian Hege,[1]
and Marcel Oberlaender, PhD[2,3,4]

[1]Department of Visualization and Data Analysis
Zuse Institute Berlin
Berlin, Germany

[2]Computational Neuroanatomy Group
Max Planck Institute for Biological Cybernetics
Tübingen, Germany

[3]Digital Neuroanatomy
Max Planck Florida Institute
Jupiter, Florida

[4]Bernstein Center for Computational Neuroscience
Tübingen, Germany

Introduction

Neuroanatomical analysis, such as classification of cell types, depends on reliable reconstruction of large numbers of complete three-dimensional (3D) dendrite and axon morphologies. At present, the majority of neuron reconstructions are obtained from preparations in a single tissue slice *in vitro*, suffering from cutoff dendrites and, more dramatically, cutoff axons. In general, axons can innervate volumes of several cubic millimeters and may reach path lengths of tens of centimeters. Thus, their complete reconstruction requires *in vivo* labeling, histological sectioning, and imaging large fields of view. Unfortunately, anisotropic background conditions across such large tissue volumes, as well as faintly labeled thin neurites, result in incomplete or erroneous automated tracings and even lead experts to make annotation errors during manual reconstructions. Consequently, unreliable tracing comprises the major bottleneck for reconstructing complete 3D neuron morphologies.

During the past 20 years, many technical barriers for reconstructing single neurons have been overcome. Labeling neurons using intracellular or cell-attached pipettes has allowed reconstructing large parts of individual neurons, thereby linking their structure with activity patterns *in vitro* and *in vivo*. In addition to such conventional techniques, genetic labeling methods based on fluorescent proteins have started the identification and reconstruction of relatively uniform, molecularly identified cell populations. Further, digital imaging has advanced rapidly. New imaging methods, such as high-speed mosaic/optical-sectioning wide-field and confocal systems, as well as block-face two-photon (Ragan et al., 2012) and light-sheet (Dodt et al., 2007) microscopes, promise high-resolution imaging of large brain regions. Finally, the limitations on archiving terabyte datasets have disappeared with the falling costs of hard disk drives. As a result of these developments, various manual, semiautomated, and fully automated approaches for reconstructing single neuron morphologies have been reported (Meijering, 2010; Donohue and Ascoli, 2011).

The vast majority of single neuron tracings has so far been obtained from *in vitro* preparations, i.e., individual neurons are labeled within a tissue slice usually of 300 µm thickness. However, reconstructing the complete 3D dendrite and axon morphology of individual neurons requires *in vivo* labeling in combination with histological sectioning of the brain (i.e., due to penetration limits of staining and imaging methods) and subsequent imaging of large tissue volumes. Tracing of faintly labeled, long-range projecting thin neurites and recovering across-section continuity of neuronal branches thus make reconstructions of *in vivo* labeled neurons a major challenge in neuroscience research (Svoboda, 2011). Nevertheless, for sparsely labeled tissue, reconstruction results are usually assumed to be highly reliable, although little validation of this reliability has been reported (Helmstaedter et al., 2011).

Here, we present the Filament Editor (FE), a novel set of tools integrated into a software environment specifically designed to reliably reconstruct and validate single neuron tracings from sparsely labeled *in vivo* preparations. The FE comprises tools for visualizing and interactively correcting 3D neuron tracings, alignment, and across-section continuity, allowing for efficient proof-editing within and across brain sections. In addition, the FE incorporates advanced annotation and morphometric analysis functionalities. We illustrate the applicability of the FE on frequently occurring use cases and demonstrate that the proof-editing routines can result in unambiguous tracings of *in vivo* labeled axons.

Methods

Data structure

The FE has been developed based on Amira software (FEI Visualization Sciences Group, 2013a), a visualization framework frequently used in neuroscience research. Neuron morphology is represented in the FE by the *SpatialGraph* data structure (Fig. 1). The topological skeleton of the graph is defined by a set of nodes, connected by a set of (unbranched) edges. The edge direction is defined by specification of the source and target node. The graph is embedded in space by associating 3D coordinates with each node. The edge trajectory is defined by a sequence of 3D points (vertices). The first and last point of each edge coincides with the source and target node, respectively. The data structure was designed to allow interactive editing and rendering of large 3D tracings (e.g., >10 k edges, >1 M points). For traversing the graph, an adjacency list is maintained for each node. Points are stored as coordinate arrays per edge for efficient rendering as line strips. Labels are used to associate semantic information with substructures of the graph, e.g., "Dendrite," "Axon," and "Soma" (Figs. 1*a*, *d*). Additionally, numerical attributes can be defined, e.g., a floating-point value representing the radius at each edge point. Multiple attributes can be defined on nodes, edges, and points simultaneously. Tracings can be imported into the FE using the *SWC* (Cannon

NOTES

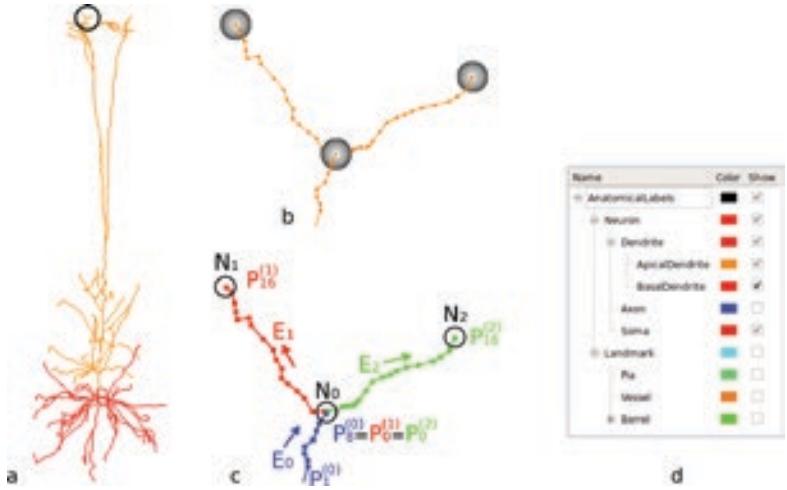

Figure 1. The *SpatialGraph* data structure. ***a***, Dendritic tree of a layer 5 pyramidal neuron, colored according to the anatomical labels defined in ***d***. ***b***, Magnification of the encircled region of ***a***. The nodes (gray spheres) are connected by edges, represented and displayed as polygonal lines defined by edge points (or points, for short; displayed as squares). ***c,*** Schematic representation of the *SpatialGraph* object in ***b***. The object consists of three directed edges (E_0, E_1, E_2), which interconnect the nodes N_0, N_1, N_2 (the source node of E_0 is not displayed). At branching nodes, the last point of the incoming edge ($P_8^{(0)}$ on edge E_0) coincides with the first point of the outgoing edges ($P_0^{(1)}$ and $P_0^{(2)}$ on E_1 and E_2, respectively). ***d***, Semantic information can be associated with the morphology using labels. The *Label Viewer* is used for editing label hierarchies, assigning labels to graph elements, and selecting these elements for editing, visualization, and analysis.

et al., 1998), *hoc* (Carnevale and Hines, 2006), or the AmiraMesh file format. These formats, as well as MorphML (Crook et al., 2007), can be used to export the tracings.

Visualization

The FE provides a two-dimensional (2D) and 3D viewer for proof-editing a tracing. The 3D viewer displays the graph using spheres for the nodes, squares for the points, and polylines for the edges. The user can inspect the spatial structure of the tracing in 3D by camera rotation, zooming, and panning using the mouse and edit each of the graphs' components. Nodes, edges, and points can be colored according to one of the label attributes. The 3D viewer can display additional data using any available Amira display module (FEI Visualization Sciences Group, 2013b). For example, the neuron morphology can be jointly visualized with the image data using volume rendering, 2D slices, or intensity projections. The *SpatialGraph* can be visualized as tubes by mapping a radius attribute defined on edge points to cylinder thickness. The 2D viewer displays a slice of user-defined thickness of the graph, superimposed on a maximum intensity projection (MIP) of the corresponding 3D image region. Hiding the remaining image and tracing regions provides an unobstructed view to locally verify the tracing with respect to the image stack. By varying the slice depth and/or orientation, the user navigates through the volume.

Selection tools

Modification of the traced morphology is achieved by selecting one or more elements (nodes, edges, points), followed by the invocation of an operation (e.g., deletion). To provide a selection system that is "powerful" (i.e., allowing efficient selection of any subset of elements) and "forgiving" (i.e., the selection itself can easily be modified), the following tools are available in the FE:

1. ***Single-Element Selection***: selects single nodes, edges, or points that have been clicked on with the mouse;

2. ***Connected-Component Selection:*** selects the entire subgraph connected to the element that has been clicked on with the mouse;

3. ***Lasso Selection***: selects all nodes and edges within a user-drawn polygon. Using a modifier key, only connected components that are completely contained within the Lasso polygon are selected;

4. ***Select-All, Clear and Invert Selection***: selects the entire *SpatialGraph*, deselects, and inverts the current selection, respectively; and

5. ***Label Selection***: selects graph elements with a particular attribute by clicking on the respective label in the *Label Viewer* (Fig. 1*d*). Holding down

a modifier key adds to the current selection. Selected items are highlighted in the viewers.

Editing operations

The following operations are available to manipulate the data structure:

1. ***Deletion*** of selected nodes and edges;

2. ***Splicing*** (connecting) edges. Splicing is achieved by selecting either two nodes, two points, or one point and one node, followed by the invocation of the connect operation. Nodes are connected by a new straight edge. Selected points are converted to nodes, as they will be branching points; the new nodes are subsequently connected by adding an edge with the smallest Euclidean distance;

3. ***Point-to-Node Conversion*** converts a selected point into a node, resulting in an edge split. The inverse *Node-to-Point* operation concatenates two edges while removing the intermediate node. The latter can be run for all intermediate nodes at once. Together with the *Remove-Isolated-Nodes* operation, all nodes that are neither branching nor terminal nodes can be purged from the graph;

4. ***Edge-Smoothing***. *Edges* are smoothed by repositioning their edge points as follows: the user specifies the neighborhood size N, which must be odd. The position of each point $\boldsymbol{p}_i$ on the edge is replaced by the average of its own position and the $M = (N-1)/2$ points along both directions:

$$\boldsymbol{p}'_i = \frac{1}{N}\sum_{k=i-M}^{i+M} \boldsymbol{p}_k.$$

   The first and last M points on the edge are not moved, effectively leaving all nodes in place; and

5. ***Transformation***. An affine transformation can be applied to tracings, images, or any other 3D dataset. For example, a linear scaling could be applied, independently for all dimensions, to compensate for tissue shrinkage. All editing operations can be *undone/redone*.

Semantic labels

Semantic information can be associated with nodes, edges, and points by assigning labels. A label is a name (i.e., a string), uniquely identified by an integer value and associated with a color. Labels are organized in a hierarchical fashion, i.e., in a tree data structure, providing access to graph substructures at different levels of detail. Upon creation of a node (or edge/point) label attribute, each node (or edge/point) is assigned a label from the tree. The *Label Viewer* (Fig. 1*d*) is part of the FE user interface allowing the user to define and edit custom label trees, assign labels to selected substructures of the graph, and select these substructures for editing, visualization, and analysis. For example, one could define a hierarchical label tree with the root label "Neuron" having child labels "Axon" and "Dendrite" and assign these to the respective edges and nodes. Alternatively, the *Label Viewer* supports flat label hierarchies. For example, the "identify loops" functionality automatically assigns all edges comprising a loop the same label, pinpointing potential autapses (i.e., an intersecting dendrite and axon from the same cell) or falsely connected branches.

Section alignment

The FE incorporates an automated method (Dercksen et al., 2009) for rigid alignment of tracings obtained from adjacent image stacks, e.g., from consecutive brain sections. The automated algorithm is complemented by a user interface for interactive manual alignment (Fig. 2*a*). First, tracings from adjacent image stacks are merged using the *CreateSpatialGraphStack* module. This module generates a new *SpatialGraph* by positioning tracings from image stacks obtained from adjacent brain sections at either fixed distances along the z-axis (i.e., perpendicular to the cutting plane) or such that the bounding boxes adjoin. Tracings from image stacks obtained from the same brain section can be merged without (z-)translation for subsequent manual alignment. The nodes and edges are assigned identifier labels that refer to the corresponding image stack. Transformations can thus be applied to tracings of each individual stack by transforming all nodes and edges with a particular label. The stack of tracings is aligned by repeated pairwise alignment of neighboring sections. The automated method (Dercksen et al., 2009) uses a 2D point-matching approach to compute the optimal transform, i.e., a rotation angle around the z-axis and a 2D translation parallel to the xy-plane. The points to be matched are the terminal nodes in the top and bottom region of each section, e.g., within the upper and lower 25% (Fig. 2*b*). The algorithm is sufficiently fast to be used in an interactive workflow, with response times ranging from a fraction of a second for a small number of end points (~30) to several seconds for a larger set (~100). Sections can be aligned simultaneously or pairwise. The resultant alignments appear in the

NOTES

3D viewer, allowing visual validation (Fig. 2*c*). In cases where the automated alignment result is not satisfactory, the user can interactively translate and rotate each section with respect to its predecessor section in the 3D viewer using handles. All other sections can be hidden so as not to obscure the view.

Interactive manual tracing

The interactive tracing functionality available in the 2D viewer can be used to manually add filamentous and/or anatomical reference structures. The user adds new nodes by clicking on the desired location in the image. The node is added at the mouse cursor position at the depth of the image plane (for 2D images) or the depth with highest image intensity (3D image). The node is automatically connected to the latest created node by a new edge. This feature can be used to augment automatically generated tracings, for example, with contours representing anatomical landmarks, such as pia, white matter, or blood vessel outlines (Fig. 3*a*), as well as with 2D outlines of the soma in different optical or histological sections.

Visual and quantitative morphometric analysis

The FE includes the following functionalities for visual and quantitative morphometric analysis (Fig. 3):

1. Branch length and node statistics for the entire graph or for a selected subgraph, grouped by semantic labels;
2. Quantitative measurement and visualization of branches within or outside a reference volume (Fig. 3*a*). The length contained within a volume is computed by intersecting all edge segments with the triangles comprising the bounding surface, performing a point location test, and accumulating the length of the confined branches. The parts of the morphology contained within a volume can be visualized further by labeling the edge points by the name of the respective structure and coloring the graph according to these labels (Fig. 3*a*);
3. 3D density of morphological properties. A 3D grid of user-defined voxel size is superimposed onto the morphology, and morphological properties of the tracing within each voxel (Fig. 3*b*) are computed. Branch length within a voxel is computed by clipping each segment between adjacent edge points against the voxel's bounding box and accumulating the resulting lengths; and
4. 1D profile of morphological properties. By accumulating the values in voxels in each plane of the 3D voxel grid described above, a 1D profile of the property of interest along an axis can be extracted (Fig. 3*c*).

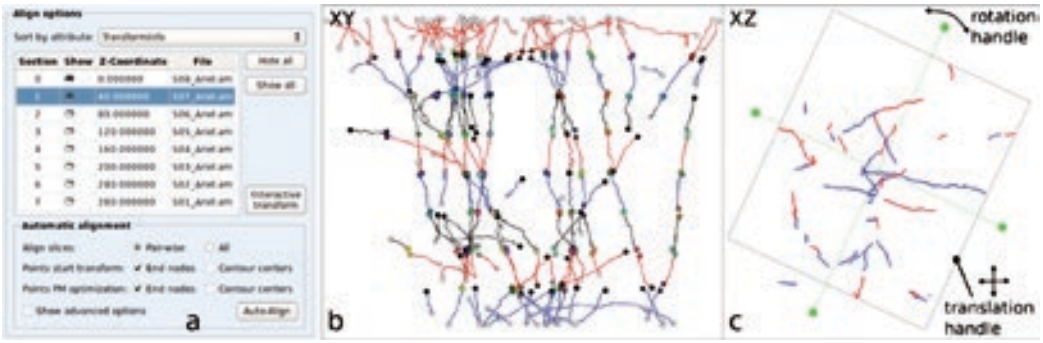

Figure 2. Section alignment. ***a,*** The *Align* toolbox provides access to both automated and interactive manual alignment. The section list allows one to (1) select a section to align, (2) toggle section visibility, and (3) manually adjust the *z*-position of a section. ***b,*** *XY*-view after alignment of eight sections. Edges are colored by section, alternating red, blue, and black. Nodes are colored by matching result. Matching nodes in different sections are assigned the same label, and thus the same color. Black nodes could not be matched; white nodes were not used for alignment. ***c,*** Interactive manual alignment using a handle. Only the section that is currently transformed (red, highlighted in the table in ***a***) and its predecessor (blue) are visible; other sections are hidden to not obscure the view.

Visual and quantitative comparison of tracings

Comparison of tracings obtained from the same image data requires defining their correspondence. We implemented such a comparison metric based on Helmstaedter et al., 2011: Given a set of reconstructions $R_1 \ldots R_N$ (N being the number of users), first, edge points are inserted on all edges (without modifying the trajectory) such that the distance between any two consecutive edge points is smaller than a maximum sampling distance D. Second, the reconstruction R_1 is compared with the reconstructions of all other users $R_2 \ldots R_N$, respectively. For each edge point $\boldsymbol{p}$ on R_1, the number of reconstructions that have a point $\hat{\boldsymbol{p}}$ that corresponds to $\boldsymbol{p}$ is counted. $\hat{\boldsymbol{p}}$ corresponds to $\boldsymbol{p}$ if they are no further than a maximum correspondence distance R apart, i.e., $|\hat{\boldsymbol{p}} - \boldsymbol{p}| \leq R$. This results in the number of corresponding reconstructions $C(\boldsymbol{p}) \in [1,N]$; $C(\boldsymbol{p}) = 1$ if there is no other reconstruction with a matching point (R_1 agrees only with itself in $\boldsymbol{p}$); $C(\boldsymbol{p}) = N$ if all other reconstructions have a matching point. Third, the total length of all edges of R_1 is divided among N bins $L_1 \ldots L_N$. A bin L_i represents the length of R_1 that was agreed on by i reconstructions. To this end, all straight segments between pairs of successive edge points $\boldsymbol{p}$ and $\boldsymbol{q}$ are regarded. If $C(\boldsymbol{p}) = i$, and $C(\boldsymbol{q}) = j$, then half the length of segment $\boldsymbol{pq}$ is added to L_i, and half to L_j. The length bins are computed separately for all other reconstructions $R_2 \ldots R_N$. The length per bin is presented to the user in a spreadsheet. To visualize the correspondences, an integer attribute is defined on the edge points, storing the value of $C(\boldsymbol{p})$ for each point. Displaying one or more reconstructions colored according to this value effectively pinpoints interuser differences.

Results

Application example: 3D reconstruction of individual axons labeled *in vivo*

We illustrate a potential workflow using the tools of the FE to generate complete 3D morphologies for the example of *in vivo* labeled axons, reconstructed by a previously reported automated imaging and tracing pipeline (Oberlaender et al., 2007).

Preprocessing: sample preparation, imaging and tracing

Briefly, individual neurons in rat vibrissal thalamus (Oberlaender et al., 2012a) were filled with biocytin using whole-cell patch–clamp recordings *in vivo*. After perfusion, brains were fixed and cut into 50-µm-thick consecutive vibratome sections. Using a custom-designed mosaic/optical-sectioning bright-field microscope (Oberlaender et al., 2007, 2009), 3D image stacks of typically 2 × 2 × 0.05 mm volumes were acquired in vibrissal cortex at a resolution of 0.184 × 0.184 × 0.5 µm per voxel. Neuronal structures were automatically extracted from eight consecutive image stacks using previously reported and validated automated tracing software

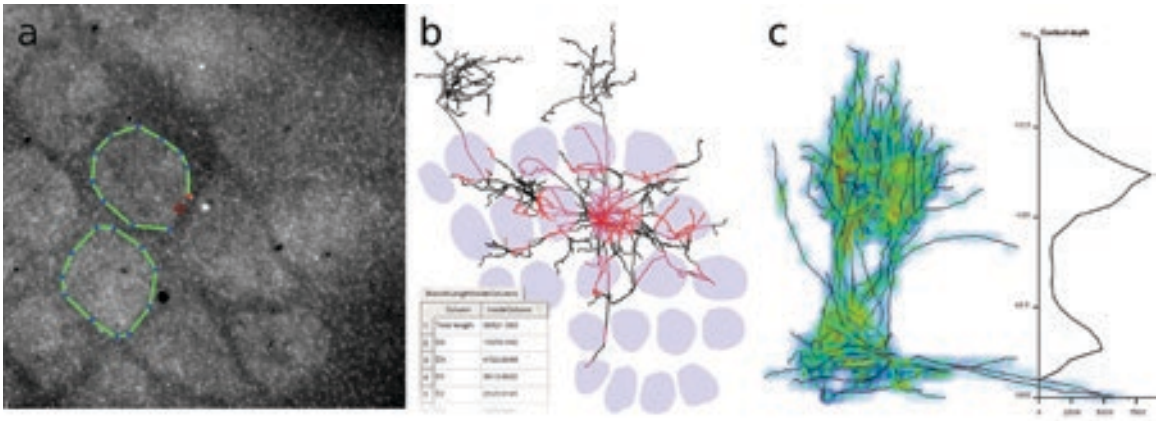

Figure 3. Morphometric analysis. ***a,*** Manual drawing of anatomical landmark contours. Contours outlining "barrel columns" in rat vibrissal cortex (S1) are created by clicking on the MIP image. A new node (red) is automatically connected to the previously created node by an edge (green). ***b,*** Visual and quantitative analysis of semantically labeled neuronal branches with respect to anatomical reference structures. Here, axonal length of a layer 5 slender-tufted pyramidal neuron is evaluated with respect to the barrel columns in S1 (Oberlaender et al., 2011). The axon length within and outside each column was automatically computed, exported to a spreadsheet, and visualized by labeling all edge points as either inside (red) or outside (black) any cortical column. ***c,*** Branch density visualization and quantification. A grid of 50 µm voxels is superimposed onto a reconstructed axon labeled in rat vibrissal thalamus *in vivo* (Oberlaender et al., 2012a). For each voxel, the total axon length is computed and visualized in 3D or as 1D density profile by accumulating length densities across each *x/y* plane.

NOTES

named "*NeuroMorph*" (Oberlaender et al., 2007). Projection images of each image stack, as well as 3D skeletons of neuronal branches (i.e., *SpatialGraph* files), represent the final results of the automated pipeline for each brain section. A position label is assigned to all edges. The labels indicate whether the connected component containing the edge (1) touches the top of the section (blue), (2) touches the bottom (green), (3) passes through (i.e., touches top and bottom) (red), or (4) touches neither top nor bottom (yellow).

Proof-editing of tracings from individual image stacks

The FE is used to interactively splice (connect) fragmented edges and to delete falsely traced edges from the automated tracing in each individual section. The tracing data are superimposed on the MIP of the respective image stack. Four typical proof-editing situations can occur:

- **Case 1:** *Splicing*. The tracing algorithm may generate a fragmented result, for example, because of poorly stained regions in the axial direction. In such cases, the MIP and position label colors facilitate identification of potentially contiguous parts. By 3D rotation of the camera, human pattern recognition can quickly resolve this. Using the selection and splicing tools, gaps between identified fragments can be closed.
- **Case 2:** *Creating new branching points*. A new branching connection is created by selecting a terminal node and a point on a different edge. The latter will be converted into a branching node when applying the splice operation. The most likely location of the new branching node can easily be resolved by human pattern recognition, using the position-dependent coloring and 3D camera rotation of the tracing and MIP.
- **Case 3:** *Removal of false segmentations*. The *NeuroMorph* algorithms are designed to accept oversegmentation to ensure that no faintly stained axons are falsely discarded. The Lasso tool provides a dedicated mode to select only connected subgraphs that are entirely contained within a user-drawn polygon. This allows one to select all small artifacts in the neighborhood of a reconstructed neuronal process at once and to delete them, without affecting the larger structure.
- **Case 4:** *Removal of false connections*. Occasionally, nearby branches may have been falsely connected by the tracing algorithm. The *NeuroMorph* algorithms may have created tracings whose spatial structure is difficult to verify from the 2D MIP image. For example, the 3D view may reveal that the structure consists of two parallel axonal branches connected by a "bridge." To correct the false connection, the user selects the bridging edge and removes it.

Alignment and proof-editing across multiple image stacks

An important aspect of reconstructing complete 3D neuron morphologies is the merging of tracings obtained from multiple image stacks (e.g., consecutive brain sections). Here, tracings containing axonal branches from thalamocortical axons in eight consecutive brain sections were proof-edited as described above and then merged into a single *SpatialGraph* (see Methods). The tracings obtained from each image stack were translated in the *z*-direction, i.e., perpendicular to the cutting plane, such that their bounding boxes adjoin. The *Align* toolbox was then used to rigidly align the subgraphs corresponding to each section tracing. The automated algorithm determined the correct transformation for all tracings in the eight-section dataset. After alignment, the branches were connected across the section boundaries using the *Splicing* operation. The alignment and splicing process is regarded as the final quality control, as tracings of branches passing through multiple brain sections can be checked for continuity. The final tracing result is scaled in the *z*-direction to match the vibratome-defined thickness of the brain sections, compensating for potential tissue shrinkage. Further, smoothing along the *z*-direction is applied to remove staircase artifacts in the skeletons resulting from anisotropic voxel sizes. As a result, axonal branches of >1 cm path length, including 31 branching points, were extracted from this example dataset.

Interuser variability of proof-editing *in vivo* labeled neurons

The proof-editing of tracings obtained from individual image stacks, as well as the alignment and interconnection of tracings across image stacks, may introduce interuser variability to the final 3D neuron reconstructions. We validated the above-described tasks involving the FE by investigating the reproducibility of the final tracing result. To do so, 5 users proof-edited, merged, and aligned the 8 tracings of the example dataset. The users had varying degrees of experience. In brief, comparison of the proof-editing results produced by 5 different users indicated a high degree of accuracy of the final morphology. First, coarse comparison yielded only small differences in the number of branches (~1 error per 20 branches), branching nodes (~1 error per 31 branching nodes), and total length (~19 μm error per 1 mm axon).

Second, agreement in trajectories (see Methods) after proof-editing varied between 85.7% and 94.5% across individual image stacks. Third, differences in alignment were small, ~4 μm. Consequently, the trajectories of the final reconstructions across multiple image stacks were very similar: On average, 98.8% of the reconstructed trajectories were identical across users, using a correspondence radius of 5 μm. No significant differences were measured between expert and novice users. Specifically, the consensus length was computed for 2 groups consisting of the 3 most and 3 least experienced users, respectively. The average consensus length (i.e., at least 2 of 3 users agreed) as a percentage of the total length was 98.7% for the less experienced and 98.8% for the more experienced group (using the correspondence distance of R = 5 μm). The amount of manual labor required for proof-editing automated tracings decreased with experience from ~6.5 h to ~2 h per centimeter axon.

Discussion

The FE combines visualization, selection, and operation functionalities that allow interactive proof-editing and analysis of 3D neuronal tracings within an easy-to-use and intuitive graphical user interface. Using an example dataset of *in vivo* labeled thalamocortical axons from eight consecutive large, high-resolution image stacks, we illustrated four general situations that may occur during proof-editing any sparsely labeled morphology data. The relative abundance of each of the four use cases will, however, strongly depend on the image and labeling quality, as well as on the accuracy of the automated or manual tracing methods.

The example dataset used here can be regarded as one of the most challenging cases for reconstructing complete and accurate 3D neuron morphologies. First, the neuron was labeled in rat thalamus *in vivo*, whereas its axonal branches were imaged within vibrissal cortex, ~3 mm away from the recording site. Thus, in addition to faint staining caused by thin axonal diameters, diffusion of the tracer (i.e., biocytin) along centimeters of axon may have further decreased signal-to-noise ratios of terminal branches. Second, owing to the large axonal innervation volume (here 2 × 2 × 1 mm), the tissue was imaged using a bright-field microscope (at the diffraction limit of light) at the cost of contrast and axial resolution. Any fluorescent microscope system of superior contrast and resolution would require impractically long imaging times compared with the ~24 h required using the present system (Oberlaender et al., 2007, 2009). Third, because of the faint labeling and limited contrast, the automated tracing algorithms accept oversegmentation to guarantee that all axonal fragments are reconstructed, at the cost of picking up background structures.

The completeness of detecting and tracing all axonal fragments by the *NeuroMorph* system has been validated against manual results previously generated by human expert users (Oberlaender et al., 2007). Consequently, because the FE allows unambiguous proof-editing of the thalamocortical axons presented, datasets of higher contrast, higher resolution, or less background will certainly allow for an even faster and equally reliable proof-editing of complete 3D morphologies. Using a challenging dataset, we have illustrated that the combination of 3D image data (e.g., as a 2D MIP) with (1) 3D tracings (edges are rendered as polylines, nodes as spheres, points as squares); (2) semantic labeling; (3) 3D viewing (i.e., camera rotation, translation, and zoom); as well as (4) 3D selecting, hiding, and editing is a convenient, intuitive, and fast approach to extract reliable 3D morphologies from large, sparsely labeled images. Here, ~0.5 terabytes of image data, containing >1 cm of axonal fragments, could be proof-edited with 98.8% accuracy within 2–6 h.

In summary, we have presented the FE, a software toolbox integrating components for proof-editing neuron tracings in 3D, a cross-section alignment, and morphometric analysis. The FE addresses a clear need for efficient and effective proof-editing, advancing the possibilities for high-throughput reconstruction of accurate and complete 3D neuron morphology, as previously illustrated by the examples of determining cell types (Oberlaender et al., 2012b), axon projection patterns (Oberlaender et al., 2011), and plasticity during sensory deprivation (Oberlaender et al., 2012a).

Acknowledgments

This paper was published in unabridged format in Neuroinformatics 2014;12:325–339. Full methods and any associated references, as well as supplemental figures and movies, are available in the online version of the paper at http://link.springer.com/journal/12021. The FE and associated modules described in the full article can be obtained by acquiring Amira 5.5 and installing the ZIB extension package as described on following website: www.zib.de/en/visual/software/neuronreconstruction.html.

NOTES

References

Cannon RC, Turner DA, Pyapali GK, Wheal HV (1998) An on-line archive of reconstructed hippocampal neurons. J Neurosci Methods 84:49–54.

Carnevale NT, Hines ML (2006) The NEURON book. Cambridge, UK: Cambridge University Press.

Crook S, Gleeson P, Howell F, Svitak J, Silver RA (2007) MorphML: level 1 of the NeuroML standards for neuronal morphology data and model specification. Neuroinformatics 5:96–104.

Dercksen VJ, Weber B, Guenther D, Oberlaender M, Prohaska S, Hege HC (2009) Automatic alignment of stacks of filament data. In: Proc 2009 6th IEEE Int Symp on Biomedical Imaging: From Nano to Macro (ISBI), June 28–July 1, Boston, pp. 971–974.

Dodt HU, Leischner U, Schierloh A, Jahrling N, Mauch CP, Deininger K, Deussing JM, Eder M, Zieglgansberger W, Becker K (2007) Ultramicroscopy: three-dimensional visualization of neuronal networks in the whole mouse brain. Nat Methods 4:331–336.

Donohue DE, Ascoli GA (2011) Automated reconstruction of neuronal morphology: an overview. Brain Res Rev 67:94–102.

FEI Visualization Sciences Group (2013a) Amira 5.5. In.

FEI Visualization Sciences Group (2013b) Amira 5.5 Reference Guide. In.

Helmstaedter M, Briggman KL, Denk W (2011) High-accuracy neurite reconstruction for high-throughput neuroanatomy. Nat Neurosci 14:1081–1088.

Meijering E (2010) Neuron tracing in perspective. Cytometry A 77:693–704.

Oberlaender M, Bruno RM, Sakmann B, Broser PJ (2007) Transmitted light brightfield mosaic microscopy for three-dimensional tracing of single neuron morphology. J Biomed Opt 12:064029.

Oberlaender M, Broser PJ, Sakmann B, Hippler S (2009) Shack–Hartmann wave front measurements in cortical tissue for deconvolution of large three-dimensional mosaic transmitted light brightfield micrographs. J Microscop 233:275–289.

Oberlaender M, Boudewijns ZS, Kleele T, Mansvelder HD, Sakmann B, de Kock CP (2011) Three-dimensional axon morphologies of individual layer 5 neurons indicate cell type-specific intracortical pathways for whisker motion and touch. Proc Natl Acad Sci USA 108:4188–4193.

Oberlaender M, Ramirez A, Bruno RM (2012a) Sensory experience restructures thalamocortical axons during adulthood. Neuron 74:648–655.

Oberlaender M, de Kock CPJ, Bruno RM, Ramirez A, Meyer HS, Dercksen VJ, Helmstaedter M, Sakmann B (2012b) Cell type–specific three-dimensional structure of thalamocortical circuits in a column of rat vibrissal cortex. Cereb Cortex 22:2375–2391.

Ragan T, Kadiri LR, Venkataraju KU, Bahlmann K, Sutin J, Taranda J, Arganda-Carreras I, Kim Y, Seung HS, Osten P (2012) Serial two-photon tomography for automated *ex vivo* mouse brain imaging. Nat Methods 9:255–258.

Svoboda K (2011) The past, present, and future of single neuron reconstruction. Neuroinformatics 9:97–98.

Trainable Weka Segmentation: A Machine Learning Tool for Microscopy Image Segmentation

Ignacio Arganda-Carreras, PhD,[1] Verena Kaynig, PhD,[2] Johannes Schindelin, PhD,[3] Albert Cardona, PhD,[4] and H. Sebastian Seung, PhD[5]

[1]The French National Institute for Agricultural Research (INRA)
UMR1318, Institut Jean-Pierre Bourgin
Versailles, France

[2]Harvard School of Engineering and Applied Sciences
Cambridge, Massachusetts

[3]University of Wisconsin–Madison
Madison, Wisconsin

[4]Howard Hughes Medical Institute
Janelia Farm Research Campus
Ashburn, Virginia

[5]Princeton Neuroscience Institute, Princeton University
Princeton, New Jersey

Introduction

State-of-the-art light and electron microscopes are capable of acquiring large image datasets, but quantitatively evaluating the data often involves manually annotating structures of interest. For example, to measure the average size of mitochondria in an electron microscopy image stack, each mitochondrion has to be outlined by a human annotator. This process is time-consuming and is becoming the main bottleneck in the evaluation pipeline. To overcome this problem, we have introduced the Trainable Weka Segmentation (TWS), a machine learning tool that leverages a limited number of manual annotations in order to train a classifier and segment the remaining data automatically. The tool works interactively, allowing the user to guide the training by providing corrections to the classifier output. In addition, TWS can provide unsupervised segmentation learning schemes (clustering) for image data and can be customized to employ user-designed feature maps or classifiers.

The usefulness of the TWS tool has already been demonstrated by its utilization in a wide range of imaging pipelines that involve disparate segmentation tasks: analyzing wing photomicrographs (Dobens and Dobens, 2013), visualizing myocardial blood flow (Krueger et al., 2013), monitoring nests of bees (Hart and Huang, 2012), and other applications. TWS has proven useful for performing segmentation using many different image modalities. These include magnetic resonance imaging (Kulinowski et al., 2011), two-photon microscopy (Villa et al., 2013), serial-section transmission electron microscopy (Laptev et al., 2012), confocal fluorescence microscopy (Felcht et al., 2012; Frank et al., 2012; Crepaldi et al., 2013), micro- and computerized tomography (Maiora and Graña, 2012; Macdonald and Shefelbine, 2013), transmission scanning (Mathew et al., 2012), and angiography (Favazza et al., 2013).

Background

Traditional image processing methods

Image segmentation is generally defined as the process of partitioning a digital image into nonintersecting regions. These regions or segments comprise sets of pixels that share certain visual characteristics and are assigned a specific label. For instance, in the microscopic image of a cell, one could segment the different organelles and label pixels belonging to the nucleus, the mitochondria, and other structures. Similarly, in an image from a security camera, one might want to identify suspicious objects and separate them from the rest of the pixels. In the same example, a face recognition system may attempt to label the person or persons appearing in the image. Therefore, image segmentation can be regarded as an ill-defined problem since, depending on the final application, different ways of partitioning the same image can be considered correct. Hundreds of automatic and semiautomatic segmentation algorithms have been presented since the appearance of the digital image. However, no single method can be considered appropriate for all types of images. Moreover, methods that have been designed for a particular type of image might not be applicable to other types.

Most traditional methods are based only on the intensity information of pixels. Nonetheless, humans use much more knowledge when performing manual segmentation. For that reason, in recent years, trainable methods have emerged as powerful tools to include part of that knowledge in the segmentation process and improve the accuracy of the labeled regions. Algorithms to perform this task have been developed principally for natural and medical images but can be adapted for other types of image data and transferred to platforms that are accessible to both experienced and inexperienced users. Such software should provide a user-friendly and intuitive framework for prototyping and applying machine learning algorithms to image data and visualizing their results.

Platforms that build in machine learning tools

Just a few software platforms partially provide both machine learning and image processing tools. These include commercial platforms (e.g., MATLAB, MathWorks, Natick, MA) and open-source plaforms, e.g., the Konstanz Information Miner (KNIME) by Berthold et al. (2007), RapidMiner (http://rapid-i.com), Vision with Generic Algorithms (VIGRA) by Köthe (1999), and CellProfiler by Kamentsky et al. (2011). Commercial platforms usually target inexperienced users and a wide range of image types. However, the details of the algorithms are hidden, which is undesirable for use in scientific research. Conversely, those details are available in open-source platforms such as KNIME and RapidMiner, which is becoming the world-leading open-source system for data and text mining. Nevertheless, RapidMiner is developed primarily by the machine learning community for the machine learning community, and its image processing extension by Burget et al. (2010) provides only a minimal set of image tools. This makes the platform less attractive for computer scientists to use it to develop image segmentation solutions. Other projects like VIGRA offer powerful computer vision libraries with a focus on algorithms

NOTES

and data structures but no visualization tools or user-friendly interfaces. And only a development version of CellProfiler integrates VIGRA learning methods into custom segmentation pipelines.

To address these deficiencies in the field, we started the new open-source software project TWS. The project combines the image processing toolkit Fiji (Fiji Is Just ImageJ) by Schindelin et al. (2012), a popular distribution of ImageJ by Rasband (1997–2009), with the state-of-the-art machine learning algorithms provided in the latest version of the data mining and machine learning toolkit Waikato Environment for Knowledge Analysis (WEKA) by Hall et al. (2009). TWS provides a set of library methods for extracting statistical properties of an image from user-provided pixel samples and uses that information to segment the rest of the pixels in that image or a similar image. These methods are then implemented in a modular and transparent way and can be called up from any Fiji plugin, script, or macro. TWS also provides a friendly graphical user interface (GUI) for loading a two-dimensional (2D) image or image stack and performing automatic segmentation by interactive learning.

TWS came about through the perceived need of a general purpose workbench that would allow researchers from the imaging world to access state-of-the-art techniques in machine learning to improve their image segmentation results. This need was observed by Burget et al. (2010), who created an image processing extension for the popular data mining software RapidMiner. Following that innovation, Sommer et al. (2011) presented ilastik, an interactive, user-friendly tool for image classification and segmentation based on training a random forest classifier on precomputed nonlinear features. TWS provides both a set of library functions to design experiments and algorithms, based on the WEKA and Fiji platforms, and a complete GUI for performing interactive and noninteractive learning.

Enhancing Fiji and WEKA

In the past four years, Fiji has become the software of reference for many scientists to meet their image analysis needs, especially in the field of biomedical imaging. Fiji provides its users with powerful tools to generate sophisticated image processing pipelines and algorithms, via scripting languages and library methods that can handle many types and sizes of images. At the same time, WEKA is nowadays recognized as a landmark system in data mining and machine learning. It has achieved widespread acceptance within academia and business circles, and has become a widely used tool for data mining research.

However, little (if any) of the success of both toolboxes would have been possible if they had not been released as open-source software. Giving users free access to the source code has enabled a thriving community to develop and facilitated the creation of many projects that incorporate or extend WEKA's existing functionalities. One of the best examples of these projects is TWS, which combines both toolboxes to enlarge their capabilities and increase their impact and range of application. For WEKA users and developers, TWS offers transparent access to a whole new set of supervised and unsupervised learning problems based on an arbitrarily large number of image features. For Fiji users and developers, respectively, TWS provides a new and user-friendly way of performing image segmentation and facilitates access to learning tools that can be used to either enhance existing image processing algorithms and pipelines or create new ones.

Implementation

Computing environment

TWS has been developed using the developing (but stable) versions of Fiji and WEKA (version 3.7.6). The only requirement to use TWS is to have Fiji installed and up to date. In fact, given the cross-platform nature of Fiji, it can be run with any Unix, Macintosh, or Windows environment. The software is distributed as open-source software with a detailed user manual and multiple tutorials published in the Fiji wiki (http://fiji.sc).

For basic users, TWS requires only basic experience and knowledge of Fiji. The user should be familiar with the simple interface of Fiji and its plugin system. The TWS plugin can be run from the plugin menu under the segmentation submenu. The user can then interact with the GUI without the need for any other Fiji commands (a detailed explanation is given in the user manual). For more experienced users and developers, the TWS library methods are accessible from the scripting interpreters available in Fiji as well as from any third-party script or plugin.

Data input/output

When the plugin is called up from the Fiji menu, TWS runs on the current 2D (gray-scale or color) image or stack of images. If no image data are open, the plugin will ask for a file to load in any of the multiple image formats compatible with Fiji. The image feature information produced in the interactive learning procedure can be saved and loaded in the Attribute-Relation File Format (ARFF) (Witten and Frank, 2005), which can also be loaded and manipulated in the WEKA suite. The trained

models (classifiers and clusterers) can also be saved and loaded in a WEKA-compatible format (.model). This separation between feature data and models enables full compatibility with the WEKA tools and library methods. For instance, a user can save the feature data of an experiment using the plugin's GUI, then load it into the WEKA experimenter to find the most suitable classifier, and finally load the classifier back into the GUI to use it in an arbitrary number of images.

Image features

In computer vision, a feature is usually defined as the part of an image of special interest, and image features are used frequently as the starting point for many algorithms. Therefore, the overall algorithm will often only be as good as its feature detector. For that reason, TWS includes a wide range of image features, most of which are extracted using common filters or plugins available in the Fiji core. By default, more than 70 features are computed using generic parameters and spherical filters with radii varying from 1 to 16 pixels. The user has complete freedom to select features and tune their scales and optional parameters using either the settings dialog in the GUI or the specific library methods.

Based on their purpose, the features available in TWS can be grouped into the following types:

- ***Edge detectors***, which aim at indicating boundaries of objects in an image. TWS includes, among other edge detectors, Laplacian and Sobel filters, difference of Gaussians, Hessian matrix eigenvalues, and Gabor filters.
- ***Texture filters***, to extract texture information. Among others, TWS provides a set of filters including minimum, maximum, median, mean, variance, entropy, structure tensor, etc.
- ***Noise reduction filters***, such as Gaussian blur, bilateral filter, Anisotropic diffusion, Kuwahara, and Lipschitz.
- ***Membrane detectors***, which localize membrane-like structures of a certain size and thickness.

In addition to providing filters, TWS allows the user to customize features. As described in the wiki, a very simple script is needed to include user-defined features in the segmentation process. As long as they contain unique identifiers, an arbitrary number of new features can be used either alone or in combination with the existing filters. This opens the door to all kinds of linear and nonlinear features that users can externally create, including 3D features.

Segmentation by pixel classification

To segment the input image data, TWS transforms the segmentation problem into a pixel classification problem in which each pixel can be classified as belonging to a specific segment or class. A set of input pixels that has been labeled is represented in the feature space and then used as the training set for a selected classifier. Once the classifier is trained, it can be used to classify either the rest of the input pixels or completely new image data. The number and names of the classes, together with the desired learning algorithm, are defined by the user. All methods available in WEKA can be used. These include a large variety of supervised classification and regression algorithms and clusterers. For a complete list, visit http://wiki.pentaho.com/display/DATAMINING/Data+Mining+Algorithms+and+Tools+in+Weka . Figure 1 describes the pixel classification scheme of TWS.

One of the strengths of the TWS toolbox is that it allows different options to perform training and testing. One possibility is to use the GUI following an active learning approach. In a similar way to ilastik (the image classification and segmentation tool developed by Sommer et al., 2011), the user is allowed to interactively provide training samples while navigating the data, obtain on-the-fly test results on the loaded input image, and retrain the classifier as many times as needed. In this way, the user can fine-tune the parameters of the classifier and select labels until achieving satisfactory results. More classical (not interactive) approaches are also available via the library methods, allowing training on arbitrarily large labeled data.

Creating your own algorithms

The segmentation of image data typically requires applying a sequence of algorithms to many images in a so-called pipeline. In Fiji, fast prototyping of segmentation pipelines is facilitated via scripting, which uses simple programming commands (or scripts) to define sequences of operations that can be applied to sets of images.

Scripting became popular among inexperienced users thanks to the simple and friendly ImageJ macro language, which allows users to record GUI commands and rapidly construct basic programs. TWS is not an exception, and all the user actions in its GUI can be recorded and reproduced later in a macro. Additionally, Fiji supports a broad range of scripting languages, which can be used without knowledge of Java (the native language of Fiji and WEKA), and offers more advanced programming capabilities than the macro language while keeping

NOTES

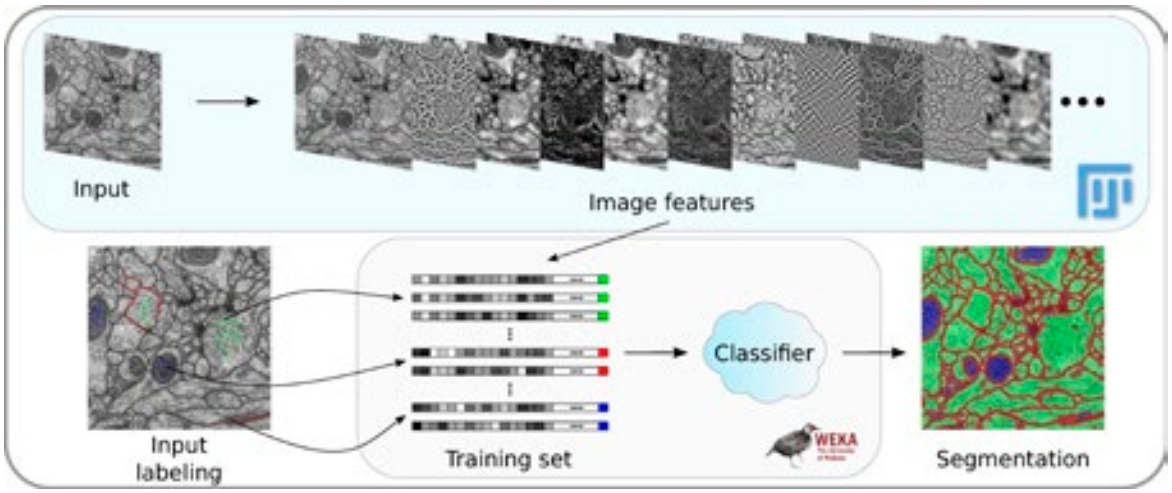

Figure 1. TWS pipeline for pixel classification. Image features are extracted from an input image using Fiji-native methods. Next, a set of pixel samples is defined and represented as feature vectors, and a WEKA learning scheme is trained on those samples and finally applied to classify the remaining image data. The input image in this example pipeline is a serial section from a transmission electron microscopy dataset from the *Drosophila* first instar larva ventral nerve cord; its pixels are divided into three classes: membrane, mitochondria, and cytoplasm.

relative simplicity for the occasional programmer. TWS makes extensive use of this functionality to provide an ideal framework to rapidly prototype and implement new algorithms. Individual commands can be interactively tested on the current images using the corresponding scripting language interpreter. In addition, the script editor enables writing, debugging, testing, and running arbitrarily complex scripts in all the supported languages, including Java itself. For example, it takes only 10 lines of code to load an image and its binary labels to train a classifier on how to identify cells, apply the trained classifier to a second image, and extract each individual cell in the image by running a watershed algorithm implementation (Tsukahara et al., 2008) on the cell probability map (Fig. 2).

The details of the code or the chosen scripting language are not relevant (TWS scripting tutorials are available at http://fiji.sc/Scripting_the_Trainable_Segmentation). All scripting languages in Fiji allow users to access advanced image processing libraries and now, thanks to TWS, to interact with the WEKA machine learning algorithms without mastering Java programming. Moreover, it is also possible to integrate this functionality through the Fiji interfaces in other image platforms such as MATLAB or ITK (Ibanez et al., 2003).

Conclusion

We have presented TWS, a versatile tool for image segmentation based on pixel classification. The software has a library of methods and a GUI that makes it easy to use without any programming experience. This toolbox is an important addition to the growing arsenal of segmentation plugins in Fiji (fiji.sc/Category:Segmentation) for analyzing biological and nonbiological image data. TWS is designed to facilitate the integration of machine learning schemes with image processing modules into a pipeline. Researchers can easily prototype segmentation algorithms using TWS methods with any of the scripting languages available in Fiji. Scripts are indeed vehicles of execution, but also act as mechanisms for disseminating the new algorithm or pipeline that are easily accessible by others.

TWS is intended to work as a bridge between the machine learning and the biomedical imaging communities, facilitating a framework to develop, test, and apply novel solutions to the existing segmentation challenges. The project is completely open source, and we invite users and developers to contribute to its growth.

a)

```
1  import trainableSegmentation.WekaSegmentation;
2  trainInput = IJ.openImage( "https://dl.dropboxusercontent.com/u/1958594/cells/images/A9p5d.tif" );
3  trainLabels = IJ.openImage( "https://dl.dropboxusercontent.com/u/1958594/cells/labels/A9p5d.tif" );
4  testInput = IJ.openImage( "https://dl.dropboxusercontent.com/u/1958594/cells/images/A9p9d.tif" );
5  segmentator = new WekaSegmentation( trainInput ); // create segmentator
6  segmentator.addRandomBalancedBinaryData( trainInput, trainLabels, "class 1", "class 2", 4000 );
7  segmentator.trainClassifier(); // train classifier based on input image and binary labels
8  probs = segmentator.applyClassifier( testInput, 0, true ); // apply classifier to test image
9  probs8bit = new ImagePlus( "Probs 8-bit", probs.getProcessor().convertToByte( true ) );
10 IJ.run( probs8bit, "Watershed ", "blurring=3.0'   watershed='1 0 40 80 0 0'   display='2 4' " );
```

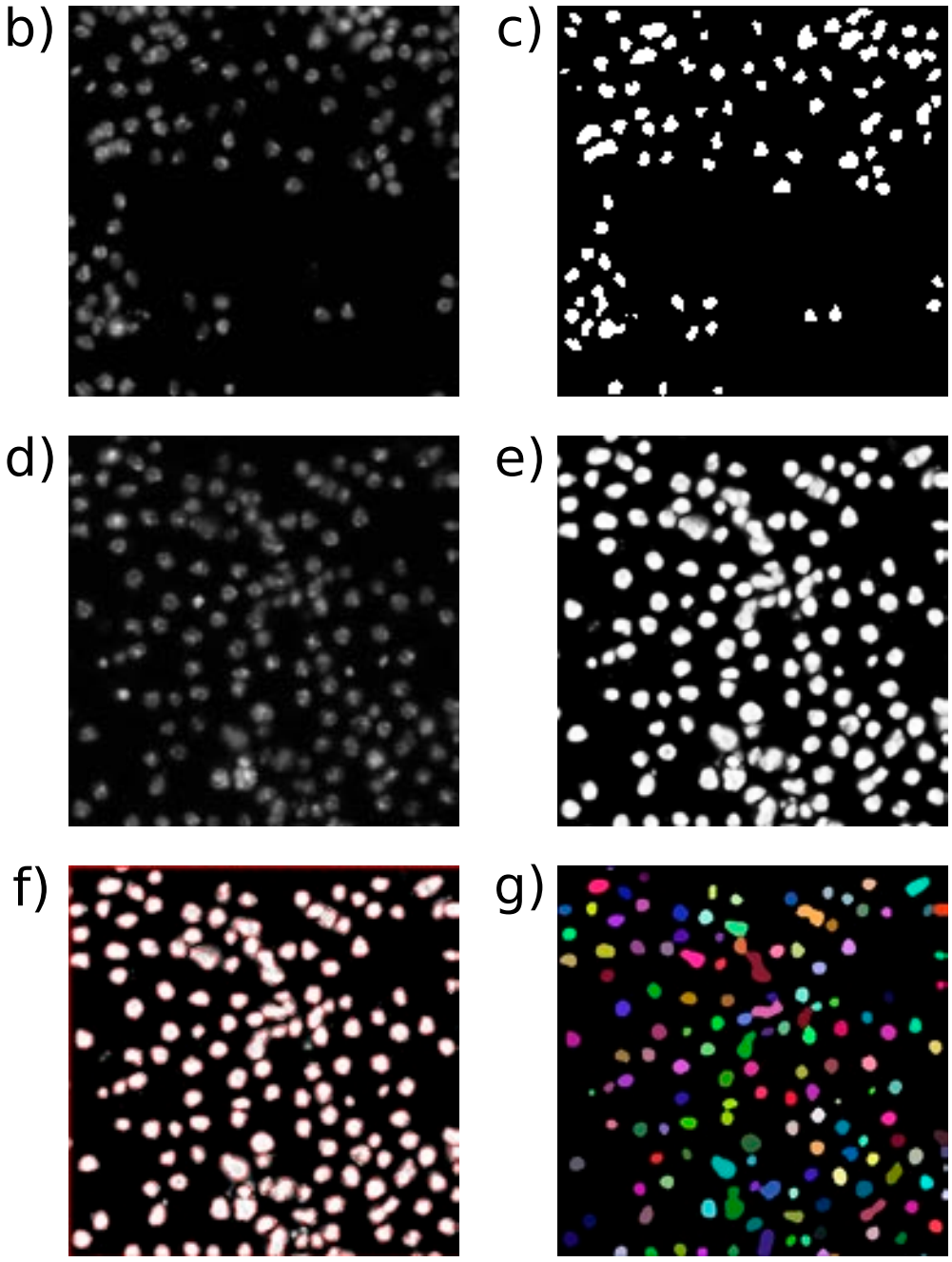

Figure 2. Scripting your own algorithm. *a,* Example of BeanShell script that trains on a cell colony image (*b*) from the Broad Bioimage Benchmark Collection (Ljosa et al., 2012) and its corresponding binary labels (*c*) and then applies the trained classifier to a test image (*d*) to obtain its in/out probability map (*e*). The algorithm finally runs watershed segmentation to extract the boundaries of the cells (*f*) and labels the individual objects (*g*).

NOTES

References

Berthold MR, Cebron N, Dill F, Gabriel TR, Kötter T, Meinl T, Ohl P, Sieb C, Thiel K, Wiswedel B (2007) KNIME: The Konstanz Information Miner in studies in classification, data analysis, and knowledge organization (GfKL 2007). Berlin, Heidelberg: Springer.

Burget R, Karásek J, Smékal Z, Uher V, Dostál O (2010) RapidMiner Image Processing Extension: a platform for collaborative research. International Conference on Telecommunications and Signal Processing, Baden, Austria, August 7–10.

Crepaldi L, Policarpi C, Coatti A, Sherlock WT, Jongbloets BC, Down TA, Riccio A (2013) Binding of TFIIIC to SINE elements controls the relocation of activity-dependent neuronal genes to transcription factories. PLoS Genetics 9:e1003699.

Dobens AC, Dobens LL (2013) FijiWings: an open source toolkit for semiautomated morphometric analysis of insect wings. G3 (Bethesda) 3:1443–1449.

Favazza TL, Tanimoto N, Munro RJ, Beck SC, Garrido MG, Seide C, Sothilingam V, Hansen RM, Fulton AB, Seeliger MW, Akula JD (2013) Alterations of the tunica vasculosa lentis in the rat model of retinopathy of prematurity. Doc Ophthalmol 127:3–11.

Felcht M, Luck R, Schering A, Seidel P, Srivastava K, Hu J, Bartol A, Kienast Y, Vettel C, Loos EK, Kutschera S, Bartels S, Appak S, Besemfelder E, Terhardt D, Chavakis E, Wieland T, Klein C, Thomas M, Uemura A, et al. (2012) Angiopoietin-2 differentially regulates angiogenesis through TIE2 and integrin signaling. J Clin Invest 122:1991–2005.

Frank M, Duvezin-Caubet S, Koob S, Occhipinti A, Jagasia R, Petcherski A, Ruonala MO, Priault M, Salin B, Reichert AS (2012) Mitophagy is triggered by mild oxidative stress in a mitochondrial fission dependent manner. Biochim Biophys Acta 1823:2297–2310.

Hall M, Frank E, Holmes G, Pfahringer B, Reutemann P, Witten I (2009) The WEKA data mining software: an update. SIGKDD Explor 11:10–18.

Hart N, Huang L (2012) Monitoring nests of solitary bees using image processing techniques. 19th International Conference on Mechatronics and Machine Vision in Practice (M2VIP), Auckland, New Zealand, November 28–30, 2012. IEEE Explore, pp. 1–4.

Ibanez L, Schroeder W, Ng L, Cates J (2003) The ITK software guide, Ed 2. Kitware Inc.

Kamentsky L, Jones TR, Fraser A, Bray MA, Logan DJ, Madden KL, Ljosa V, Rueden C, Eliceiri KW, Carpenter AE (2011) Improved structure, function and compatibility for CellProfiler: modular high-throughput image analysis software. Bioinformatics 27:1179–1180.

Köthe U (1999) Reusable software in computer vision. In: Handbook of computer vision and applications, Vol 3, Systems and applications. San Diego: Academic Press.

Krueger MA, Huke SS, Glenny RW (2013) Visualizing regional myocardial blood flow in the mouse. Circulation Res112:e88–e97.

Kulinowski P, Dorozynski P, Mlynarczyk A, Weglarz WP (2011) Magnetic resonance imaging and image analysis for assessment of HPMC matrix tablets structural evolution in USP apparatus 4. Pharm Res 28:1065–1073.

Laptev D, Vezhnevets A, Dwivedi S, Buhmann JM (2012) Anisotropic ssTEM image segmentation using dense correspondence across sections. In: 15th Annual Conference on Medical Image Computing and Computer-Assisted Intervention (MICCAI 2012), October 1–5, 2012, Nice, France; pp. 323–330. Berlin, Heidelberg: Springer.

Ljosa V, Sokolnicki KL, Carpenter AE (2012) Annotated high-throughput microscopy image sets for validation. Nat Methods 9:637–637.

Macdonald W, Shefelbine S (2013) Characterising neovascularisation in fracture healing with laser Doppler and micro-CT scanning. Med Biol Eng Comp 51:1157–1165.

Maiora J, Graña M (2012) Abdominal CTA image analisys through active learning and decision random forests: application to AAA segmentation. In: The 2012 International Joint Conference on Neural Networks (IJCNN), Brisbane, Australia, June 10–15, 2012. IEEE Explore, pp. 1–7.

Mathew MD, Mathew ND, Ebert PR (2012). WormScan: a technique for high-throughput phenotypic analysis of *Caenorhabditis elegans*. PloS One 7:e33483.

Rasband W (1997–2009) ImageJ. US National Institutes of Health, Bethesda, Maryland.

Schindelin J, Arganda-Carreras I, Frise E, Kaynig V, Longair M, Pietzsch T, Preibisch S, Rueden C, Saalfeld S, Schmid B, Tinevez JY, White DJ, Hartenstein V, Eliceiri K, Tomancak P, Cardona A (2012) Fiji: an open-source platform for biological-image analysis. Nat Methods 9:676–682.

Sommer C, Straehle C, Kothe U, Hamprecht F (2011) Ilastik: interactive learning and segmentation toolkit, In: Biomedical imaging: from nano to macro. 8th IEEE International Symposium on Biomedical Imaging (ISBI), March 30–April 2, Chicago. Proceedings, pp. 230–233.

Tsukahara M, Mitrovic S, Gajdosik V, Margaritondo G, Pournin L, Ramaioli M, Sage D, Hwu Y, Unser M, Liebling T (2008) Coupled tomography and distinct-element-method approach to exploring the granular media microstructure in a jamming hourglass. Phys Rev E (Statistical, Nonlinear, and Soft Matter Physics) 77:061306.

Villa MM,Wang L, Huang J, Rowe DW, Wei M (2013) Visualizing osteogenesis *in vivo* within a cell scaffold construct for bone tissue engineering using two-photon microscopy. Tissue Eng Part C Meth 19:839–849.

Witten IH, Frank E (2005) Data mining: practical machine learning tools and techniques. Morgan Kaufmann.

NOTES